Chem Soc Rev

Single Atom Electrocatalysts Supported on Graphene or Graphene-Like Carbons

Journal:	*Chemical Society Reviews*
Manuscript ID	CS-REV-06-2019-000422.R1
Article Type:	Review Article
Date Submitted by the Author:	05-Aug-2019
Complete List of Authors:	Fei, Huilong; Hunan University College of Chemistry and Chemical Engineering, Chemistry and Chemical Engineering; Dong, Juncai; Institute of High Energy Physics, Chinese Academy of Sciences, Beijing Synchrotron Radiation Facility Chen, Dongliang; Institute of High Energy Physics Chinese Academy of Sciences, hu, tiandou; Institute of High Energy Physics, Beijing Synchrotron Radiation Facility Duan, Xidong; Hunan University, CHemistry and Chemical Engineering Shakir, Imran; Deanship of scientific research, College of Engineering, King Saud University, Huang, Yu; Univeristy of California, Los Angeles, Materials Science and Engineering Duan, Xiangfeng; UCLA,

Single Atom Electrocatalysts Supported on Graphene or Graphene-Like Carbons

Huilong Fei,[1] Juncai Dong,[2] Dongliang Chen,[2] Tiandou Hu,[2] Xidong Duan,[1] Imran Shakir,[3,4,] Yu Huang,[3,*] Xiangfeng Duan[5,*]*

[1]State Key Laboratory for Chemo/Biosensing and Chemometrics, College of Chemistry and Chemical Engineering, Hunan University, Changsha 410082, China; [2]Beijing Synchrotron Radiation Facility, Institute of High Energy Physics, Chinese Academy of Sciences, Beijing 100049, China; [3]Sustainable Energy Technologies Centre, College of Engineering, King Saud University, Riyadh 11451, Saudi Arabia; [4]Department of Materials Science and Engineering, University of California, Los Angeles, Los Angeles, CA 90095, USA. [5]Department of Chemistry and Biochemistry, University of California, Los Angeles, Los Angeles, CA 90095, USA;

*Correspondence: xduan@chem.ucla.edu, yhuang @seas.ucla.edu, mshakir@ksu.edu.sa

Abstract: Electrocatalysis plays an essential role in diverse electrochemical energy conversion processes that are vital for improving energy utilization efficiency and mitigating the aggravating global warming challenge. The noble metals such as platinum are generally the most frequently used electrocatalysts to drive these reactions and facilitate the relevant energy conversion processes. The high cost and scarcity of these materials pose a serious challenge for the wide-spread adoption and the sustainability of these technologies in the long run, which have motivated considerable efforts in searching for alternative electrocatalysts with reduced loading of precious metals or based entirely on earth-abundant metals. Of particular interests are graphene-supported single atom catalysts (G-SACs) that integrate the merits of heterogeneous catalysts and homogeneous catalysts, such as high activity, selectivity, stability, maximized atom utilization efficiency and easy separation from reactants/products. The graphene support features a large surface area, high conductivity and excellent (electro)-chemical stability, making it a highly attractive substrate for supporting single atom electrocatalysts for various electrochemical energy conversion processes. In this review, we highlight the recent advancements in G-SACs for electrochemical energy conversion, from the synthetic strategies and identification of the atomistic structure to electrocatalytic applications in a variety of reactions, and finally conclude with a brief prospect on future challenges and opportunities.

1. Introduction

Electrochemical energy conversion plays an essential role in addressing the global challenge in climate change and energy crisis. Consequently, extensive research efforts have been devoted to advanced electrochemical energy conversion technologies, such as water splitting, CO_2 conversion, N_2 reduction, fuel cells and metal-air batteries, that are critical for renewable energy harvesting, storage and efficient energy utilization.[1] The performances of these devices strongly rely on the properties of the materials used in each component, particularly the catalysts employed at the electrode/electrolyte interface to decrease the kinetic barrier of the associated electrochemical processes for improving the energy conversion efficiency.[2] As a result, considerable research efforts have been devoted to the development of highly active, selective, robust and cost-effective electrocatalysts.

In this regard, homogeneous and heterogeneous catalysis were developed independently as two parallel frontiers, each with their own merits and limits.[3] Homogeneous catalysis is characterized by the maximized atom utility efficiency, well-defined catalytic center and coordination configuration, which allows a rational design and synthesis of high-performance catalysts based on the established structure-property correlation. However, in practical applications, homogeneous catalysis is often limited by the low stability and difficulty in separation from products and solvents. Although strategies have been explored to address these challenges by immobilizing the homogeneous catalysts on solid supports, none of them have thus far found use in industry mainly due to the insufficient stability of the immobilized catalysts and the extra cost imposed by the immobilization process.[4] On the other hand, heterogeneous catalysts, particularly those based on nanostructured materials, have attracted increasing interest for their high stability, facile separation and recycling, and easy immobilization on electrodes. However, most heterogeneous catalysts feature a broad distribution of particle sizes and surface characteristics, posing serious challenges in fundamental mechanistic studies and the rational design of active sites with tailored activity and selectivity.[5] Additionally, the heterogeneous catalysts typically show a limited atom utilization efficiency due to the limited surface active sites as most the atoms are embedded in the bulk. To this end, significant research efforts have been devoted to downsizing the particle size and engineering the surface morphology to achieve more surface sites, which is particularly important in precious metal-based catalysts where cost and scarcity are of serious concerns.[6]

Single atom catalysts (SACs) with atomically dispersed metals on solid support represent the ultimate limit of nanoscale catalysts that bridge the gap between heterogeneous catalysts and homogeneous catalysts to deliver the combined merits of both.[7-10] Due to the high surface free energy of single atoms, SACs are typically supported on substrates with high surface area and abundant anchoring sites to prevent aggregation during synthesis and catalytic processes.[11,12] Typical substrates include metal surface, metal oxide, metal nitride, metal chalcogenide and nanocarbons, and SACs on these substrates have been applied to catalyze a wide range of chemical reactions, such as oxidation reactions, hydrogenation reactions, and electrocatalytic reactions.[13-19] With well-dispersed SACs on a solid support, the metal-support interactions and coordination environment may be systematically varied. In this regard, the supporting substrate plays a critical role in tailoring the catalytic activity, selectivity and stability of SACs.

Graphene, a two-dimensional material consisting of a single layer of sp^2-hybridized carbons arranged in hexagonal lattice, has extraordinary physicochemical properties and it has found applications in broad ranges of areas, such as electronics, sensing, polymer composites, energy storage and conversion.[20] Graphene exhibits several unique features to make it an attractive supporting substrate for various nanostructured catalysts (such as nanoplates, nanoparticles or nanoclusters, nanowires)[21-24] or SACs (Fig. 1). First, the atomically thin two-dimensional (2D) nature of graphene features an ultrahigh theoretical surface area (2630 m^2/g) that is important for the uniform dispersion of metal atoms, particularly at high mass loading, and for the maximized exposure of the catalytic centers to the reactants. Moreover, the highly crystalline nature of the ultrathin graphene substrate provides an excellent platform for atomistic imaging of the exact coordination configuration of the metal centers by advanced characterization techniques, which is important for the fundamental understanding of the catalytic behavior for formulating design principles for future generations of catalysts.[25] Second, graphene exhibit excellent electrical conductivity for efficient transport of electrons to or from the catalytic sites, which is particularly important for electrocatalysis involving long-range charge transport. In comparison, SACs on metal oxide-based supports typically have rather low electrical conductivity and consequently their application areas are mainly limited to the conventional heterogeneous reactions (e.g., CO oxidation, water-gas shift reactions, oxidation and hydrogenation of organic molecules) where long-range electron transport is not a necessity.[13] Third, graphene exhibits extraordinary chemical and electrochemical stability over wide potential windows, and can withstand the harsh liquid electrolyte environment and large potential range that are typically encountered in

electrocatalytic processes. For example, in order to achieve efficient and stable operation of water splitting, a strong acid or base electrolyte is needed to increase the ionic conductivity and minimize the pH gradient occurred from the proton consumption and production at the cathode and anode, respectively.[26] Such a requirement limits the choice of stable catalysts and excludes most of SACs supported on metal or metal oxide due to the insufficient stability in such highly corrosive media. Lastly, defects engineering and chemical doping in graphene offers an additional degree of freedom to tailor the anchoring sites for the dispersion of SACs, which provides a rich playground for exploring synthetic strategies and tuning metal-support interactions.[27] In particular, pristine graphene sheets are not good supports for SACs since the adatoms on the dangling-bond free graphene sheets are highly mobile and could easily aggregate due to their low migration energy barrier.[28] Calculation results suggested that the transition metal adatoms on pristine graphene had binding energies of 0.2-1.5 eV and migration barriers of 0.2-0.8 eV, indicating that the adatoms should be mobile at room temperature. To this end, the generation of defective sites in graphene provides various possible bonding configurations for metal atoms, such as single and double vacancies.[29] The metal atoms can be anchored by the defective sites of graphene as a substitutional or interstitial dopant and form metal-vacancy complexes with much higher binding energies that ensure its stability, as has been demonstrated by both experiments and calculations.[28-31] Besides, a wide range of heteroatoms (e.g., N, B, O, S) can be incorporated within graphene lattice to serve as potential anchoring sites for metal atoms with diverse coordination geometries, providing a new dimension to tune the interaction between metal atoms and the coordination environment.[32]

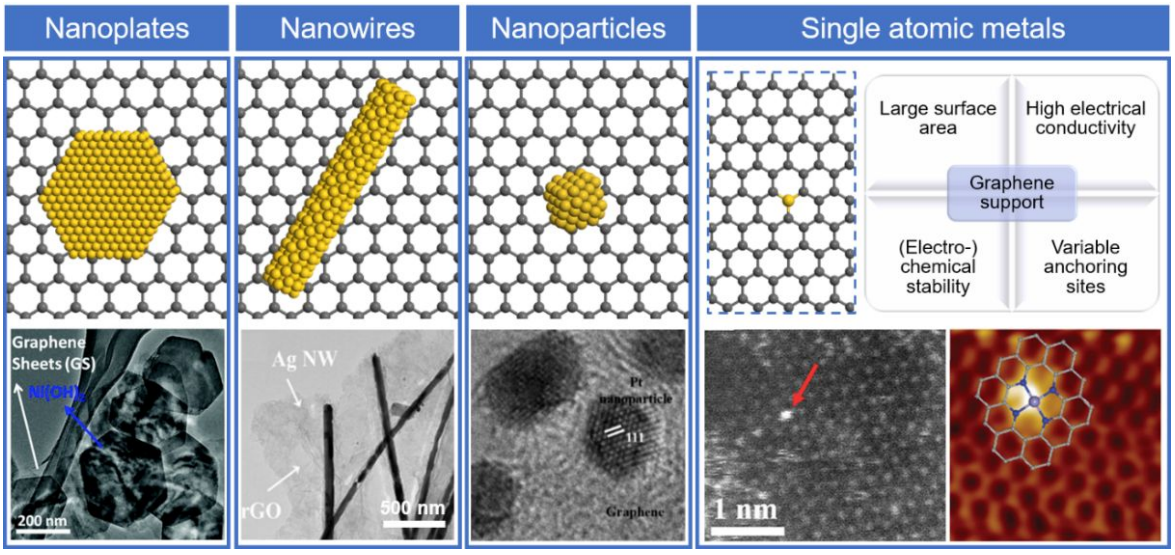

Fig. 1 Graphene as supports for nanostructured catalysts. Schematic illustration of graphene supports for different types of nanostructures, including nanoplate, nanowire, nanoparticles

and single atomic metals. Image of nanoplate on graphene: reproduced with permission from Wang et al.[21] Copyright 2010 American Chemical Society. Image of nanowire on graphene: reproduced with permission from Hu et al.[22] Copyright 2017 Wiley-VCH. Image of nanoparticles on graphene: reproduced with permission from Kundu et al.[23] Copyright 2011 American Chemical Society. Image of single atomic metals on graphene: reproduced with permission from Deng et al.[33] Copyright 2015 American Association for the Advancement of Science.

With its intriguing physicochemical properties and versatility in chemical functionalization, the exploration of graphene as supports for SACs has attracted intense research interests and endeavors in the past few years. This review provides an overview of the recent progress in graphene-supported SACs (G-SACs) for electrochemical energy conversion processes. We will begin with recent theoretical and experimental efforts in establishing the correlation between the structure and catalytic properties of G-SACs, elaborating how the catalytic behaviors could be tuned or influenced by tailoring the electronic interaction between metal atoms and graphene support. We will then summarize the various synthetic strategies developed to access G-SACs, the recent advancements in the identification of the atomistic structure and their applications in different types of electrochemical energy conversion processes, including oxygen reduction reaction (ORR), hydrogen evolution reaction (HER), oxygen evolution reaction (OER), CO_2 reduction reaction (CO_2RR), N_2 reduction reaction (NRR) and so on. Finally, we briefly discuss about the challenges and opportunities ahead.

2. Understanding structure-activity correlation

The activity of an electrocatalyst system can be generally improved by either increasing the number of active sites (e.g., through the increased loading or minimizing the size to increase exposed active sites) or enhancing the intrinsic activity of each active site (Fig. 2).[2] For catalysts based on transition metals, it has long been established that the intrinsic activity is highly dependent on the strength of the adsorbate-surface interaction and hence on the surface electronic structure (the *d*-band center).[34] With respect to traditional heterogeneous catalysts of metal surfaces, the regulation of their electronic structure and hence catalytic activity has been realized by alloying, sizing, defects, strain, interface, geometry, etc.[35-37] In the case of the homogeneous catalysts with organometallic compounds, the variability in their reactivity can be generally achieved by tuning the ligand-field effect,

which is governed by the central metal center as well as its chemical and structural coordination environment.[38] Considering that G-SACs can be regarded as the mimics of organometallic complexes by having the metal center and neighboring coordinators accommodated in the π-conjugated graphitic carbon, the concept of electronic modulation by ligand-field effects can be transferred to some degree from the familiar paradigm of homogeneous catalysis to G-SACs. In this regard, the intrinsic activity of G-SACs can be regulated by various factors, including the metal identity, the coordination configuration of the metal center, the Lewis acidity/basicity (electron-donating/withdrawing capability) of the graphene substrate and the metal location (edge site versus basal plane site) (Fig. 2). A fundamental theoretical understanding on how these factors influence the catalytic activity along with experimental validations is central for defining the basis for the rational design of new generations of high-performance G-SACs.

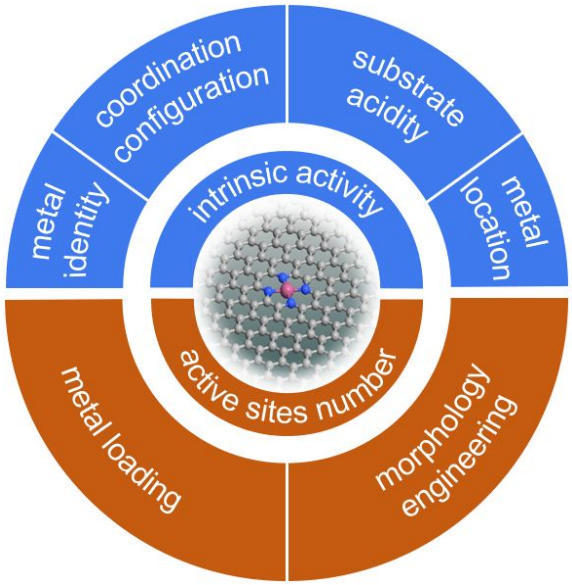

Fig. 2 Overview of factors affecting the intrinsic activity and active sites number in G-SACs.

In recent years, numerous theoretical simulations have been performed on G-SACs to explore their potential applications in electrocatalysis with focus on establishing the correlation between the local atomic structure and the catalytic properties. Choi et al. performed a high-throughput computational search for hydrogen electrocatalysts based on the porphyrin-like complexes embedded in the graphene lattices (Fig. 3A).[27] The regulation in the electronic structure of these motifs was achieved by varying the metal center (30 *d*-block transition metals), the coordination atoms (B, C, N, O, S) coordinated to the metal center, and the coordination geometry (threefold and fourfold coordination geometries at the mono-vacancy and di-vacancy sites, respectively). The consideration of these variables produced a

large candidate pool (300 combinations), among which 180 combinations passed the complex stability screening test while the others would form metal aggregates. The stability screening test further suggested that C and N are the best coordination atoms and they predominantly adopt the threefold (3C) and fourfold (4N) configurations, respectively. The catalytic activity of the selected combinations was then evaluated with the descriptor based on the free energy of the hydrogen adsorption on the metal centers. The screening results reveal that the majority of the active and stable catalysts were related to the 3C configuration (Fig. 3B), attributed to the free orbitals of threefold-coordinated metal center that can interact more strongly with the hydrogen 1*s* orbital. In another study, Xu et al. developed a theory-based universal design principle to evaluate the catalytic activity of G-SACs toward a variety of reactions, including ORR, OER and HER.[39] A total of 112 G-SACs models were constructed on various transition metal atoms embedded in graphene with four types of configurations (Fig. 3C), including a mono-vacancy with three carbon atoms (SV-C_3), a di-vacancy with four carbon atoms (DV-C_4), four pyridine nitrogen atoms (pyridine-N_4), and four pyrrole nitrogen atoms (pyrrole-N_4). A complex descriptor, associated with the electronegativity of the metal atom, coordination atom type and coordination number, was identified to intimately correlate with intermediate adsorption strength and thus catalytic activities, and used to predict highly active G-SACs with specific active centers (e.g., Fe-pyridine/pyrrole-N_4 for ORR, Co-pyrrole-N_4 for OER and Mn-pyrrole-N_4 for HER). Similar theoretical efforts have been performed to understand the influence of local chemical and structural environments of the metal centers on their catalytic activity and selectivity toward CO_2RR, CO reduction, and NRR.[40-42]

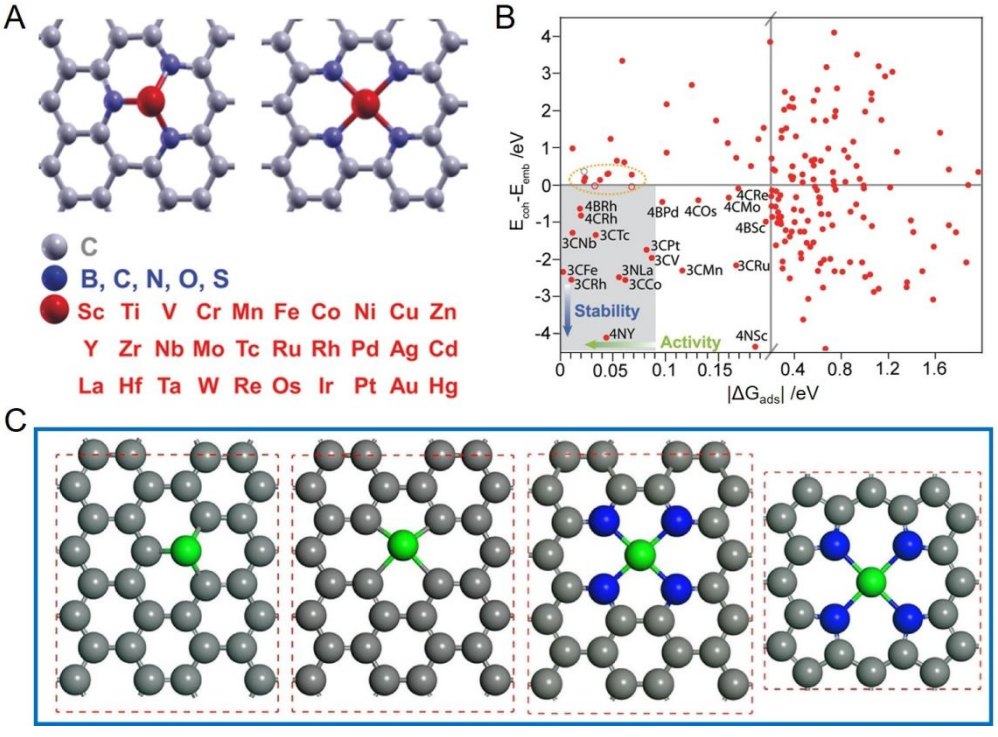

Fig. 3 Theoretical studies on the correlation between structure and intrinsic catalytic activity in G-SACs. (A) Illustration of the possible transition metal-embedded graphene complexes forming the initial material pool for the search of hydrogen electrocatalysts. (B) Descriptor-based screening results of G-SACs catalyst candidates based on activity and stability. The lower-left quadrant contains materials that passed both criteria. Reproduced with permission from Choi et al.[27] Copyright 2015 Wiley-VCH. (C) Schematic of a transition metal atom embedded in graphene with different coordination environments. From left to right: mono-vacancy with three carbon atoms (SV-C_3), di-vacancy with four carbon atoms (DV-C_4), four pyridine nitrogen atoms (pyridine-N_4), four pyrrole nitrogen atoms (pyrrole-N_4). Reproduced with permission from Xu et al.[39] Copyright 2018 Nature Publishing Group.

Despite considerable progress in theoretical studies, to experimentally establish the exact structure-to-property correlation in G-SACs remain challenging mainly due to the difficulties in accessing G-SACs with well-defined and controllable atomistic structure, and the technical difficulties in unambiguously identifying the exact atomic structure of G-SACs. Unlike homogeneous catalysts where precise synthetic chemistry can guide the synthesis and modification of active sites, current progress in the synthesis of G-SACs primarily involves a trial-and-error approach. For instance, high-temperature pyrolysis of mixed precursors represents the most frequently used approach to metal-nitrogen-carbon (M-N-C) catalysts with atomic MN_x active sites, which however usually leads to the formation of atomic metal sites mixed with metal aggregates.[43] Furthermore, diverse coordination configurations could be simultaneously formed in a given M-N-C catalyst.[44] These structural and compositional heterogeneities severely complicate the identification of the active site and further the correlation between the structure and catalytic properties. Nevertheless, a few experimental efforts have recently been carried out, aiming at establishing such correlations. For example, our group recently developed a general approach to a series of atomic transition metals (Fe, Co, Ni) embedded in nitrogen-doped graphene with a common MN_4C_4 moiety, which can be described as the metal atom occupying the di-vacancy in graphene lattice with coordination to four pyridinic N (Fig. 4A).[25] The well-defined atomistic structure and the systematically tunable metal center in the different catalysts provided an ideal model system to correlate the specific metal center with the catalytic property. Density functional theory (DFT) calculation and electrochemical measurements suggested that the catalytic activity toward OER were strongly dependent on the metal center with the activity following the trend Ni > Co > Fe. In another example, Wang et al. synthesized a series of graphene-supported single atomic Co

with varied numbers of N coordinators, as identified by EXAFS spectra (Fig. 4B, C). Experimental and theoretical explorations on applying these materials as CO_2RR catalysts suggested that the decrease in the number of coordinating N atoms would result in more unoccupied 3*d* orbitals of Co atoms, resulting in an increase of the absorption of reaction intermediates and thus the catalytic activity.[45] Moreover, the modification in the coordination configuration of the metal center in G-SACs by secondary binding sites (e.g., boron, sulfur, chlorine, carbon monoxide) in addition to the nitrogen sites have recently been employed to modulate their electronic structure and catalytic behaviors.[46-50]

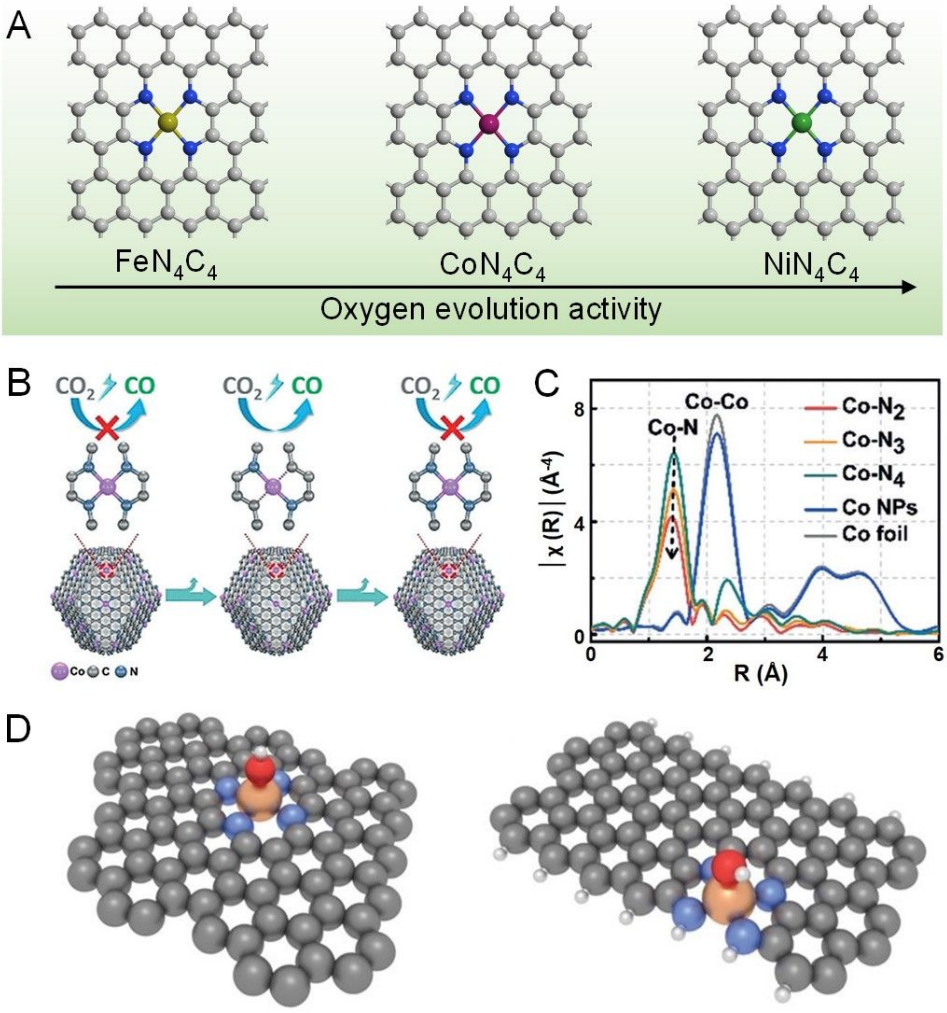

Fig. 4 Representative experimental studies on the correlation between structure and intrinsic catalytic activity in G-SACs. (A) Illustration of the trend for the catalytic activity toward OER for MN_4C_4 moieties supported in graphene lattices. Adapted with permission from Fei et al.[25] Copyright 2018 Nature Publishing Group. (B) Schematic illustration of the dependence of CO_2RR catalytic behavior on the coordination configurations. (C) EXAFS spectra for different atomic catalysts. Adapted with permission from Wang et al.[45] Copyright 2018 Wiley-VCH. (D) Model structures of the bulk-hosted and zigzag edge-hosted FeN_4. Adapted

with permission from Chung et al.[51] Copyright 2017 American Association for the Advancement of Science.

Considering that the graphene substrate constitutes an integral part of the active site with covalent bonding rather than merely serves as an electrical conductor in G-SACs, its properties such as Lewis acidity/basicity and the location of the active sites in the substrate could also play important roles in determining the intrinsic activity of G-SACs. Ramaswamy et al. elucidated the relationship between the ORR catalytic activity of atomic Fe-N_x moieties and the basicity of the π-conjugated carbon support in Fe-N-C catalysts.[52] It was suggested that the electron-donating or withdrawing capability of the graphene support resulted from its delocalized π-electrons could regulate the *d*-orbital configuration of the metal center and consequently the chemisorption strength of O_2 and reaction intermediates on the active site. In another study, Zitolo et al. measured the pK_a of the surface nitrogen groups in their Fe-N-C catalysts and found that the higher ORR activity of the NH_3-annealed catalyst correlated well with their higher basicity than that of the non-annealed counterpart.[43] Chung et al. obtained the atomic-scale images of ORR-active FeN_4 moiety in Fe-N-C catalyst by aberration-corrected scanning transmission electron microscopy (AC-STEM) and confirmed such structure by electron energy-loss spectroscopy (EELS) with single-atom resolution.[51] Based on the quantum chemical calculation results and the observation that the dispersed Fe single atoms were preferably located at the surfaces of the graphitic domains or step edges in multilayer graphene, it was suggested that the edge-hosted FeN_4 sites rather than bulk-hosted FeN_4 primarily contribute to the observed ORR activity (Fig. 4D). The enhanced catalytic contribution of edge-hosted MN_x moieties was confirmed by later studies that synthesized G-SACs with a high fraction of the edge-hosted sites by porosity engineering in the graphene matrix.[53-55]

3. Synthetic strategies

A prerequisite for studying G-SACs is to stabilize the single atomic metals onto the support of graphene layers. The preparation of G-SACs is challenging due to the mobility of the metal atoms and their tendency to agglomerate during synthesis and post-treatments. Pristine graphene is not a good support for G-SACs since most metal adatoms usually exhibit a rather low migration barrier and high mobility on pristine graphene even at room temperature.[29] Therefore, the generation of defective sites or functionalization of graphene are

generally required to create anchoring sites to stabilize metal atoms without the formation of metal aggregates. We summarize below the synthetic strategies toward G-SACs.

3.1. Pyrolysis and thermal activation

The pyrolysis and thermal activation of precursors at high temperature remain the most widely adopted method to obtain single atomic metals supported on graphene or graphene-like nanocarbons with small domains of graphene surrounding the metal centers. The pyrolysis method is simple, scalable and does not require sophisticated instrumentation, and therefore can be readily carried out across different laboratories. Furthermore, there are versatile precursors to choose from for the optimization of metal doping and nanostructure engineering that are critical in determining the catalytic activity. The precursors used for pyrolysis can be generally divided into three different categories: molecular/polymeric precursors, graphene oxide (GO) and metal organic frameworks (MOFs).

3.1.1. Molecular/polymeric precursors

Transition metal macrocycles, such as Fe and Co porphyrins or phthalocyanines, were the first studied precursors for synthesizing M-N-C catalysts through pyrolysis at high temperature (typically above 700 °C).[43] It was later shown that the replacement of these expensive macrocycles was possible by pyrolyzing separate metal-, nitrogen- and carbon-containing precursors and since then different combinations of metal salts and N/C-containing precursors have been investigated, such as imidazole, pyrrole, melamine, formamide, polyaniline and polydopamine.[56-61] For example, Zhao et al. developed a cascade anchoring strategy to synthesize a wide range of carbon-supported single atomic metals (e.g., Fe, Co, Cu, Mn, Ni, Mo) with metal loading up to 12 wt%.[62] During the synthesis, the metal ions were firstly chelated with glucose and further anchored onto oxygen-functionalized porous carbon to isolate the metal ions (Fig. 5A). The complex was then mixed with melamine as nitrogen source, which would release carbon nitrogen species (CN_x) during high-temperature pyrolysis to bind with metal atoms to form MN_x moieties. The resulted composite exhibited uniform distribution of Fe and N elements (Fig. 5B). With systematic experimental comparisons, it was found that the chelation of metal ions, physical isolation of chelate complex, and the binding with N-species at high temperature were critical in achieving atomic metal dispersion at high loading.

The choice of precursors is not only important for the effective implantation of atomic M-N_x species into carbon but could also affect the structure and porosity of the carbon support.

For example, Chung et al. deliberately combined precursors of polyaniline and cyanamide to synthesize a catalyst that exhibited both porous structure and high intrinsic catalytic activity.[51] Precursors containing multiple heteroatoms (e.g., sulfur, boron, phosphorus) other than nitrogen could be included to introduce multiple types of dopants to modify the local coordination configuration of the metal center or tune the electronic properties of the carbon support, which could both be applied to regulate the catalytic performances.[46,48,63-65]

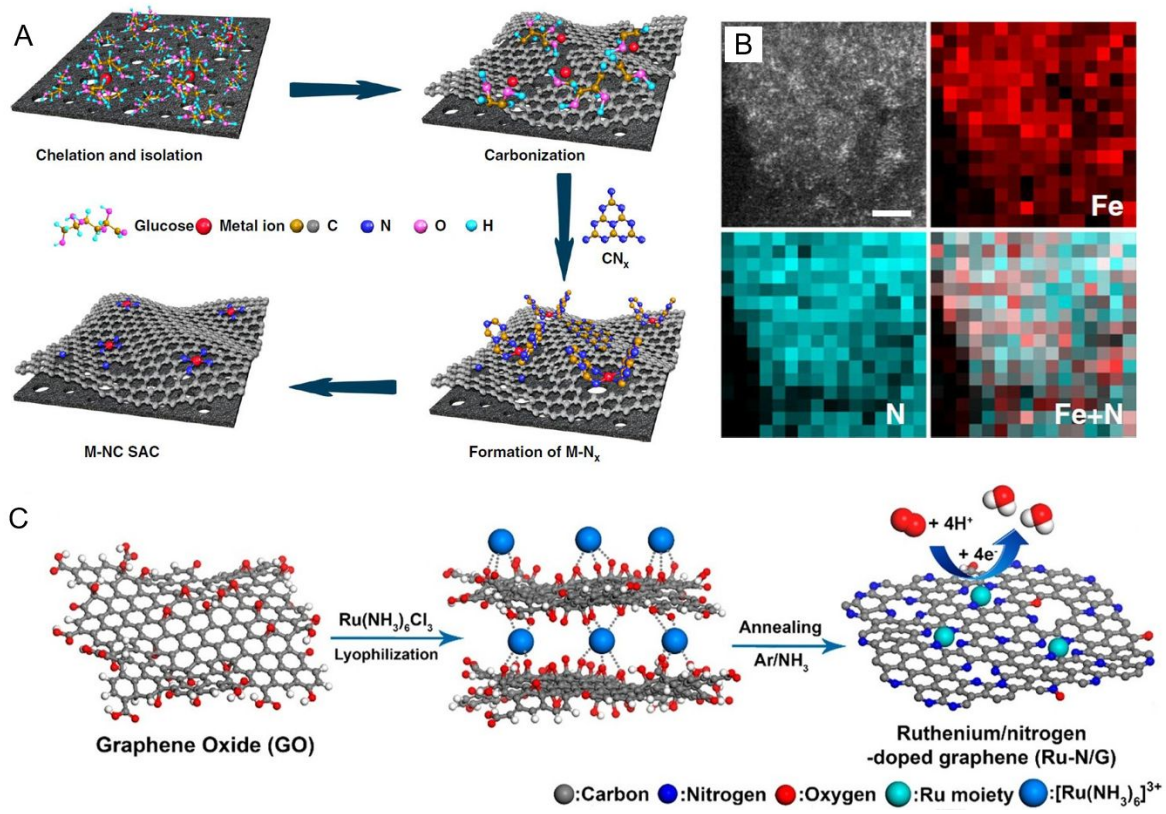

Fig. 5 (A) The cascade anchoring strategy for the synthesis of carbon-supported single atomic metals. First, glucose as chelating agent sequesters metal ions and binds to O-rich carbon support. Second, the chelated metal complexes secure metal atoms via the decomposed residues at elevated temperature. Third, CN_x species decomposed from melamine at higher temperature capture metal atoms to generate M-N_x moieties incorporated in the pyrolyzed carbon substrate. (B) HAADF-STEM image and EELS mapping images of Fe, N and overlaid Fe and N. Scale bar, 2 nm. Reproduced with permission from Zhao et al.[62] Copyright 2019 Nature Publishing Group. (C) The preparation route to single atomic atoms on nitrogen-doped graphene by a two-step mixing and annealing process with GO as precursor. Reproduced with permission from Zhang et al.[66] Copyright 2017 American Chemical Society.

3.1.2. GO as precursors

GO is an oxidized form of graphene and it is typically prepared by the oxidation of graphite followed by solution-phase exfoliation.[67] Because of the solution-based processing of GO, it has desirable manufacturability for scalable production and therefore has become one of the most popular starting materials to graphene-based nanomaterials for wide ranges of application areas, especially those where mass-production is required such as energy storage, catalysis, composite materials and coating.[24,68] The surface of graphene oxide is enriched with a high density of oxygen functional groups, including carboxyl, hydroxyl, carbonyl and epoxy, and these functional groups provides handful opportunities for surface modification and functionalization. To date, research on GO has mainly focused on their restoration by chemical or thermal reduction to pristine graphene alternatives (reduced graphene oxide, rGO) for applications in electronics, electrocatalysis, energy storage.[69-71] Recently, the intrinsic defects in rGO resulting from the removal of carbon-containing by-products such as CO and CO_2 gas during the reduction process have been used to stabilize single atomic metals.[25] The synthetic procedure typically involved simple two-step treatments (Fig. 5C).[66] The first step was the mixing of metal precursor and GO in aqueous solution with the negatively charged functional groups on GO providing anchoring sites for the metal ions. After being freeze-dried to prevent the restacking of GO nanosheets, the mixture was annealed in NH_3 atmosphere at high temperature, during which GO was reduced to rGO and nitrogen dopants were introduced into the carbon lattices as the effective binding sites for the individual metal atoms. It is critical to precisely control the amounts of metal precursor added in order to achieve maximized activity while preventing the metal aggregation. Unlike other carbon precursors, the reduction of GO to highly conductive rGO does not require the catalyzing effects of metals for the formation of conductive graphitized carbon and therefore excessive addition of metal precursors can be avoided, which is beneficial for the achievement of exclusive or predominant atomic metal dispersion. This method has been employed to prepare a variety of atomic metals (e.g., Fe, Co, Ni, Ru, Mn, Sc) dispersed in nitrogen-doped graphene.[25,66,72-75]

However, the preparation of G-SACs by thermally annealing the mixture of GO and metal precursors typically involves prolonged heating treatment, which is not only time- and energy-consuming, but also could cause aggregation of metal atoms. To this end, our group recently developed a facile and rapid strategy to prepare a series of monodispersed atomic transition metals (e.g., Co, Ni, Cu) by microwave irradiating the mixture of amine-functionalized GO and metal precursors with conventional microwave oven.[76] The microwave treatment can simultaneously induce the reduction of GO, the doping of nitrogen and the

incorporation of metal atoms into the graphene lattices. In addition, the microwave treatment is so rapid (~ 2 s) that there is less chance for metal aggregation to occur, resulting in the predominant presence of atomic species.

3.1.3. MOFs as precursors

With rich structural diversity, high porosity, tailorable compositions and versatile functionality, MOFs have been widely used as precursors to create nanostructured materials (e.g., porous nanocarbons, metal carbides, nitrides, phosphides and oxides) by high-temperature pyrolysis.[77] Compared to other approaches to nanostructured materials, the pyrolysis of MOFs offers controllability in size, shape, composition and porosity and allow the integration of diverse functionalities in one step.[78,79] Recently, the pyrolysis of MOFs has been demonstrated as an effective method to access G-SACs, and careful synthetic design is critical to ensure the uniform distribution and spatial separation of the metal sites in order to prevent their aggregation during pyrolysis.[55,80-90] For example, Yin et al. achieved the atomic dispersion of Co atoms on nitrogen-doped porous carbon by pyrolyzing Zn/Co bimetallic MOFs with homogeneous distribution of Zn and Co in the framework.[89] The addition of Zn^{2+} as metal nodes in the MOFs serve as spacer to dilute Co^{2+} and it can be evaporated away at high temperature due to its low boiling point. By carefully controlling the molar ratio of Zn and Co, catalysts with Co predominantly in the form of single atoms could be achieved. Motivated by these results, Wu et al. synthesized nitrogen-coordinated single Mn sites supported on graphitic carbon through the pyrolysis of Mn-doped ZIF-8 precursors.[91] Unlike the case of Co^{2+}, Mn^{2+} cannot easily exchange with Zn^{2+} in ZIF-8 and therefore only a limited number of atomic Mn sites were introduced into the carbon matrix by the one-step pyrolysis treatment. In order to increase the Mn loading, the pyrolyzed products with a high degree of microporosity was further used as host materials to absorb additional metal and nitrogen sources, followed by secondary thermal activation (Fig. 6A). With such a two-step doping and adsorption strategy, the atomic Mn loading was significantly increased, resulting in excellent catalytic activity.

The preparation of atomically dispersed noble metals (e.g., Ru, Pt, Au) by the strategy of converting the atomically dispersed metal nodes *in situ* from MOFs was hindered as these metals were rarely used as the metal nodes of MOFs. To circumvent this limitation, Wang et al. utilized the uncoordinated -NH_2 group on the skeletons of MOFs structure as the Lewis base to immobilize Ru precursor. Benefited from the strong interaction between the lone pair electrons and *d*-orbital of Ru ion, single Ru sites were prepared without obvious aggregation

during high-temperature pyrolysis, while Ru clusters were found in the sample without the assistance of -NH_2 groups.[92] Zhao et al. found that the metal precursor need not to be pre-mixed within the MOF. Rather, they developed a gas-migration strategy to access a series of metal atoms (Cu, Co, Ni) via direct thermally emitting from bulk metals and the subsequent trapping on MOF-derived nitrogen-rich carbon with the assistance of NH_3.[84] This gas-migration strategy is general in producing different types of atomic metals and easy to scale up as it avoids the complex operating steps and sensitive conditions encountered in the conventional method. With the similar strategy, Sun and coworkers reported a metallorganic gaseous doping method to synthesize single Fe atoms by evaporating iron organic compound of ferrocene and trapping into ZIF-8 precursors placed at the downstream during thermal activation.[93] Besides MOF-derived nanocarbon, graphene oxide was used as the trapping agent to anchor atomic Pt via the thermal emitting method.[94]

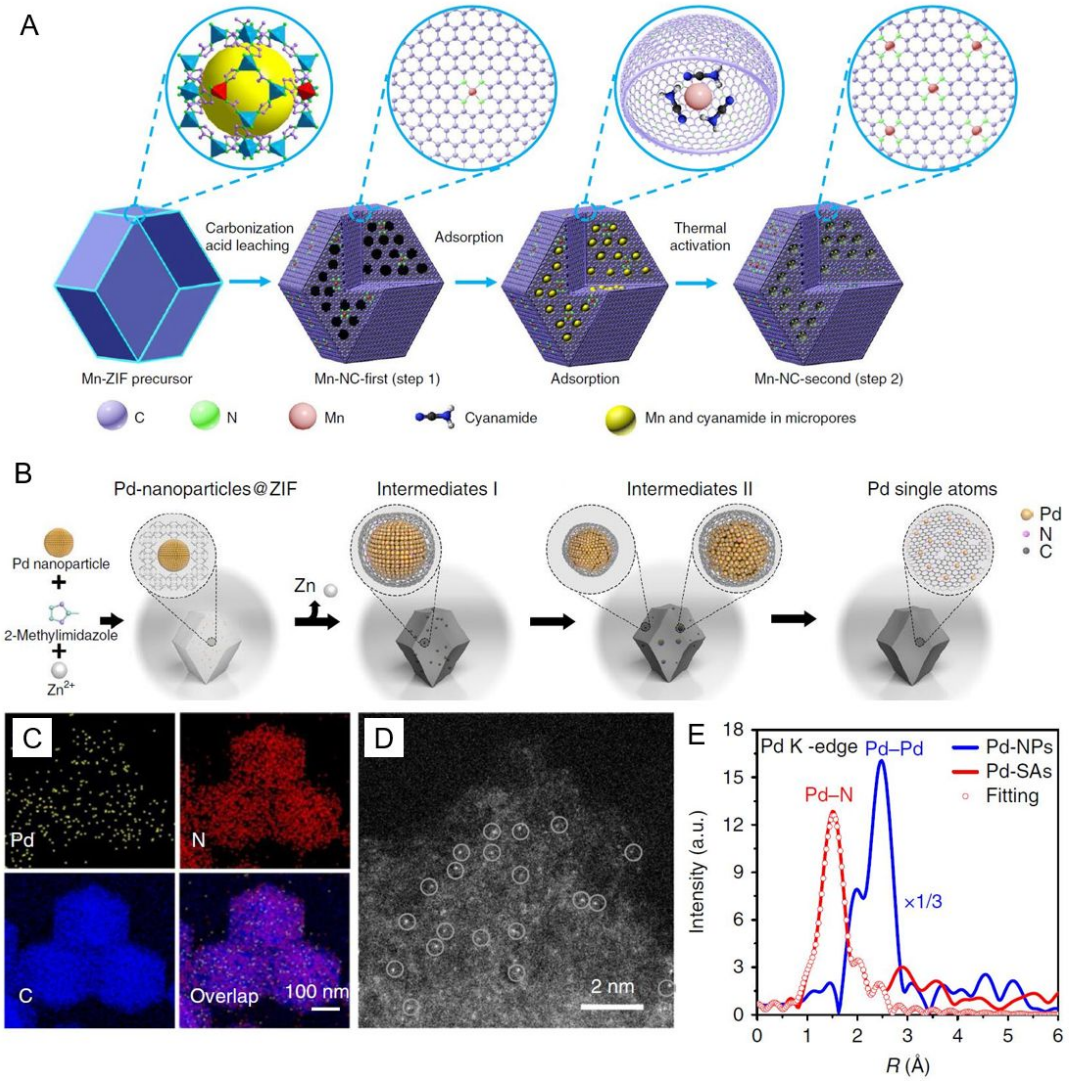

Fig. 6 (A) Schematic for the synthesis of atomically dispersed MnN_4 sites. In the first step, Mn-doped ZIF-8 were carbonized and leached with acid to prepare a partially graphitized

carbon host with optimal nitrogen doping and microporous structures. In the second step, additional Mn and N sources were adsorbed into the carbon host by a thermal activation to generate increased density of MnN_4 active sites. Reproduced with permission from Li et al.[91] Copyright 2018 Nature Publishing Group. (B) Scheme of the transformation of nanoparticles to single atoms and structural characterizations of Pd single atoms. (C) Energy dispersive X-ray spectroscopy elemental mapping results of Pd, N and C, showing their uniform distribution. (D) HAADF-STEM image of Pd single atoms. (E) Fourier transforms of k^3-weighted Pd K-edge EXAFS experimental data for Pd nanoparticles and Pd single atoms, showing the coordinating atoms adjacent to Pd atoms before and after pyrolysis. Reproduced with permission from Wei et al.[86] Copyright 2018 Nature Publishing Group.

Taking a step further, Yang et al. reported that Ni nanoparticles within MOF-derived N-doped carbon can be transformed into Ni single atoms through a thermal diffusion mechanism, during which the Ni nanoparticles could break C-C bonds to generate pores on the surface and at the same time the Ni atoms split from the nanoparticles could be bound to the N-rich defects due to the strong M-N interaction, resulting in the atomization of Ni nanoparticles.[95] In another work, Li and coworkers found that noble metal nanoparticles (Pd, Pt, Au) embedded in N-doped carbon derived from ZIF-8 can be transformed into single atoms at high temperature in an inert atmosphere (Fig. 6B).[86] The dynamic process for the transformation was directly observed by *in situ* environmental TEM. Specifically, ZIF-8 nanocrystals with embedded metal nanoparticles were heated at 900 °C under an inert atmosphere for 3 h and the morphologic evolution of the nanocomposite during different heating stages was recorded by STEM. The metal nanoparticles firstly grew larger and the size distribution became less homogeneous. Subsequent heating led to the amorphization of the metal nanoparticles and the decrease in the number of nanoparticles. After extensive pyrolysis, the remaining metal nanoparticles were digested within the substrate. Characterizations by the energy dispersive X-ray spectroscopy analysis, AC-STEM and EXAFS confirmed that the metal atoms were atomically dispersed in the carbon matrix (Fig. 6C-E). Detailed experimental studies by TEM and DFT calculations revealed that the high temperature transformation from metal nanoparticles to metal atoms was driven by the formation of $M\text{-}N_4$ moiety that is more thermodynamically stable than the metal nanoparticles.

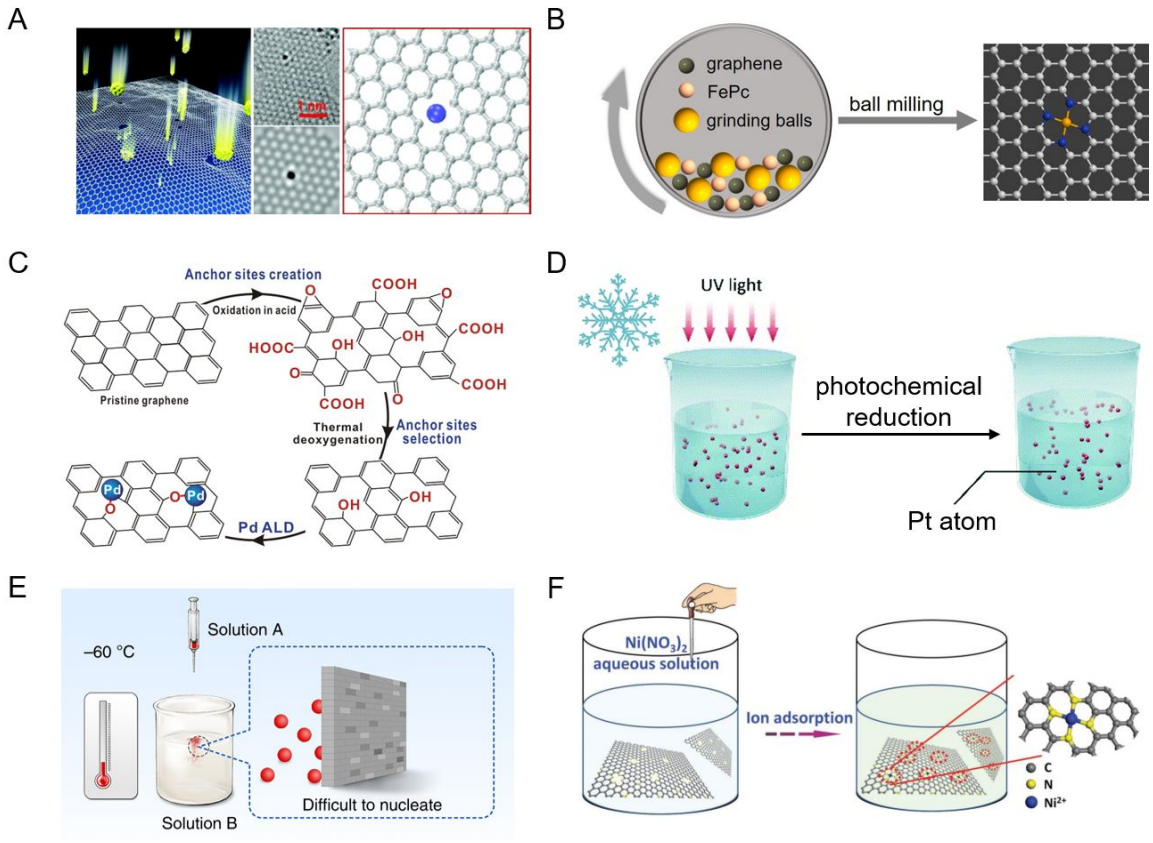

Fig. 7 Summary of synthetic strategies toward G-SACs. (A) HRTEM image, simulated image and atomic model of a Pt atom trapped in a di-vacancy of graphene. The left panel shows the schematic illustration of the metal ions irradiating graphene surface. Reproduced with permission from Wang et al.[29] Copyright 2012 American Chemical Society. (B) Schematic illustration of the ball milling approach to graphene-supported FeN_x moieties. (C) Schematic illustration of Pd atoms on graphene synthesized via a two-step process of anchoring sites creation and Pd ALD. Reproduced with permission from Yan et al.[96] Copyright 2015 American Chemical Society. (D) Schematic for the synthesis of atomically dispersed Pt by the ultralow-temperature photochemical reaction, during which the nucleation process of isolated atoms was prevented. Reproduced with permission from Wei et al.[97] Copyright 2019 Royal Society of Chemistry. (E) Schematic of the ultra-low temperature solution reduction process. The nucleation of reduced metal atoms can be significantly suppressed mainly due to the sluggish thermodynamics and kinetic process. Reproduced with permission from Huang et al.[98] Copyright 2019 Nature Publishing Group. (F) Schematic illustration of surface immobilization of transition metal ions on N-doped graphene via ion adsorption. Reproduced with permission from Bi et al.[99] Copyright 2018 Wiley-VCH.

3.2. Electron/ion irradiation

High-energy electron/ion bombardment has been demonstrated as an effective method to generate defects and vacancies in graphene, which are then able to trap mobile transition metal atoms. A variety of metal atoms (e.g., Fe, Cu, Co, Pt) have been successfully incorporated into the graphene lattices by this approach.[29,100] For example, Wang et al. developed a two-step process to dope graphene with Fe atoms: create carbon vacancies using energetic Au or B species ejected from laser ablation and fill these vacancies with Fe atoms by focused ion beam in the presence of Fe precursor (Fig. 7A).[29] It was suggested that the defect structure was affected by the energy and the incident angle of the bombarding species and therefore the refinement of the process was important to selectively generate vacancies for hosting metal dopants. Another related study showed that focused electron beam irradiation using TEM operated at an accelerating voltage of 80 kV was able to generate vacancies for metal doping in graphene with 10 × 10 nm^2 spatial control.[100] Metal atoms were most frequently observed at mono-vacancy and di-vacancy sites of graphene, and in some cases at topological defects. This method has the advantage of enabling the *in situ* study on the structure of the metal atoms and their migration behaviors.[101] However, the irradiation method lack the capability of mass production and its application for catalysis has yet to be demonstrated.

3.3. Ball milling

Ball milling is a common technique in the powder production industry and it is a process where the moving balls apply their kinetic energy to the materials, reconstructing the chemical bonds of materials and producing fresh surfaces. In addition, a high-energy ball milling process has the capability to create a local high temperature up to 1000 °C and high pressure up to several GPa, and it has been demonstrated as a powerful tool for the synthesis and modification of materials, such as organics and carbon-based nanomaterials.[102] For instance, ball milling has been applied for the exfoliation of graphite into graphene as well as the fragmentation and chemical functionalization of graphene.[103] More recently, Deng et al. used ball milling approach to synthesize well dispersed single atomic FeN_4 moieties within graphene matrix at a large quantity with iron phthalocyanine (FePc) and graphene nanosheets as precursors (Fig. 7B).[33] For the formation mechanism, it was proposed that the outside macrocyclic structure of FePc could be destroyed by ball milling, leaving the residual isolated FeN_4 center to interact with the defective sites of graphene, meanwhile the adjacent carbon atoms of FeN_4 could further reconstruct to finally form the graphene-embedded FeN_4 centers. The atomic Fe content was estimated to be ~ 2.7 wt% by inductively coupled plasma (ICP)

and further increasing the metal loading would lead to agglomeration. The generality of this method to prepare various atomic 3*d* transition metals (e.g., Mn, Fe, Co, Ni, Cu) within graphene lattices was demonstrated later by the same group.[104]

3.4. Atomic layer deposition

Atomic layer deposition (ALD) is a promising bottom-up technique to prepare catalysts with atomic precision. During the fabrication process, a substrate is alternately exposed to a series of reactive precursors, which react in a self-limiting manner to deposit materials in an atomic layer-by-layer fashion.[105] As the technique is based on chemisorption, deposition only happens on reactive surface sites and therefore it is possible to realize area-selective ALD. When graphene nanosheets are used as substrate for dispersing single atomic metals by ALD, they need to be pre-treated to introduce nucleation sites for selective deposition. Yan et al. reported the synthesis of graphene-supported Pd single atoms by the ALD technique (Fig. 7C).[96] The generation of anchoring sites on perfect graphene nanosheets was achieved by firstly oxidizing graphite into graphite oxide, followed by thermal exfoliation and deoxygenation through high-temperature reduction to precisely tune the type and amounts of surface oxygen functional groups. It was suggested that isolated phenols or phenol-carbonyl pairs on the graphene were the primary anchoring sites for metal atom deposition during ALD. With a similar procedure, Sun et al. fabricated Pt atoms on oxygenated graphene nanosheets and found that the size, density and loading of Pt on graphene can be precisely controlled by adjusting the number of ALD cycles.[106] Moreover, nitrogen-doped graphene has also been demonstrated as an effective substrate to support Pt atoms with enhanced interaction between metal and N sites.[107,108] However, due to the scalability and cost issues, the capability of ALD technique to produce catalysts for commercial applications is still limited in its current format.[8]

3.5. Photochemical reduction

Photochemical reduction chemistry involves the absorption of photons and electronically excited states and it has been widely employed to synthesize nanocrystals.[109] Recently, Wu and coworkers developed an iced-photochemical reduction method to synthesize Pt single atoms (Fig. 7D). H_2PtCl_6 aqueous solution was firstly frozen to yield an ice layer with a homogeneous distribution of Pt precursor and then the frozen solution was exposed to UV irradiation to reduce Pt precursor into Pt atoms.[110] During the photoreduction process, the ice lattice confined the dispersed reactants and therefore suppressed nucleus

formation. Subsequently, the melted solution containing Pt atoms was mixed with different types of substrates such as defective graphene that provided anchoring sites to stabilize Pt atoms. The same group later developed an ultralow temperature photoreduction process to synthesize Pt single atoms by firstly UV-irradiating H_2PtCl_6 precursor in an antifreeze solution containing ethyl alcohol and water at – 60 °C and then mixed with nitrogen-doped mesoporous carbon.[97] The ultralow reaction temperature can effectively prevent the nucleation and aggregation of isolated metal atoms in solution. Wang et al. developed a modified photoreduction process, in which $PtCl_6^{2-}$ ions were firstly absorbed on nitrogen-doped porous carbon with rich absorption sites (e.g., nitrogen and oxygen heteroatoms), high porosity and abundant defects that are beneficial for the absorption of metal ions.[111] The carbon with absorbed $PtCl_6^{2-}$ ions in solid state was then irradiated with UV light to realize the reduction of $PtCl_6^{2-}$ ions to Pt atoms supported on carbon. The as-prepared Pt atoms were well-dispersed on the carbon without formation of clusters or nanoparticles. The photochemical reduction process is considered to be green and simple, but it is mainly used to synthesize noble metal atoms. Its generality for synthesizing non-noble metal atoms remain questionable considering the limited reducing capability of UV light.

3.6. Solution-phase synthesis

The rapid nucleation and growth of solid-state products during solution-phase synthesis make the formation of ultrafine nanoclusters or metal single atoms challenging. Recent research efforts suggest that metal single atoms can be obtained by solution-phase synthesis provided that the kinetics for the nuclei formation could be significantly reduced or strong metal-support interaction could be introduced. Wu et al. developed a low-temperature (– 60 °C) solution synthesis of single atomic Co supported on nitrogen doped mesoporous carbon through the liquid-phase reduction of $CoCl_2$ with hydrazine hydrate using a water/alcohol mixed solvent having low freezing point (Fig. 7E).[98] The low reaction temperature was found to be critical in suppressing nuclei formation to ensure atomic metal dispersion. Zhang et al. immobilized single atomic Pt onto the nitrogen-doped carbon nanocages by simply dispersing the nanocarbon into H_2PtCl_6 aqueous solution, followed by filtration, washing and mild drying.[112] Combined experimental and theoretical investigations suggested that the micropore trapping and nitrogen anchoring from the nanocarbon substrate was beneficial for trapping the metal ion and the derived Pt single atoms. Such impregnation-adsorption method was employed to synthesize atomically dispersed Ni and Cu by immersing nitrogen-enriched graphene in the corresponding solution of metal precursors, followed by

mild post-treatments (Fig. 7F).[99,113] Besides nitrogen dopants, graphene functionalized with nitrile groups and carboxy groups was employed to anchor metal atoms (Cu and Fe) as the nitrile groups and carboxylated groups could serve as strong and selective ligands for the metal ions.[114] The solution-phase synthetic method is simple, general and potentially suitable for mass production.

4. Identification of atomistic structure by synchrotron X-ray absorption spectroscopy

Recent years have witnessed much progress in the synergistic efforts of theoretical and experimental studies in the rational design of high-performance electrocatalysts.[2] At the foundation of such design lays the catalyst's atomistic and electronic structure that dictates the reaction mechanism and intrinsic activity trends. However, the unambiguous identification of the atomistic structure of the active sites in G-SACs represents a serious challenge largely due to the non-crystallographic ordering of the metal atoms and the heterogeneity in structure and composition.[43] Several characterization techniques, such as STEM, Mössbauer spectroscopy, X-ray photoelectron spectroscopy (XPS) and electron paramagnetic resonance (EPR) spectroscopy, have been used to probe the atomistic or electronic structures of SACs.[8,13,46] Recently, a blossoming interest has been paid to synchrotron X-ray absorption spectroscopy (XAS), which can provide valuable information about the coordination environment and the chemical state of the probed atom in an element-selective way. Moreover, with the capability of hard X-rays to penetrate the electrode through the catalyst/electrolyte interface, XAS allows the study of the dynamic process of electrochemical reactions under *in-situ*/*operando* conditions, which is essential for establishing a more precise structure-activity relationship and thus a fundamental understanding of the key factors governing these reactions. Rapidly increasing number of publications on these subjects have proved XAS to be a well-suited and powerful technique for characterizing G-SACs.[25,43,44,46,115] Nonetheless, unambiguously extracting exact atomistic and electronic structure by XAS remains neither trivial nor straightforward and the complementary use of different techniques is often needed. Here we focus our discussion on recent efforts in the employment of XAS in identifying the atomistic and electronic structure of the active sites in G-SACs. By examining the advantages and disadvantages of different XAS analysis methods, we describe a global strategy for the structural identification by XAS that can reduce loose ends to a minimum, likely serving as a general guide for future studies facing the structural characterization of G-SACs.

4.1. Brief introduction to XAS basics

XAS measures the X-ray absorption coefficient of a material as a function of X-ray photon energy (Fig. 8A). The incident X-ray photon energy scans through a specific element threshold to excite inner-shell electrons to the unoccupied continuum level (Fig. 8B), resulting in a sharp rise at certain energies (the absorption edge) and a series of oscillatory structure that contains unique signature of a given material. XAS can be roughly divided into two regions (Fig. 8A), the X-ray absorption near edge structure (XANES) and extended X-ray absorption fine structure (EXAFS) for their different origins, and thus they will be treated differently with emphasis on different information that can be provided. Specifically, in the frame of the single/multiple scattering approach (Fig. 8C), the EXAFS oscillations obtained by data reduction can be interpreted by the well-known standard EXAFS equation expressed as the sum of a series of sine-function-like scattering signals from different coordination shells.[116] By modeling and least-squares curve fitting the experimental EXAFS data, local structure such as interatomic distance and coordination number around the probed atoms can be determined. On the other hand, the XANES region contains much chemical information and is generally not as readily interpreted as EXAFS. The edge energy position exhibits sensitive dependence on the formal oxidation state of the probed atom (chemical shift), which can be quantitatively identified using reference compounds with known oxidation states. The XANES spectral shape and edge energy position are also sensitive to ligand types and the three-dimensional coordination environment around the central absorbing atom. Shoulder features on the edge of the XANES spectrum are sometimes introduced for square-planar configuration of the ligand atoms. The pre-edge features are sensitive to the coordination symmetry and the formal oxidation state of the probed atom. For instance, the pre-edge peak for 3*d* transition metals can result from quadrupolar allowed transition (1*s*-3*d*) or from 3*d*-4*p* orbital mixing induced by a noncentrosymmetric chemical environment where the peak intensity is directly proportional to the coordination deviation of the absorbers from centrosymmetry. In general, XANES contains more abundant structural information and can be described qualitatively in terms of coordination chemistry, molecular orbitals, band structure and multiple scattering. Interested readers are referred to more detailed reviews and books on XAS theory and its application in catalysts.[116-118]

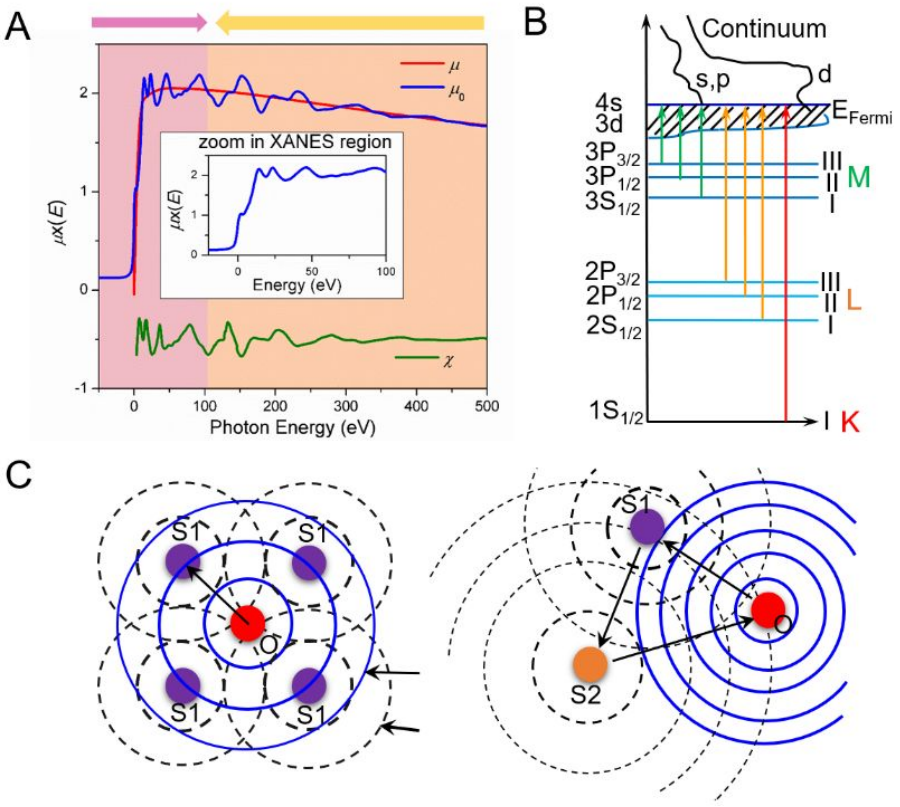

Fig. 8 Brief introduction to XAS basics. (A) The XAS spectrum consisting of absorption edge and a series of oscillatory structures. The conventional division between XANES and EXAFS region is indicated by different colors. The inset shows the magnified XANES region. (B) X-ray absorption edges nomenclature and their relationship with the corresponding excitation of core electrons. (C) The schematic illustration of the single (left) and multiple (right) scattering process of the excited photoelectrons. The EXAFS oscillations can be regarded as these originate from the constructive and destructive interferences between the scattered photoelectron waves near neighbor atoms (denoted as S1 and S2) with the outgoing photoelectron waves at the absorbing atom (denoted as O).

4.2. Probing local structure by EXAFS

EXAFS has been extensively employed to decipher the local bonding environment in various materials, attributed mostly to the fact that the Fourier transform (FT) of the EXAFS spectra enables the separation of backscattering atoms directly by a path-length criterion.[116] Specifically, a qualitative estimate of the coordination shells surrounding the absorbing atom can be made according to the radial locations of the EXAFS peak distributions in the FT modulus. Further quantitative structural information (e.g., bond length, coordination number and bond disorder) can be obtained by a least-squares curve fit of the EXAFS data to the standard EXAFS equation. However, a necessary step of EXAFS analysis is to pre-select and

test the identity of the backscattering atom through trial-and-error fit; this process is a black box and usually suffer from large uncertainty and artificiality. Moreover, the experimental XAS data of G-SACs often has a low signal-to-noise ratio and short *k*-range, which can make the pre-selection of atom type more difficult. For FT, while the identification of the backscattering atoms is relatively straightforward if the coordination shells constitute only one type of atoms at one distance (as shown in Fig. 9A, C), the analysis is substantially complicated with different types of atoms at one distance (where the FT is characterized a single peak as shown in Fig. 9B, D).[119] In contrast to FT, the wavelet transform (WT) of EXAFS allows to resolve the backscattering atoms in both *k*- and *R*-spaces that provide the elemental nature and radial distance resolutions, respectively. From Fig. 9E, F, it can be appreciated that the type of backscattering atoms indistinguishable in the FT peak can be readily distinguished based on the *k* locations of the intensity maxima in the WT distribution, without any fitting process required. Therefore, the *R* and *k* space information given by WT can greatly ease the discrimination between heavier (i.e., metal atoms) and lighter backscattering atoms (i.e., C, N and O) even if they overlap at the same distance from the central atom, which is the frequently encountered situations for atomic structural investigation in G-SACs.

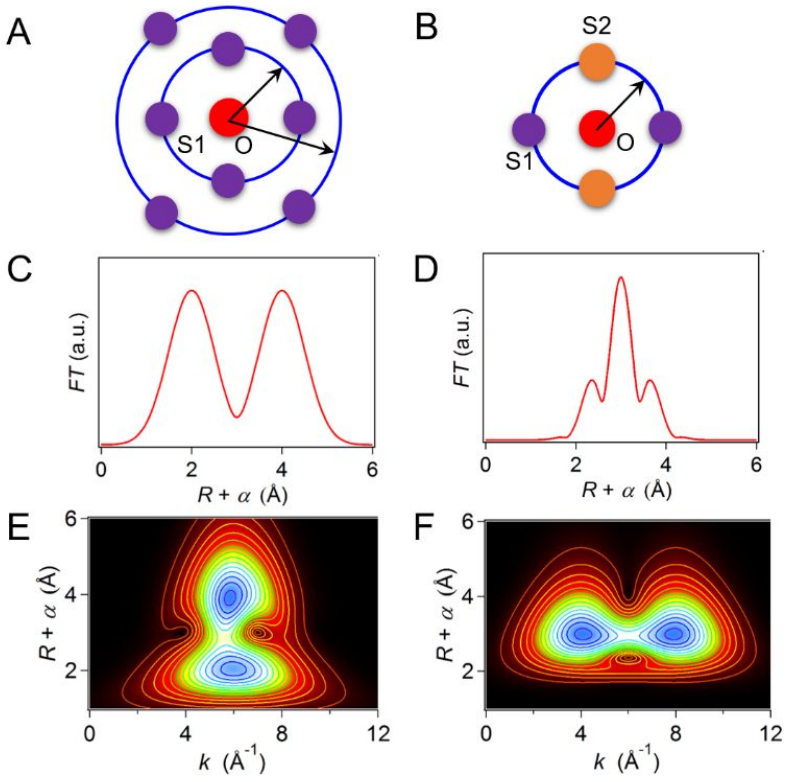

Fig. 9 Comparison between EXAFS FT and WT. (A-B) Schematic view of two different coordination configurations for one type of backscattering atom (denoted as S1) located at

two distances (so-called two shells) and two types of backscattering atoms (denoted as S1 and S2) overlapping at one distance (so-called one shell) around the central absorbing atom (denoted as O). (C-F) The simulated EXAFS-FT moduli (C-D) and EXAFS-WT distributions (E-F) corresponding to the two coordination configurations as shown in (A-B), respectively.

We recently synthesized a series of monodispersed atomic transition metals of Co, Ni and Cu embedded in nitrogen-doped graphene.[76] The EXAFS-FT profiles feature a single main peak at ~1.6 Å and another minor peak at ~2.1 Å (Fig. 10A). While the main peak at ~1.6 Å can be readily ascribed to the bonding between metal and nearest-neighbor light atoms, the assignment of the minor peak at ~2.1 Å is rather difficult mainly because in this radial range the peak arising from next nearest-neighbor light atoms overlaps substantially with the peak from the metal-metal bond. The metal-metal peak is regarded as an indicator for the presence of metal-derived crystalline structure. Nevertheless, the WT of the weighted EXAFS signals clearly reveal a single intensity maximum at ~ 4.0 $Å^{-1}$ that can be assigned to the metal-N/O/C contributions (Fig. 10B), in marked contrast to the intensity maxima at ~7.0 $Å^{-1}$ resulting from the metal-metal contributions, confirming the atomic dispersion of the metals in the samples. Another example is concerning the comparison of the EXAFS signals for Co-NG with Co atomically dispersed on N-doped graphene and Co-G without N doping.[72] The FT moduli of EXAFS signals for both the Co-NG and Co-G show only one single main peak at ~1.6 Å in *R*-space (Fig. 10C), and the WT distributions correspond to one intensity maximum at 3.4 $Å^{-1}$ for the Co-NG and one at 3.2 $Å^{-1}$ for Co-G (Fig. 10D). Theoretical calculation indicates that the location of WT maximum is largely affected by the type of backscattering atoms (i.e., 3.2 $Å^{-1}$ for Co-C path, 3.5 $Å^{-1}$ for Co-N path, 4.3 $Å^{-1}$ for Co-O path, and 6.8 $Å^{-1}$ for Co-Co path). As a result, the WT maximum A at 3.2 $Å^{-1}$ for the Co-G can be associated with the Co-C path, and 3.4 $Å^{-1}$ for the Co-N path within the Co-NG. A least-squares curve fitting analysis was carried out for the first coordination shell of Co to confirm the validity of the above WT-EXAFS interpretation. Thus, combined WT and FT is highly useful for the discrimination of the single atomic dispersion in G-SACs during EXAFS analysis of G-SACs.

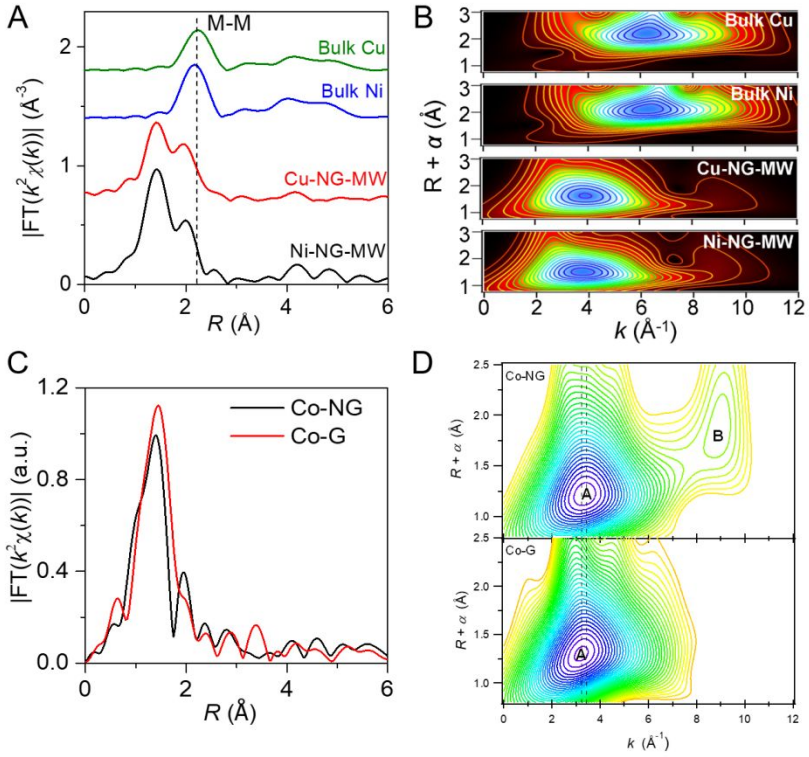

Fig. 10 EXAFS-FT and EXAFS-WT analysis of the coordination environment for 3*d* transition metal atoms in M-N-C catalysts. (A) FT magnitudes of the K-edge phase-uncorrected EXAFS signals of Ni-NG-MW and Cu-NG-MW along with bulk metals. The vertical dashed line highlighted the position of the M-M peaks. (B) WT for the k^2-weighted EXAFS signals of Ni-NG-MW, Cu-NG-MW and bulk metals with optimum resolutions at ~ 2.0 Å. Reproduced with permission from Fei et al.[76] Copyright 2018 Wiley-VCH. (C) FT magnitudes of the Co K-edge phase-uncorrected EXAFS signal in *R* space. (D) WT in both *k*- and *R*-spaces for Co-NG and Co-G. Reproduced with permission from Fei et al.[72] Copyright 2015 Nature Publishing Group.

In the past several years, WT has been widely used to characterize many different types of materials. Besides G-SACs, WT is also suitable to SACs supported on non-carbon substrates.[120] WT has been used to preclude the presence of metal cluster, and it can also be used to detect the existence of weak metal-metal interaction in sub-nano clusters.[121] Therefore, complement of FT with WT is strongly recommended in future EXAFS analysis.

4.3. Electronic and 3D geometric structure by XANES

At the energy region of XANES, the single scattering approximation breaks down and many processes contribute in a non-negligible way, including many-body effect, multiple scattering effect, polarization effect and so on, which make the signal at the relevant energies

very sensitive to the 3D atomic, electronic and magnetic structures. Therefore, XANES is highly valuable in resolving the electronic and 3D geometric structure in G-SACs. For 3*d* transition metals, two significant pre-edge features can often be observed. The peak at lower energy is due to quadrupolar-allowed 1*s*-3*d* transition or 3*d*-4*p* orbital hybridization and its intensity is directly proportional to the coordination deviation of the photo-absorbers from centrosymmetry, while the peak at higher energy arises from a $1s \rightarrow 4p_z$ shakedown transition and acts as a fingerprint for a square-planar configuration with high D_{4h} symmetry. For example, Zitolo et al. revealed slight differences in the XANES spectra of a pyrolyzed Fe-N-C catalyst and non-pyrolyzed Fe(II) phthalocyanine (Fe(II)Pc) (Fig. 11A), which suggests a valence state of +2 for the Fe sites in Fe-N-C.[43] However, the pre-edge feature at 7118 eV shows a strong intensity for Fe(II)Pc that has a square-planar configuration but is absent in the pyrolyzed Fe-N-C, thus revealing a broken D_{4h} symmetry with axial ligands. Similar results for the two pre-edge features were reported in a Co-N-C catalyst (Fig. 11B).[25] Yang et al. also used XANES to study the oxidation state and coordination structure of atomic Ni catalysts with and without the addition of a sulfur precursor (denoted as A-Ni-NG and A-Ni-NSG).[46] Interestingly, a comparison of the inflection point of the second-derivative spectrum of Ni K-edge XANES suggests that the oxidation state of the Ni atoms in A-Ni-NG and A-Ni-NSG was +1 with a $3d^9$, $S = 1/2$ electronic configuration, which could result from the lower electronegativity of pyridinic N and S relative to the pyrrolic N in Ni(II)Pc (Fig. 11C). Furthermore, as compared to Ni(II)Pc, the increased intensity in the pre-edge peak A and the reduced intensity in the pre-edge peak B for A-Ni-NG and A-Ni-NSG both indicate that the Ni atoms possess distorted D_{4h} symmetry.

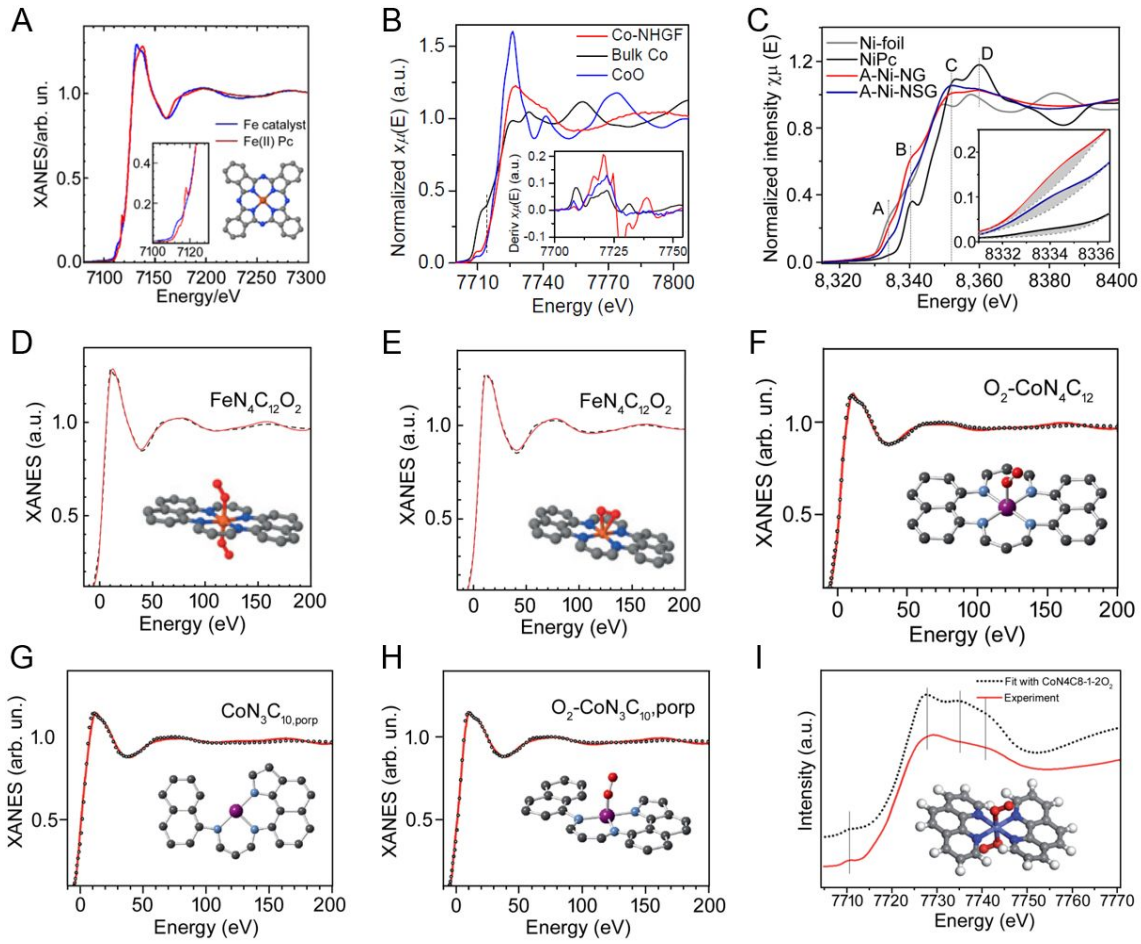

Fig. 11 Structural identification of single metal moieties in various M-N-C catalysts by XANES spectroscopy. (A-C) The experimental K-edge XANES spectra of Fe-N-C, Co-N-C and Ni-N-C and reference samples. The inset in (A) and (C) shows a magnification of the pre-edge feature. The inset in (B) shows the first derivative curves. Reproduced with permission from Zitolo et al.[43] Copyright 2015 Nature Publishing Group. Reproduced with permission from Fei et al.[25] Copyright 2018 Nature Publishing Group. Reproduced with permission from Yang et al.[46] Copyright 2018 Nature Publishing Group. (D-E) Comparison between the K-edge XANES experimental spectra (black dashed lines) of Fe-N-C and the theoretical spectra calculated with the depicted porphyrinic structures (solid red lines). Reproduced with permission from Zitolo et al.[43] Copyright 2015 Nature Publishing Group. (F-H) Comparison between the K-edge XANES experimental spectra (black dashed lines) of Co-N-C and the theoretical spectra calculated with the depicted porphyrinic structures (solid red lines). In (G) and (H), two defective sites derived from the porphyrinic moiety by subtracting one or two nitrogen atoms were shown. Reproduced with permission from Zitolo et al.[44] Copyright 2018 Nature Publishing Group. (I) Comparison between the K-edge XANES experimental spectrum of Co-N-C (solid red line) and the theoretical spectrum (black dotted line) calculated

with the depicted pyridinic moiety. Reproduced with permission from Liu et al.[122] Copyright 2016 The Royal Society of Chemistry.

Besides the above qualitative analysis, XANES calculations and fits can be used to better identify the atomistic structure in G-SACs. XANES calculation has been used to resolve the structural configuration based upon a profile/shape comparison between the experimental and theoretical spectra, which includes the peak positions and their intensity relationship. This is based on the fingerprint of XANES to similar structural configurations despite possible slight differences in the bond distances and/or angles. On the other hand, XANES fitting is a method to extract quantitative structural information via an iterative minimization of the differences between the experimental XANES spectrum and many theoretical ones, which proceeds via varying iteratively the structure parameters (e.g., bond distances and bond angles) based on an initial given geometry until the convergence criteria are reached.[123,124] Therefore, XANES fitting can be considered as a refinement of the moiety used for XANES calculation and can also be used to confirm or discard a structural model. Zitolo et al. performed a thorough XANES fitting investigation of active site structure in their single atomic Fe-N-C catalyst.[43] They initially excluded a FeN_4 moiety enclosed in a graphene sheet and a FeN_{2+2} moiety bridging two graphene sheets, due to obvious discrepancies between the experimental and calculated spectrum. Then, they examined a porphyrin-like FeN_4C_{12} moiety and the agreement was improved. Substantial improvement over the whole energy range was obtained by including one O_2 in the end-on configuration. The inclusion of a second O_2 along the axial direction resulted in an excellent agreement between experimental and theoretical spectra (Fig. 11D). Besides, the same FeN_4C_{12} moiety with O_2 adsorbed side-on was also found to correctly reproduce the experimental spectrum (Fig. 11E). In a followed study, Zitolo et al. reported the identification of atomistic structure in a Co-N-C catalyst.[44] Similar to the Fe-N-C catalyst,[43] the porphyrin-like CoN_4C_{12} moiety with and without an end-on adsorbed O_2 was found to produce an excellent agreement between experimental and theoretical spectra (Fig. 11F). Additionally, two defective moieties, derived from the porphyrinic CoN_4C_{12} moiety by subtracting one or two nitrogen atoms, were also suggested as viable candidates (Fig. 11G, H). In another study, Liu et al. studied the structure of an atomic Co catalyst. Different from the porphyrinic moieties, their XANES calculation shows that the main features of the experimental spectrum could be reproduced by a pyridinic CoN_4C_8 moiety with the addition of two O_2 in end-on mode (Fig. 11I).[122]

4.4. Global XAS analysis strategy and application

XAS studies on G-SACs (and other types of SACs) were usually separated into two independent processes of EXAFS and XANES, with emphasis on atomic radial distribution and electronic structure, respectively. However, it is worth emphasizing that both EXAFS and XANES have a common structural origin and thus the derived structural information should keep consistent with each other. Based on this fact, it is strongly suggested to routinely make complementary uses of multiple XAS analysis approaches (i.e., EXAFS fitting, XANES simulation, XANES fitting, EXAFS calculation) in a global way, as schematically shown in Fig. 12A. In particular, qualitative EXAFS-WT comparison can be first used to identify the atomic distribution; then, quantitative EXAFS-FT fitting is used to extract interatomic distances and coordination number, which are crucial parameters to distinguish potential structural motifs and can facilitate the modeling of atomic structure used for XANES calculation. As compared to the radial atomic distribution detected by EXAFS, one of the greatest strengths for XANES is its high sensitivity to the spatial arrangement of the coordinating atoms. Detailed XANES analysis usually requires extensive theoretical calculation with various well-defined model structures. Also, EXAFS simulation can be used to assist the structural identification. Just as triangulation, the ultimate goal is to achieve a global consistency between EXAFS and XANES. Therefore, the as-described global XAS analysis strategy can allow the analyzers to efficiently and properly identify the structure of SACs with minimized uncertainty and artificiality.

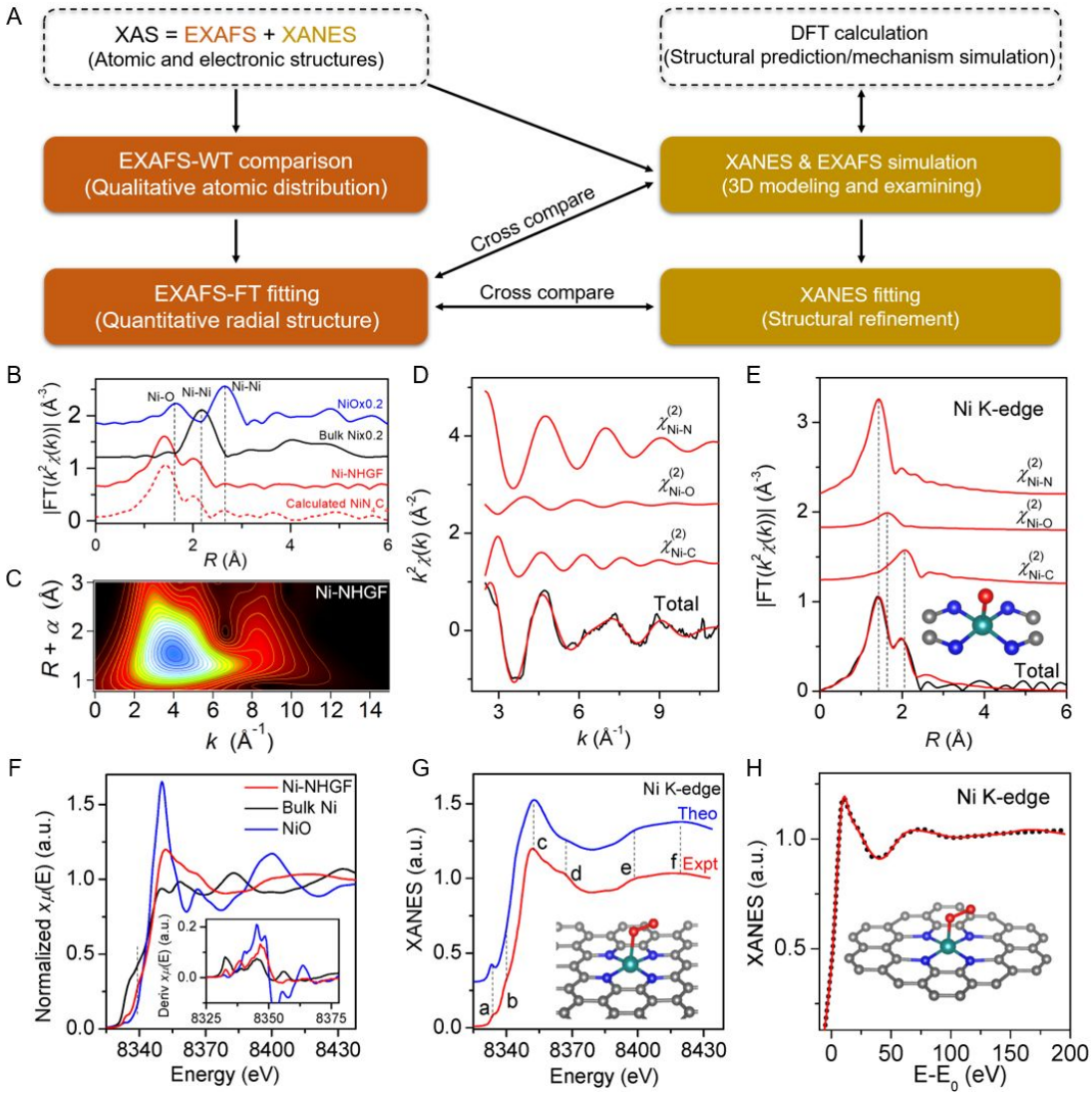

Fig. 12 Schematic presentation of the global XAS analysis strategy and its application to the structural identification of the atomistic sites in Ni-NHGF catalyst. (A) Global XAS analysis strategy consisting of various EXAFS and XANES analysis approaches. (B) FT magnitudes of the experimental K-edge EXAFS signals of Ni-NHGF along with reference samples (solid lines). The dashed lines represent calculated spectra based on a divacancy-based NiN_4C_4 moiety enclosed in the graphene lattice. (C) WT for the k^3-weighted EXAFS signals of Ni-NHGF. (D-E) Ni K-edge EXAFS analysis of Ni-NHGF in k (D) and R (E) spaces. Curves from top to bottom are the two-body backscattering signals included in the fit and the total signal (red line) superimposed on the experimental signal (black line). The inset shows the structural model of a NiN_4C_4 moiety. (F) The experimental Ni K-edge XANES spectra and first derivative curves (insets) of Ni-NHGF and reference samples. (G) Comparison between the experimental K-edge XANES spectra of Ni-NHGF and the theoretical spectra calculated with the depicted structure. (H) The best fit between the theoretical (solid red lines) and

experimental XANES spectra (black dotted lines) for Ni-NHGF. Reproduced with permission from Fei et al.[25] Copyright 2018 Nature Publishing Group.

Lately, we have conducted such a global and comprehensive XAS analyses toward the unambiguous identification of the MN_4C_4 (M = Fe, Co, Ni) moiety implanted in graphene lattice.[25] Taking the Ni case for instance, we firstly performed EXAFS-FT and EXAFS-WT analyses to confirm the exclusive atomic dispersion of Ni atoms. We found that the EXAFS-FT profile features a co-presence of a Gaussian-like main peak at 1.44 Å and a minor satellite peak at 2.01 Å (Fig. 12B). While the minor satellite peak overlaps partially with the Ni-Ni peak at 2.18 Å for bulk Ni, EXAFS-WT analysis detects only one intensity maximum at approximately 4.0 $Å^{-1}$ (Fig. 12C), which can be assigned to the M-N/O/C contributions. On the basis of the EXAFS-WT result, three backscattering paths of Ni-N, Ni-O and Ni-C were used to model the EXAFS signal by EXAFS curve fitting. The first coordination sphere of Ni was revealed to be a square-pyramidal configuration for the Ni-N/O bonding (Fig. 12D,E), with a second coordination sphere of about four C atoms, indicating a NiN_4C_4 moiety with one oxygen atom in the axial direction. On the other hand, the XANES spectrum indicates a valence state of +2 for Ni (Fig. 12F). Moreover, the rather weak intensity for the pre-edge peak (Fig. 12F), which is due to a $1s–4p_z$ shakedown transition characteristic for a square-planar configuration with high D_{4h} symmetry, indicates a broken D_{4h} symmetry and calls for axial ligands, which is in accordance with the EXAFS fitting results. Then, XANES calculation based on various possible NiN_xC_y moieties was applied to resolve the atomic-site structure. The porphyrin-based NiN_4C_{12} moiety and a pyridinic-N-based NiN_4C_8 moiety were excluded due to the large discrepancy observed between the simulated spectrum and the experimental spectrum. Another series of XANES simulation by embedding the NiN_4C_4 moieties in the 2D graphene lattice were examined, with substantially improved agreement. With the addition of one end-on dioxygen molecule in the axial position of the Ni centre, excellent agreement was obtained (Fig. 12G). XANES fitting based on the as-determined NiN_4C_4 moiety reveals that the calculated spectra match excellently with the experimental spectra (Fig. 12H), and the bond metrics are in good agreement with those determined by EXAFS analysis and DFT prediction. Together, these XANES analysis clearly demonstrate single atomic metal centers with four pyridinic N atoms and one adsorbed O atom in the first coordination sphere and four C atoms in the second coordination sphere, which is fully consistent with the EXAFS results. Lastly, EXAFS simulations based on such divacancy-based NiN_4C_4 moiety show that the simulated EXAFS spectra (dash lines in Fig. 12B) are

nearly identical to the experimental spectra. Therefore, the combination of EXAFS-WT, EXAFS-FT and XANES analyses on Ni-NHGF has achieved a global consistency and unambiguously identified the divacancy-based NiN_4C_4 moiety in the graphene lattices.

4.5. Monitoring dynamic processes by *in situ*/*operando* XAS

The real-time observation on the reacting single-atom sites via *in situ*/*operando* studies could provide in-depth insights into the dynamic changes in the atomic and electronic structures of the catalysts as a function of the applied potential, the complex reaction kinetics and mechanisms as well as the stability over time or potential. Benefited from the ability of X-ray photons to penetrate matter at the micrometer or even millimeter scale (depending on the photon energy) and the suitability of XAS to study the geometric and electronic structure of the catalysts, XAS hold a place of choice for catalytic *in situ*/*operando* studies of G-SACs.[125-128] Zitolo et al. studied the atomic and electronic structures of pyrolyzed Co-N-C and Fe-N-C catalysts during the ORR using *operando* XANES.[44] Upon increasing the potential, the main absorption edge for Co-N-C showed insignificant changes across the whole ORR potential range (Fig. 13A), suggesting that the Co moieties did not change structure. In contrast, Fe-N-C exhibited gradual shift toward higher energy (Fig. 13B), which indicates an increase of oxidation state and structural changes due to the reorganization of the N (or C) ligands and/or spin state. Besides, the authors used comparative *operando* XANES spectra collected in O_2-free or O_2-saturated electrolyte to detect the bonding of the active sites (Fig. 13C,D). While slight spectral changes were observed for Fe-N-C, large variation was detected at the white line peak region for Co-N-C. Analysis of the differential $\Delta\mu_{O_2\text{-}N_2}$ spectra of Co-N-C at 0.8 V revealed an active-site structure with four N atoms at 1.95 Å with or without an oxygen molecule adsorbed end-on at 2.22 Å. As oxygen comes exclusively from water activation in N_2-saturated electrolyte, these results suggest the formation of Co-O bond only in O_2-saturated electrolyte for Co-N-C and a formation of Fe-O bond probably in both O_2- and N_2-saturated electrolytes for Fe-N-C. However, the exact structural change induced by the redox switch remains unclear and will be of great interest in the future.

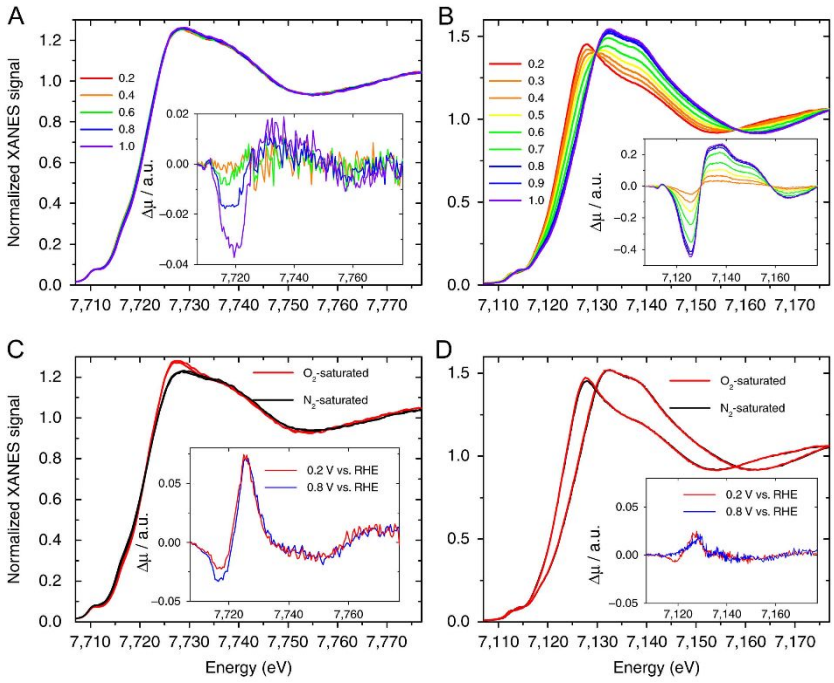

Fig. 13 *Operando* XANES studies during ORR process. (A-B) Metal K-edge XANES spectra taken in 0.5 M H_2SO_4 aqueous solution saturated with N_2 at ORR potentials for Co-N-C ($Co_{0.5}$) (A) and Fe-N-C ($Fe_{0.5}$) (B), respectively. The insets show differential Δμ XANES spectra relative to the spectrum recorded at lowest potential of 0.2 V. (C-D) Metal K-edge XANES spectra for Co-N-C ($Co_{0.5}$) (C) and Fe-N-C ($Fe_{0.5}$) (D) measured as a function of the saturating gas (O_2 or N_2) at either 0.2 V or 0.8 V versus RHE. Insets are Δμ spectra obtained by subtracting the normalized XANES spectra recorded in O_2-saturated to that recorded in N_2-saturated electrolyte at a fixed potential. Reproduced with permission from Zitolo et al.[44] Copyright 2017 Nature Publishing Group.

Yang et al. reported an A-Ni-NG catalyst with atomically dispersed monovalent Ni(I) atoms for CO_2RR.[46] They applied both the *operando* Ni K-edge XANES and EXAFS spectra to track the adsorption and activation of CO_2 on A-Ni-NG. The absorption edge position exhibited a positive shift of ~0.4 V under open-circuit voltage in CO_2-saturated $KHCO_3$ solution when compared to Ar-saturated electrolyte (Fig. 14A), indicating a slight oxidation of Ni sites that was interpreted as delocalization of the unpaired electron in the $3dx^2$-y^2 orbital and spontaneous charge transfer from Ni(I) to the carbon $2p$ orbital in CO_2 to form a $CO_2^{\delta-}$ species. The formation of Ni-C bond due to CO_2 absorption also caused a slight increase of the intensity for the first nearest-neighboring major peak at approximately 1.45 Å in EXAFS-FT (Fig. 14B). However, when a CO_2 reduction potential of -0.7 V versus RHE was applied, the Ni oxidation state was reduced based on the observation of a shift of the absorption edge

back to lower energy, which was ascribed to a recovery of low-oxidation-state Ni after one cycle of CO_2 reduction. Simultaneously, the major peak dominated by the Ni-N bond showed a shift of ~0.04 Å to longer lengths, ascribed to an elongation of the Ni-N bond that resulted from the displacement of Ni atoms out of the graphene plane due to the electron transfer from Ni atom to CO_2.

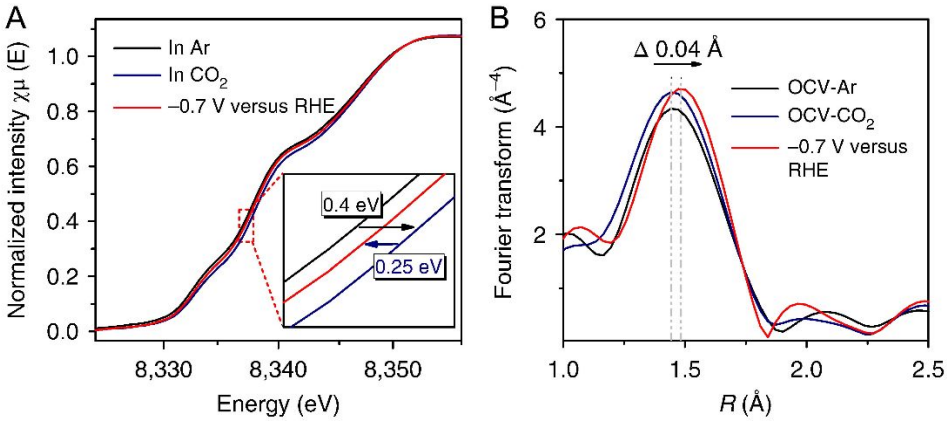

Fig. 14 *Operando* X-ray absorption spectroscopy of A-Ni-NG during CO_2 reduction process. (A) Normalized *operando* Ni-edge XANES spectra for A-Ni-NG at various biases (applied voltage versus RHE) in 0.5 M $KHCO_3$ aqueous solution at room temperature in atmosphere of Ar or CO_2. The inset shows the enlarged Ni K-edge XANES spectra. (B) EXAFS-FT spectra (without phase correction) of A-Ni-NG under open-circuit voltage in Ar (OCV-Ar) and CO_2 (OCV-CO_2), and at -0.7 V (versus RHE), in which an expanded Ni-N bond was detected. Reproduced with permission from Yang et al.[46] Copyright 2018 Nature Publishing Group.

5. Applications for electrochemical energy conversion

Electrochemical energy conversion has been considered as one of the most promising routes for the construction of a sustainable and environmental-friendly energy cycle.[129] The development of high-performance and inexpensive electrocatalysts is of vital importance to increase the reaction rate, efficiency, selectivity and stability of energy conversion technologies, such as water splitting, fuel cells, CO_2 conversion, N_2 reduction and metal-air batteries. As stated above, the ultrahigh surface area, superior electrical conductivity, excellent (electro-) chemical stability make G-SACs highly attractive as electrocatalysts for energy conversion applications. Below, we will summarize recent progress in the applications of G-SACs in ORR, HER, OER, CO_2RR, NRR and so on.

5.1. Oxygen reduction reaction

The ORR proceeds through either a 2-electron pathway ($O_2 + 2H^+ + 2e \rightarrow H_2O_2$ in acid) or a 4-electron pathway ($O_2 + 4H^+ + 4e \rightarrow 2H_2O$ in acid). The 4-electron pathway is desired for electricity generation and it is important in several energy-conversion technologies, such as fuel cells and metal-air batteries, while the H_2O_2 generated by the 2-electron pathway is a valuable chemical used in disinfection, pulp bleaching and the oxidation of various chemicals. The electrochemical production of H_2O_2 is a preferred method compared to the traditional anthraquinone redox process as it is environmentally friendly, safe, and easily adopted on a small scale.[130] Therefore, considerable research efforts have been devoted to developing catalysts that can selectively catalyze either 2-electron pathway or 4-electron pathway.

Pt-based materials remain the most active catalysts toward the 4-electron process, but its scarcity and high cost calls for alternatives catalysts based on non-precious transition metals or nanocarbons, among which M-N-C (M = Fe or Co) catalysts with atomic MN_x moieties embedded in graphene represent an attractive alternative.[131] M-N-C catalysts were generally prepared by the pyrolysis method and the optimizations in the synthetic conditions (e.g., precursor combinations, pyrolysis parameters) have resulted in a large number of high-performance ORR catalysts.[53,62,64,65,82,93,131-135] Zitolo et al. synthesized a Fe-N-C catalyst by pyrolyzing Zn(II) zeolitic imidazolate framework, Fe(II) acetate and 1,10-phenanthroline, and the resulted composite were quasi-free of crystallographic Fe structures, as demonstrated by ^{57}Fe Mössbauer spectroscopy and EXAFS-FT analysis.[43] They found that keeping the metal loading sufficiently low and pyrolysis duration short was critical in minimizing the formation of crystalline Fe species. When tested in acidic condition with a rotating ring-disk electrode (RRDE) and in a polymer electrolyte membrane (PEM) fuel cell, the optimized catalysts generated less than 2% H_2O_2 at potentials of interest for PEM, suggesting a 4-electron dominated reduction process. Combined EXAFS and XANES analyses revealed the atomistic structure of Fe to be a porphyrinic planar architecture with a FeN_4C_{12} core integrated in disordered graphene matrix and with O_2 absorbed in the side-on or end-on configuration. Adopting the similar synthetic approach, the same group then synthesized a Co-N-C catalyst free of cobalt particles and it exhibited considerably higher ORR activity in acidic medium than metal-free N-C catalyst, suggesting the atomic Co moieties were the active sites.[44] The selectivity for water formation of the Co-N-C catalyst was found to be lower than the Fe-N-C counterpart. XANES, EXAFS, magnetic susceptibility measurements and DFT analysis were applied to identify the atomistic structure and electronic state of the Co sites in Co-N-C. Interestingly, other than the porphyrinic CoN_4C_{12} moiety as found in Fe-N-C, two defective

cobalt porphyrinic moieties (CoN_3C_{10} and CoN_2C_5) were also suggested as viable candidates in Co-N-C. DFT calculation showed that these cobalt moieties likely bind oxygen intermediates too weakly to allow efficient O_2 reduction. Based on these findings, it was proposed that the modifications of the carbon matrix in Co-N-C with nitrogen or other heteroatoms resulting in a stronger O_2 binding energy at Co centers should improve their ORR activity.

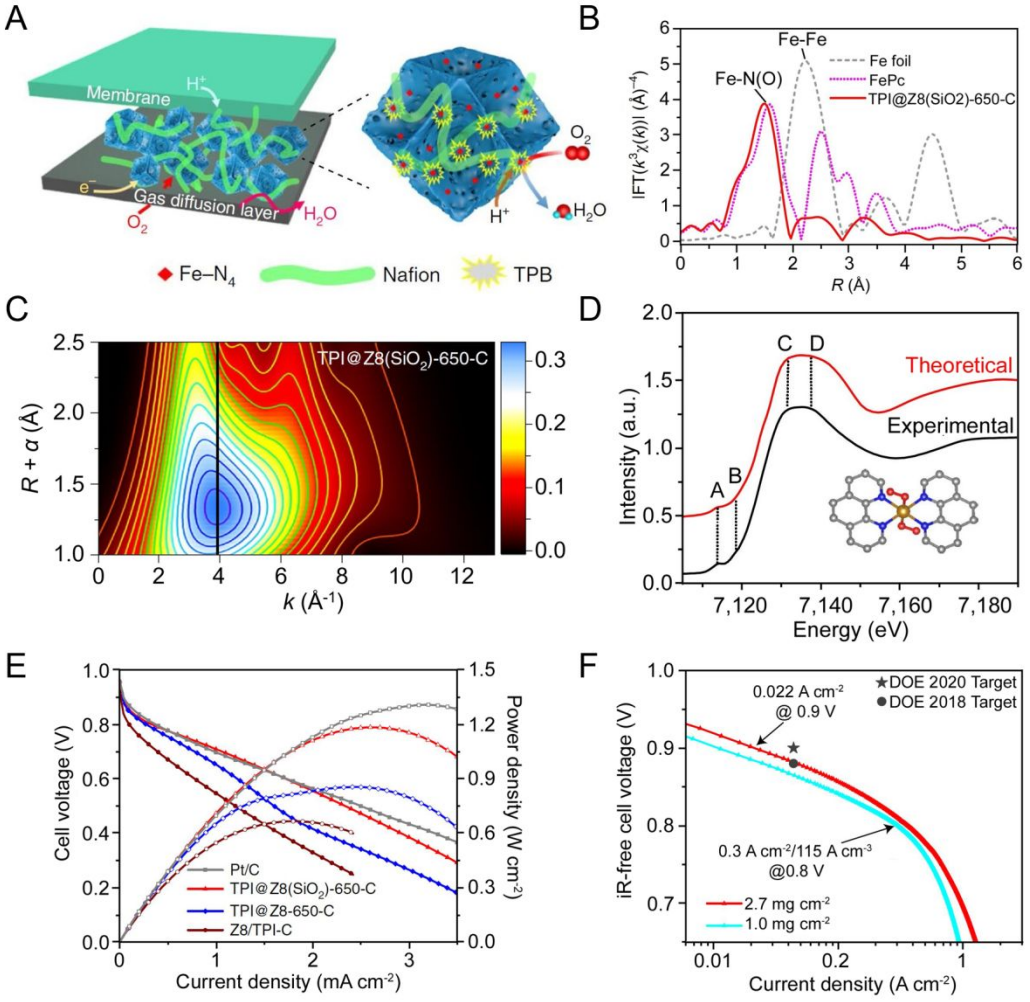

Fig. 15 Fe-N-C electrocatalysts toward ORR with 4-electron pathway. (A) A schematic illustration of active sites at the triple-phase boundary in the concave-shaped Fe-N-C catalyst-based electrodes. (B) k^3-weighted EXAFS-FT with optimum resolutions at 2.0 Å. (C) k^3-weighted EXAFS-WT with optimum resolutions at 2.0 Å of the concave-shaped Fe-N-C catalyst. (D) A comparison between an experimental XANES spectrum and a theoretical spectrum, for which calculations are based on the predicted structure of the FeN_4C_8 moiety with two O_2 molecules adsorbed in end-on mode. (E) Polarization and power density curves of the optimal catalyst and control catalysts at 2.5 bar H_2-O_2. (F) Tafel plot for determination of the activity for the optimal catalyst at 0.9 V_{iR}-free and volumetric activity at 0.8 V_{iR}-free

measured under 1 bar H_2-O_2. Reproduced with permission from Wan et al.[85] Copyright 2019 Nature Publishing Group.

It is important to note that not all single atomic metal sites in M-N-C catalysts can participate in the ORR process as the reaction takes place at the multiple-phase boundary and metal sites that are buried within the carbon matrix remain inactive. To improve the utilization efficiency of active sites, high degree of mesoporosity and macroporosity can be introduced into the M-N-C catalysts. For example, Chung et al. synthesized a porous Fe-N-C catalyst with polyaniline and cyanamide as nitrogen precursors.[51] The cyanamide with low decomposition temperature served to form macropores, which would provide better accessibility to the catalytic sites and a more open framework for improving the ionomer distribution within the catalyst layers. The atomic dispersion of FeN_4 active sites and the coordination between metal and nitrogen atoms were evidenced by HAADF-STEM and EELS but without verification by XAFS analysis. Significantly, the hydrogen (H_2)-air fuel cell fabricated using the Fe-N-C catalysts exhibited comparable performance to a Pt cathode under automotive-application conditions. In another work, Wan et al. fabricated a concave-shaped Fe-N-C catalyst with rich mesoporosity, external surface area and dense Fe-N_4 moieties by pyrolyzing mesoporous SiO_2-coated ZIF-8.[85] The high porosity in this catalyst can afford a large number of active sites at the triple-phase boundary of carbon (e^-), the ionomer (H^+) and O_2 during ORR tests and at the same time facilitate efficient mass transport (Fig. 15A). The EXAFS-FT of the catalyst exhibited a main peak at 1.5 $Å^{-1}$ in *R* space and the EXAFS-WT showed only one intensity maximum at ~ 4.0 $Å^{-1}$ in *k* space that was assigned to Fe-N(O), suggesting the mononuclear Fe centers free of crystalline structures (Fig. 15B,C). The structure of the Fe center was identified as the FeN_4C_8 moiety with two O_2 molecules adsorbed in end-on mode by XANES analysis (Fig. 15D). When tested in a PEM fuel cell under 2.5 bar H_2-O_2, this porous Fe-N-C catalyst exhibited a current density of 560 mA cm^{-2} at 0.8 $V_{iR\text{-}free}$ that is comparable to Pt/C and a peak power density of 1.18 W cm^{-2} at 0.47 V (Fig. 15E). The control sample without additional mesopores displayed inferior activity and its voltage dropped more rapidly at higher current densities when compared to the porous counterpart, suggesting its poor mass transport. When tested under the DOE testing protocol at 1 bar H_2-O_2, the porous Fe-N-C catalyst exhibited a current density of 0.047 A cm^{-2} at 0.88 $V_{iR\text{-}free}$, suppressing the DOE target of 0.044 A cm^{-2} (Fig. 15F).

In addition to Co and Fe single atoms, other transition metal atoms (e.g., Zn, Mn, Cu, Ir, Pt) supported on defective carbon have also been demonstrated as excellent ORR

electrocatalysts with 4-electron pathway that have comparable or even superior performance compared to commercial Pt/C catalysts.[80,91,136-138]

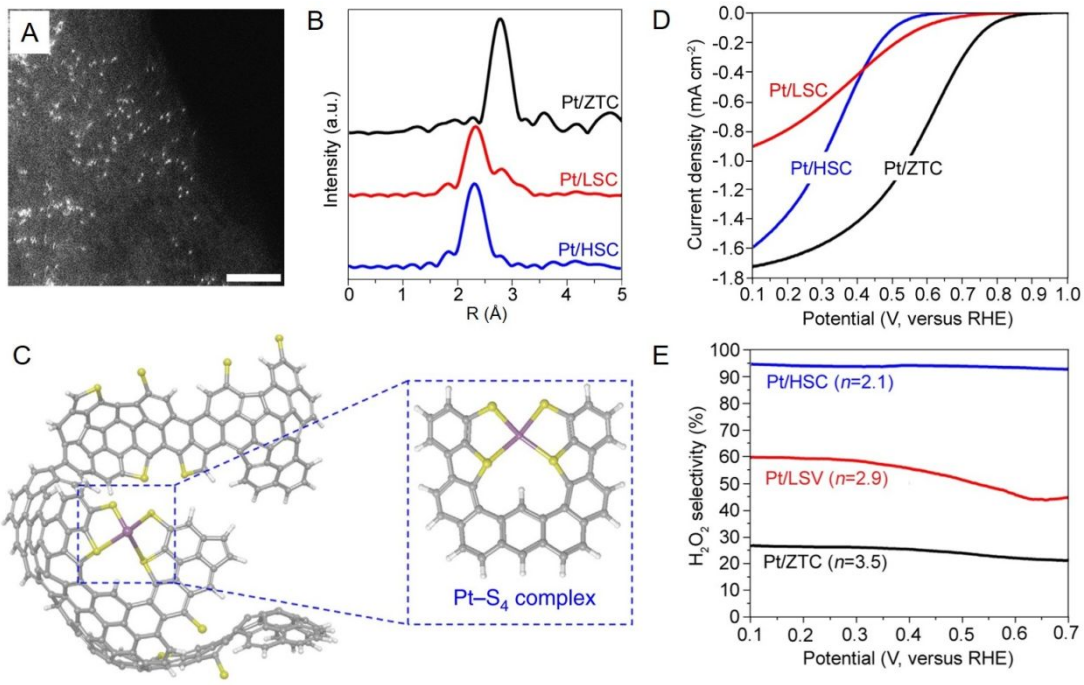

Fig. 16 Structure and ORR activity of Pt/ZTC, Pt/LSC and Pt/HSC catalysts. (A) Atomic resolution HAADF-STEM image of Pt/HSC catalyst. (B) Fourier transforms of k^3-weighted Pt L_{III}-edge EXAFS, confirming that Pt species in Pt/HSC exhibited only Pt-S coordination (CN = 3.8) without significant Pt-Pt coordination and the formation of Pt-Pt bonding in Pt/ZTC and Pt/LSC. (C) Proposed atomistic structure of Pt/HSC with possible thiophene- and thiolate-like functional groups at graphene edge sites, as well as coordinated Pt species. (D) ORR activities of the catalysts measured in an O_2-saturated 0.1 M $HClO_4$ electrolyte with 900 r.p.m. rotation. (E) H_2O_2 production selectivity estimated by RRDE experiments (Pt ring potential: 1.2 V_{RHE}). Reproduced with permission from Choi et al.[130] Copyright 2016 Nature Publishing Group.

The unique electronic properties and isolated atomic sites in SACs can suppress reactions requiring metal ensemble sites and therefore offer opportunities to tune the selectivity. For example, Choi and co-workers achieved selective O_2 reduction toward H_2O_2 production on atomically dispersed Pt catalyst.[130] This catalyst was synthesized via a simple wet-impregnation method with S-doped zeolite-templated carbon composed of 3D graphene nanoribbons as substrate, where the S content can be tuned by adjusting the annealing atmosphere (H_2S/He and pure He) during the post-treatment of the carbon substrate. As revealed by TEM and EXAFS-FT (Fig. 16A,B), Pt (5 wt%) was in highly dispersed atomic

form in the sample with high S content (up to 17 wt%) (HSC), while the formation of Pt clusters was observed in the sample with low S content (4 wt%) (LSC) and non-doped zeolite-templated carbon (ZTC), indicating that the S-moieties can efficiently stabilize the Pt atoms. The active site structure of Pt/HSC was proposed to be Pt atom ligated by two thiophenes and two thiolates based on EXAFS fitting (Fig. 16C), and the oxidation state of Pt was determined to be +2 by XPS and XANES. Electrocatalytic measurements under acidic media showed that the Pt/HSC catalyst predominantly produced H_2O_2 (96% selectivity, n = 2.1) via a 2-electron ORR process, in contrast to Pt/LSC (60% selectivity, n = 2.9) and Pt/ZTC (28% selectivity, n = 3.5) catalysts mediating mixed 2-electron and 4-electron pathways (Fig. 16D,E). DFT calculations implied that the 2-electron pathway is kinetically more favored than the 4-electron pathway on the S-coordinated Pt atoms.

5.2. Hydrogen evolution reaction

Hydrogen (H_2) is the cleanest fuel available and is an attractive substitute for fossil fuels. Electrochemical reduction of water through the hydrogen evolution is a sustainable approach to H_2 and it is promised to replace traditional production method of steam-reformed methane that is energy demanding and environmentally unfriendly.[139] The most effective catalysts for HER is based on precious Pt nanomaterials with low overpotential, small Tafel slope and high exchange current density. Due to the high cost and scarcity of Pt, decreasing the size of Pt nanoparticles to the limit of single atoms is highly desirable to maximize their efficiency by making use of nearly all Pt atoms.[140-142] Cheng et al. fabricated single Pt atom and clusters on nitrogen-doped graphene using the ALD technique and studied their catalytic performance toward HER.[108] During ALD process, the Pt precursor reacted with the nitrogen-doped graphene, where the nitrogen dopants provided strong interaction between the deposited species and the support (Fig. 17A). The resulted catalysts exhibited negligible onset overpotentials with higher activity than the commercial Pt/C catalyst (Fig. 17B). Moreover, when normalized to the Pt loading, the mass activity of the optimized catalyst was 37 times higher than that of the Pt/C catalyst. The enhancement in performance was ascribed to the partially unoccupied density of states in the 5*d* orbital of the Pt atom. However, it is worth noting that there was a co-presence of Pt atoms and clusters in the catalysts, as observed by STEM images, and thus it was difficult to deconvolute the catalytic contributions from each. In another work, Liu et al. suggested that the introduction of curvature into the graphitic carbon can enhance the HER activity of the supported Pt atoms (Fig. 17C).[141] Pt single atoms distributed on nanosized onion-like carbon (Pt_1/OLC) were synthesized by ALD and their

atomic deposition on multishell fullerene structures was characterized by STEM and EXAFS-FT (Fig. 17D,E). Electrochemical studies suggested that the Pt_1/OLC with only 0.27 wt% of Pt exhibited a low overpotential of ~38 mV at 10 mA cm^{-2}, which is comparable to a commercial 20 wt% Pt/C catalyst and superior to a 5 wt% Pt/C catalyst (Fig. 17F). Additionally, Pt atoms supported on two-dimensional graphene (Pt_1/graphene) prepared by the same ALD procedure displayed inferior activity compared to Pt_1/OLC. When normalizing the current by the Pt loadings at the same overpotential of 38 mV, the Pt_1/OLC catalyst exhibited mass activity of 7.4 A mg^{-1}_{Pt} that is ~2.5 times and ~43 times higher than those of the Pt_1/graphene catalyst and the commercial Pt/C catalyst, respectively (Fig. 17G). DFT calculation revealed that the enhanced catalytic activity of Pt_1/OLC could be ascribed to a tip-enhanced local electric field at the Pt site on the curved support and the high local proton concentration near the catalyst surface. This interesting study highlights the critical roles of the local structure and morphology of the substrates in modulating the catalytic performances of the supported metal atoms and provides a new avenue to the rational design of high-performance SACs.

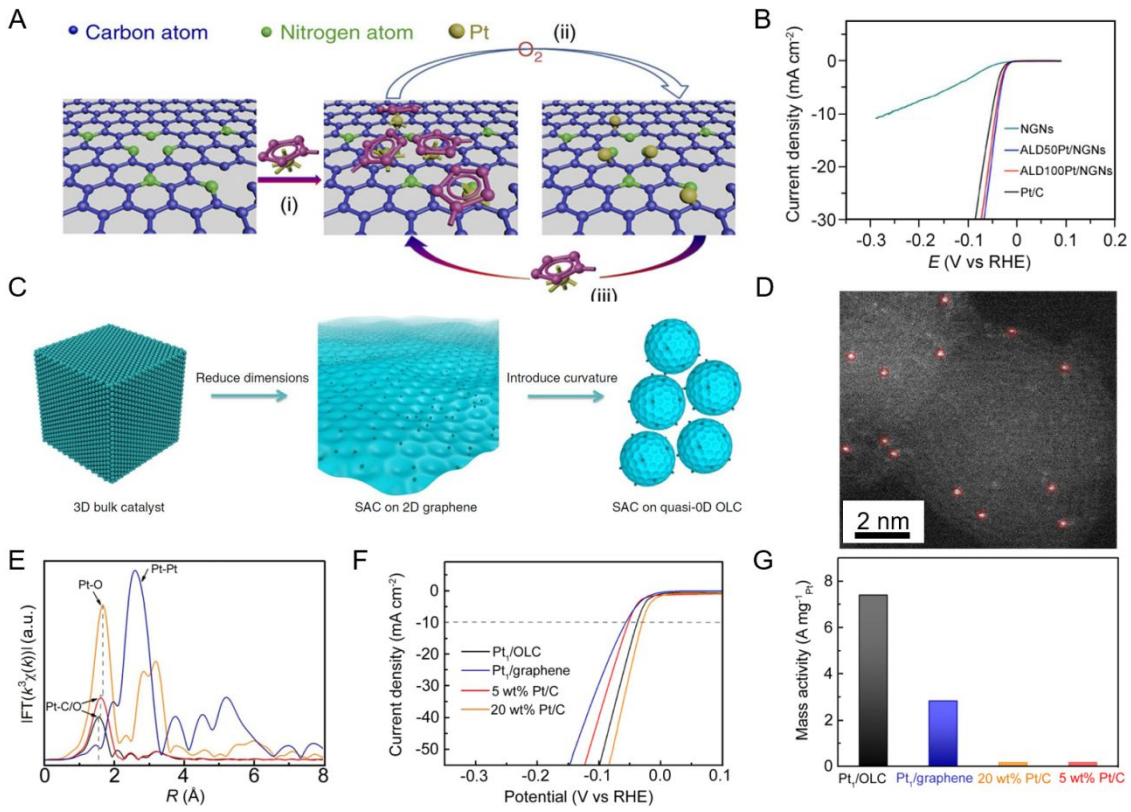

Fig. 17 (A) Schematic illustration of the Pt ALD mechanism on nitrogen-doped graphene nanosheets. (B) HER polarization curves of ALD-derived Pt catalysts. Reproduced with permission from Cheng et al.[108] Copyright 2016 Nature Publishing Group. (C) The schematic illustrates that the catalytically active particles were reduced in size to a single-atom form and

the dimensionality of the catalyst support was reduced by using quasi-0D OLC. (D) The HAADF-STEM image of Pt_1/OLC. (E) The Pt L_3 edge EXAFS-FT spectra of Pt_1/OLC (red) along with several control samples for comparison. (F) Polarization curves of Pt_1/OLC in comparison with Pt_1/graphene and Pt/C in a 0.5 M H_2SO_4. (G) The mass activity of Pt_1/OLC normalized to the Pt loading at an overpotential of 38 mV compared to the reference catalysts. Reproduced with permission from Liu et al.[141] Copyright 2019 Nature Publishing Group.

The desire to eliminate the reliance on the use of Pt has stimulated the search for HER catalysts based on earth-abundant metals, which however usually suffer from the insufficient chemical stability in strong acidic or basic electrolyte. The strong coordination of the metal atoms to the support can greatly enhance their (electro-)chemical stability. By acid etching of a porous Ni foam pre-coated with CVD-grown graphene layers, Qiu et al. fabricated nanoporous graphene-supported Ni atoms along with small amounts of 1-2 nm clusters, as observed by STEM.[143] The resulted catalyst showed superior HER performance with low onset overpotential of ~ 50 mV and cycling stability, which were ascribed to the charge transfer between the Ni atoms and the neighboring C atoms. Yao and co-workers prepared well-dispersed atomic Ni (1.5 wt%) in graphitized carbon matrix by carbonization of a Ni-based MOF in inert atmosphere followed by electrochemical activation.[144] Examination of different regions by STEM suggested that about 78% of the Ni species were present as well-separated single atoms with the rest as nanoclusters. This catalyst exhibited overpotentials of 34 mV, 48 mV, 112 mV at the current density of 10 mA cm^{-2}, 20 mA cm^{-2} and 100 mA cm^{-2}, respectively, a low Tafel slope of 41 mV dec^{-1}, and stable operation for over 25 h in chronoamperometric test. The same group later synthesized another HER catalyst of atomically dispersed Ni on defective graphene (A-Ni@DG, 1.24 wt% Ni) by annealing the mixture of Ni^{2+} precursor and defective graphene, followed by acid-leaching to remove the redundant Ni-derived nanoparticles (Fig. 18A).[145] The A-Ni@DG catalyst displayed a fragmentized and porous 2D structure without any obvious nanoparticles and the Ni atoms were uniformly distributed on the graphene layers (Fig. 18B). The Ni atom was suggested to occupy the di-vacancy of the graphene lattices, as revealed by HAADF-STEM image (Fig. 18C). The Ni species were predominantly present as atomically dispersed Ni, as evidenced by the absence of appreciable Ni-Ni peak in the EXAFS-FT spectra. The HER activity of A-Ni@DG, with overpotential at 10 mA cm^{-2} as low as 70 mV and Tafel slope of 31 mV dec^{-1} in 0.5 M H_2SO_4, was highly comparable to that of the commercial Pt/C catalyst (Fig. 18D).

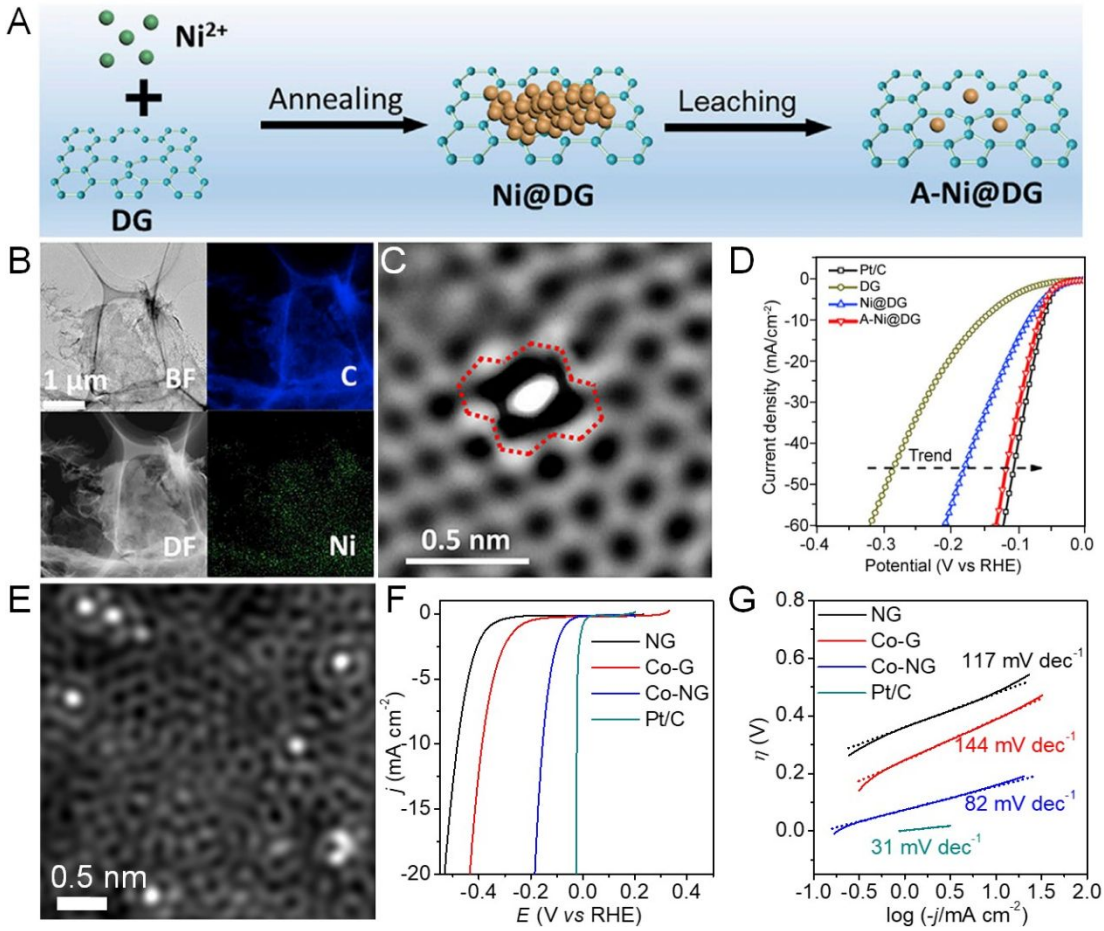

Fig. 18 Representative examples of HER catalysts based on graphene-supported atomic Ni and Co catalysts. (A) The fabrication schematic of Ni atoms on defective graphene. (B-C) STEM-EDS elemental mapping (B) and HAADF-STEM image (C) of the atomic Ni catalyst. (D) HER polarization curves of the atomic Ni catalysts along with other control samples. Reproduced with permission from Zhang et al.[145] Copyright 2018 Elsevier. (E) HAADF-STEM image of the single Co atoms on nitrogen-doped graphene in the Co-NG catalyst. (F) HER polarization curves of the Co-NG catalyst along with control samples. (G) Tafel plots of the Co-NG catalyst and control samples. Reproduced with permission from Fei et al.[72] Copyright 2015 Nature Publishing Group.

In addition to Ni, another first-row transition metal Co has also been atomically dispersed in graphene and repeatedly explored as HER electrocatalysts. Fei et al. achieved atomic Co (0.57 at%) embedded in nitrogen-doped graphene (Co-NG) that is active and stable in both acidic and alkaline conditions.[72] The catalyst was synthesized by thermally annealing GO and Co precursor in NH_3 atmosphere. The Co metals were atomically dispersed in the graphene substrate (Fig. 18E), and further confirmed by EXAFS-FT and EXAFS-WT analyses. The co-existence of Co and N in the catalysts was found to be critical in achieving

the high HER activity (Fig. 18F), indicating the active sites were associated with the Co and N. Impressively, the onset overpotential of Co-NG in acid was as low as 30 mV and the overpotential required to deliver 10 mA cm^{-2} was 147 mV. The Tafel slope of Co-NG was determined to be 82 mV dec^{-1} (Fig. 18G). Other than GO, molecular and polymeric precursors have been used to prepare atomic Co catalysts toward HER via the pyrolysis strategy.[146-148] Liang et al. obtained a CoN_x/C catalyst by pyrolyzing Co-N_4 macrocycles or cobalt/*o*-phenylenediamine composites with silica colloids as hard templates.[147] This catalyst, with only 0.14 wt% Co, exhibited low overpotential of 133 mV at 10 mA cm^{-2}, high turnover frequencies and high stability. Though XAFS characterizations were not provided in this study, high-resolution TEM and XPS analyses, along with the acid leaching and thiocyanate ion poisoning experiments, suggested that the catalytic activity originated from the atomically dispersed CoN_x centers. Wang et al. synthesized self-supported and porous carbon fiber foams embedded with CoN_x complex by pyrolyzing Co^{2+}-absorbed polyaniline precursor.[146] The annealing temperature and the porous structure were suggested to play critical roles in the formation and activity of the atomic Co sites. XAFS analyses suggested that annealing below 850 °C resulted in the predominant formation of atomic Co, while metal nanoparticles would form when annealed at 950 °C. The optimal catalyst annealed at 750 °C with 0.22 at% Co showed excellent HER activity (138 mV at 10 mA cm^{-2}; 212 mV at 100 mA cm^{-2}) and long-term stability. Besides, single Mo and W atoms supported on nitrogen-doped graphene layers have recently been demonstrated as highly efficient HER catalysts.[149-151] Table 1 summarizes different HER catalysts based on single metal atoms supported on graphene layers or graphitized carbons.

5.3. Oxygen evolution reaction

OER is an important process in several energy-conversion technologies, such as water electrolyzers, metal-air batteries and CO_2 conversion. The intrinsically sluggish kinetics of the OER, which involves multiple proton-coupled electron-transfer steps, have stimulated the exploration for highly active and stable electrocatalysts.[5,57] Precious-metal-based electrocatalysts (Ru and Ir) possess high activity, but their high cost and scarcity have hindered their large-scale practical application. As alternative catalysts based on earth-abundant elements, Fe-, Co- and Ni-based oxides and derivatives have been intensively studied,[152] and their atomic counterparts supported on graphene have recently been demonstrated as efficient OER catalysts (Table 1). For example, the A-Ni@DG catalyst discussed in the HER section was also highly active toward OER with a small overpotential of

270 mV to deliver 10 mA cm^{-2} and Tafel slope of 47 mV dec^{-1} in 1 M KOH.[145] Chen et al. developed an OER catalyst composed of atomic Fe-N species (verified by HAADF-STEM and EXAFS-FT) on N and S co-doped hierarchical carbon layers, prepared by pyrolysis of CNTs coated with 2,2-bipyridine and Fe precursor.[57] The resulted catalyst exhibited an overpotential of 370 mV at a current density of 10 mA cm^{-2} and a Tafel slope of 82 mV dec^{-1} in 0.1 M KOH solution. Guo et al. reported boron-doped Co-N-C active sites dispersed in porous carbon sheets by a soft template self-assembly pyrolysis method.[47] The atomically dispersed boron-doped Co-N-C sites were evidenced by HAADF-STEM, XPS, XANES and EXAFS characterizations. The catalyst required 430 mV to deliver 10 mA cm^{-2} in 0.1 M KOH. DFT calculations suggested that the introduction of boron gives an electron-deficient site that can strengthen the interaction with oxygenated species, facilitating the reaction kinetics. Hou et al. reported S- and N-coordinated Ni atoms dispersed in porous carbon nanosheets as a highly active and stable OER catalyst with a low overpotential of 1.51 V at a current density of 10 mA cm^{-2} and a Tafel slope of 45 mV dec^{-1} in alkaline media, making it superior to the benchmark Ir/C catalysts.[48] XANES and EXAFS studies revealed that the Ni atom adopted a distorted Ni-$[N/S]_4$ bonding configuration deviated from the ideal square planar geometry and the coordination numbers of Ni-N and Ni-S were estimated by EXAFS fitting results to be 2.8(2)and 0.8(3), respectively. Theoretical studies based on such coordination environment suggested that the high catalytic activity of the S- and N-coordinated Ni atoms resulted from the optimized density-of-states distribution and enhanced electron transfer ability of the active sites. Our group recently reported a series of atomic transition metals (Fe, Co, Ni) in nitrogen-doped graphene by pyrolyzing GO and metal precursor in NH_3 atmosphere and investigated the influence of the metal center in determining the OER activity.[25] The uniform distribution of the metal atoms in the graphene matrix was evidenced by HAADF-STEM (Fig. 19A) and EXAFS-FT/WT (Fig. 12B,C). DFT calculation results suggested that the OER activity and reaction pathways were strongly dependent on the number of *d* electrons (N_d) of the metal with Fe (N_d = 6) and Co (N_d = 7) following the single-site mechanism and Ni (N_d = 8) following the dual-site mechanism (Fig. 19B). Electrochemical measurements in 1 M KOH electrolyte confirmed the metal-dependent OER activity in different atomic catalysts following the trend Ni > Co > Fe. Specifically, the atomic Ni catalyst exhibited an onset potential of 1.43 V and an overpotential at 10 mA cm^{-2} of 331 mV, much smaller than those of atomic Co (402 mV) and atomic Fe (488 mV) (Fig. 19C). The Tafel slope for atomic Ni was determined to be 63 mV dec^{-1}, smaller than those of atomic Co (80 mV dec^{-1}), atomic Fe (164 mV dec^{-1}) and metal-free catalysts (175 mV dec^{-1}) (Fig. 19D). Stability tests by both

electrochemical measurements and structural characterization of XAFS suggested that the metal atom and its coordinating matrix were robust enough to withstand the OER operation condition. Atomic Mn in nitrogen-doped graphene has recently been demonstrated to exhibit superior OER activity with intrinsic activity close to that of nature's catalyst $CaMn_4O_5$ in photosystem II and much higher than those of previously reported Mn-based OER catalysts.[74]

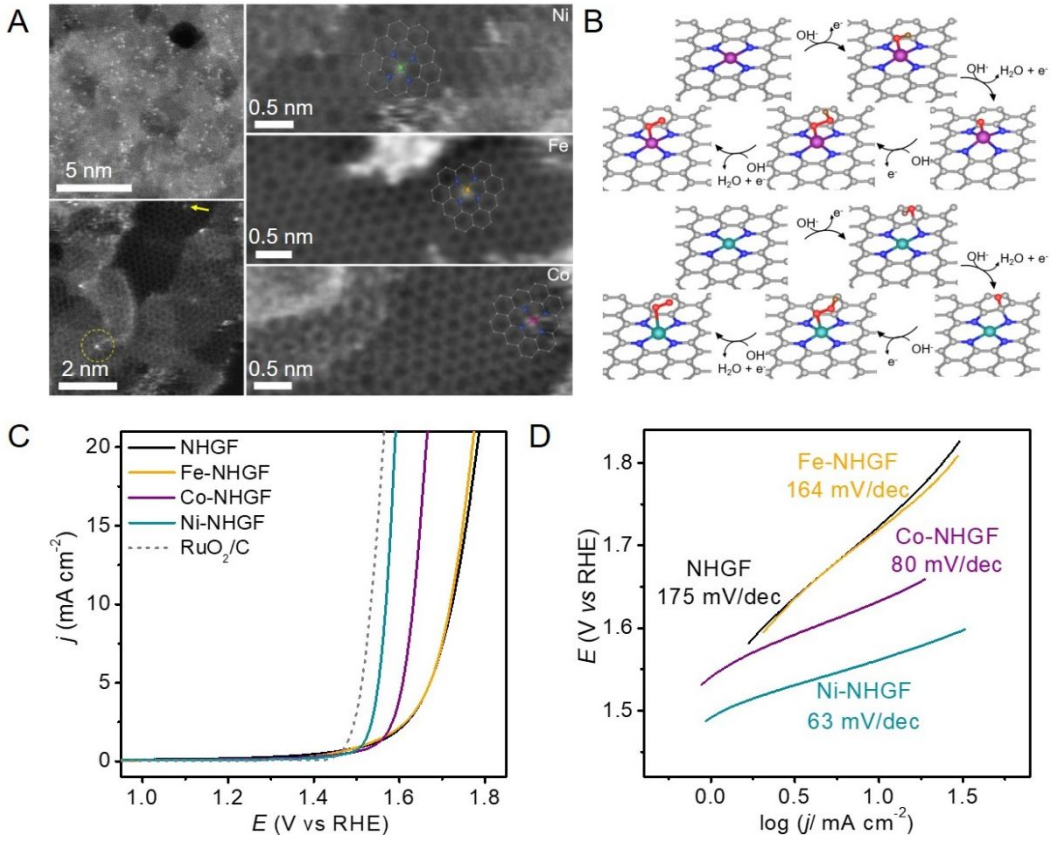

Fig. 19 Structural and electrocatalytic characterizations of atomic metal catalysts toward OER. (A) Atomic structure characterizations of Ni, Fe, Co single atoms supported on nitrogen-graphene by HAADF-STEM. (B) Proposed reaction scheme with the intermediates having optimized geometry of the single-site (top) and dual-site mechanisms (bottom) toward OER. (C) OER polarization curves of different atomic catalysts along with control samples. (D) Tafel plots for different atomic metal catalysts and metal-free nitrogen-doped graphene. Reproduced with permission from Fei et al.[25] Copyright 2018 Nature Publishing Group.

5.4. CO_2 reduction reaction

Electrochemical reduction of CO_2 to value-added molecules such as carbon monoxide (CO) and hydrocarbons is an effective strategy to remit the environmental and energy issues. However, significant overpotentials are typically needed to overcome the activation barrier of CO_2 reduction due to its sluggish kinetics; moreover, there are wide distributions of products

(e.g., CO, HCHO, CH_3OH, CH_4) and competitive side reactions such as HER.[153] Therefore, developing highly active, selective and stable electrocatalysts is of paramount significance to realize CO_2RR for practical applications. Many types of materials, including metals, metal oxides, carbon-based materials, and molecular compounds, have been shown to be effective CO_2RR electrocatalysts and their performances have been greatly enhanced by optimizing the size, structure, and composition.[154-156]

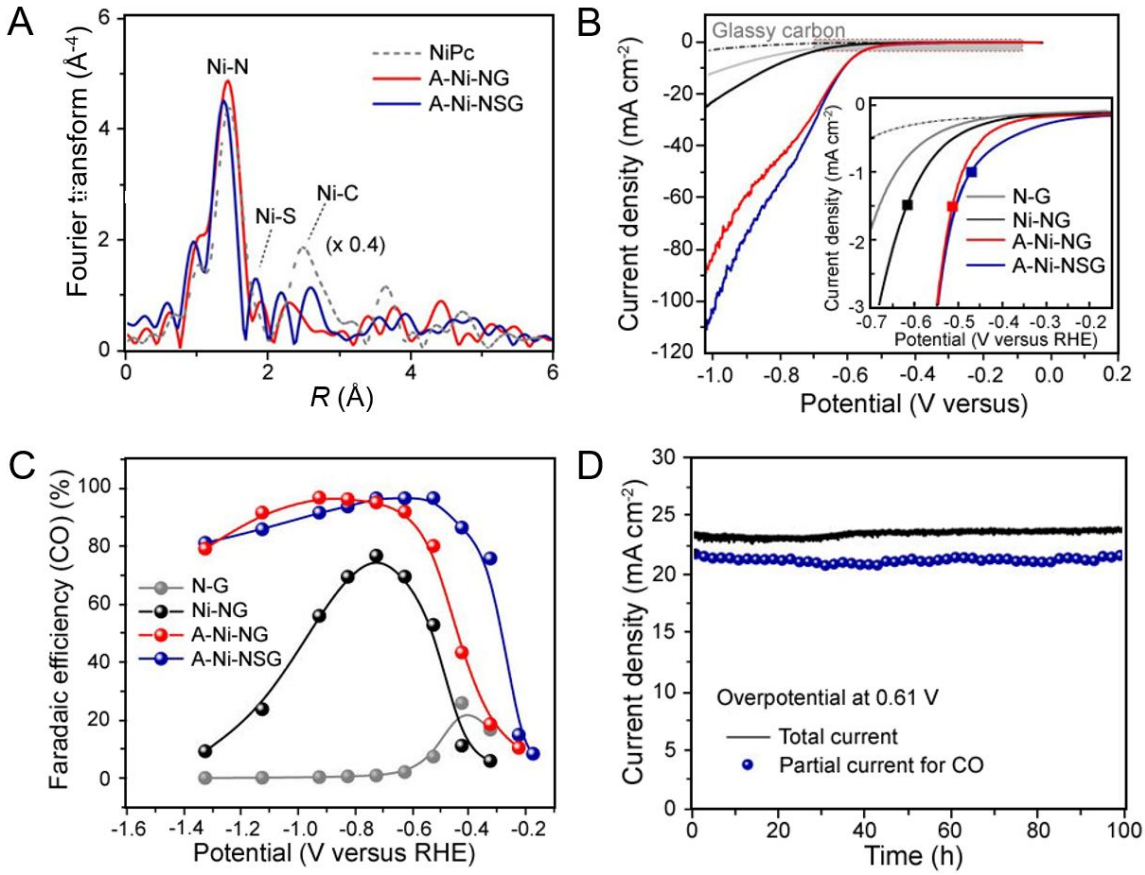

Fig. 20 Structural and CO_2RR catalytic characterizations of the atomic Ni catalyst supported on N- and S-codoped graphene. (A) FT-EXAFS spectra of the atomic Ni catalyst along with reference samples. (B) Polarization curves in CO_2-saturated 0.5 M $KHCO_3$ solution. (C) CO Faradaic efficiency at various applied potentials. (D) Current-time response at constant potential. Reproduced with permission from Yang et al.[46] Copyright 2018 Nature Publishing Group.

Recently, first-row transition metals (e.g., Zn, Mn, Fe, Co, Ni, Cu, Sn) atomically dispersed in graphene layers have been explored as CO_2RR electrocatalysts in aqueous solution with CO as the dominant product and Ni-based ones are the most widely studied among different atomic metal catalysts (Table 2).[46,73,99,157-172] For example, using the pyrolysis

method with Ni-pentaethylenehexamine and GO as precursors, Su et al. prepared atomic Ni embedded in nitrogen-doped graphene that exhibited a high activity for CO formation in neutral solution with Faradaic efficiency exceeding 90% at -0.7 V to -0.9 V.[157] The competitive HER was greatly suppressed, in strong contrast to the metal-free nitrogen-doped graphene and Ni metal electrode. The NiN_x moiety was proposed to be the active center based on the EXAFS-FT analysis as well as on the observation that the replacement of the Ni by Cu resulted in significantly lower CO_2RR activity and that the Faradaic efficiency of CO did not decrease after lowering the concentration of the NiN_x moiety. With the similar synthetic strategy, Jiang et al. reported another atomic Ni catalyst that presented a high CO selectivity of 95% at an overpotential of 0.55 V and long-term stability over 20 hours' continuous electrolysis in 0.5 M $KHCO_3$.[73] The atomic dispersion of Ni and a mixed Ni-C/Ni-N coordination environment within the catalyst were suggested by XANES and EXAFS analyses. The active sites were proposed to be associated with the NiN_x moiety by the control experiments on Ni-coordinated graphene with no nitrogen incorporation, nitrogen-doped graphene and Ni_3N catalysts, all exhibiting significantly lower CO_2RR activity and CO_2-to-CO selectivity. The critical role of the Ni atoms in forming the active centers was confirmed by the catalytic evaluation on a variety of other atomic transition metals (e.g., Fe, Co, Mn, Cu) synthesized by the same approach, which showed dramatically decreased selectivity. The use of GO as pyrolysis precursor to prepare CO_2RR-active atomic catalysts was recently extended to Fe-N-C catalyst by Tour and coworkers.[173] They found that the CO_2RR activity of Fe-N-C was highly dependent on the pyrolysis temperature and the sample prepared at 750 °C had predominant atomic Fe dispersion (evidenced by EXAFS-FT) that resulted in the optimal activity of a maximum Faradaic efficiency of 80% toward CO formation at -0.6 V. Moreover, the formation of Fe_3O_4 and metallic Fe nanoparticles resulted from the increase in the Fe loading would lead to lower selectivity (<10%) toward CO production, consistent with the study by Huan et al.[174]

In addition to GO, MOF and molecular/polymeric precursors have also been frequently applied in the pyrolysis method for the preparation of M-N-C catalysts toward CO_2RR.[46,158-161,175] With handful choices of molecular precursors for the pyrolysis synthesis of G-SACs, multiple dopants can be simultaneously introduced in the carbon substrate to tune the electronic structure of the metal center and thus the CO_2RR activity. Yang et al. prepared atomically dispersed Ni on nitrogen-doped graphene (A-Ni-NG) and sulfur-, nitrogen-codoped graphene (A-Ni-NSG) by pyrolyzing a mixture of amino acid (L-alanine or L-cysteine), melamine and Ni acetate.[46] The resulted composite possessed a two-dimensional

structure, and the Ni existed as isolated atoms on the graphene substrate with no Ni-Ni bonding, confirmed by the HAADF-STEM image and FT-EXAFS spectra (Fig. 20A). When tested as CO_2RR catalysts (Fig. 20B), A-Ni-NSG showed an earlier onset potential than A-Ni-NG and both of them delivered considerably higher current density than control samples of nitrogen-doped graphene (NG) and Ni nanoparticle decorated NG (Ni-NG). The enhancement from sulfur doping was attributed to the distorted coordination geometry around Ni center in A-Ni-NSG owing to the non-centrosymmetric ligand strength, which was expected to promote better adsorption of reactants and intermediates on the catalyst surface. The two single Ni atom catalysts maintain over 80% selectivity toward CO production, even at very negative applied potentials (Fig. 20C). Moreover, the A-Ni-NSG catalyst could deliver stable performance, retaining 98% of the initial current after 100 hours operation (Fig. 20D). The active site was identified as monovalent Ni atomic center with a d^9 electronic configuration based on operando X-ray absorption and photoelectron spectroscopy measurement.

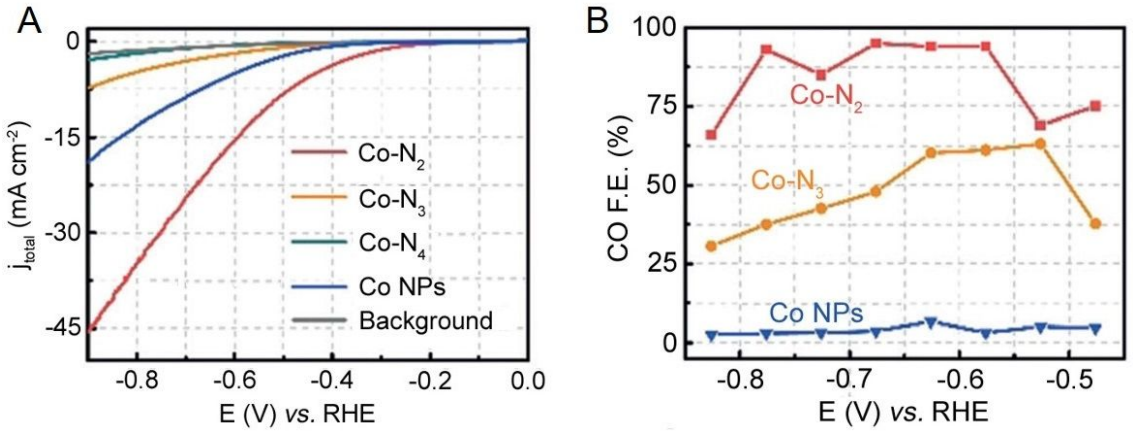

Fig. 21 CO_2RR activity and selectivity of Co-N_2, Co-N_3, Co-N_4 and Co NPs. (A) Linear sweep voltammetry of the different catalysts evaluated in 0.5 M $KHCO_3$ with pure carbon paper as background. (B) CO Faradaic efficiencies at different applied potentials of the different catalysts. Reproduced with permission from Wang et al.[45] Copyright 2018 Wiley-VCH.

Though Co-N-C catalysts with atomic CoN_x moieties were most frequently investigated as HER electrocatalysts and studies focusing on elucidating the correlation between the type of metal center and CO_2RR activity of M-N-C catalysts have suggested that Co-N-C catalysts generally exhibit low Faradaic efficiency for CO formation compared to Ni-based and Fe-based counterparts,[176] it was indicated by recent reports that their selectivity toward CO formation and H_2 generation can be tuned by altering the coordination

environment of the Co center.[45,163,177,178] For example, Wang et al. synthesized a series of atomic Co catalysts by pyrolyzing Co/Zn MOFs and the nitrogen coordination numbers of the Co center was regulated by the variation in pyrolysis temperature. Specifically, the increase in pyrolysis temperature would lead to the decrease in N coordinators due to the volatile nature of C-N fragments, generating three different types of CoN_x moieties (i.e., Co-N_2, Co-N_3 and Co-N_4), as determined by EXAFS fitting (Fig. 4C). As shown by the linear sweep voltammetry (Fig. 21A), the overall current density was highest in Co-N_2 and it reached 18.1 mA cm^{-2} at -0.63 V, which was significantly higher than those for Co-N_3, Co-N_4 and Co nanoparticles. Analysis of products distribution by gas chromatography and ^1H nuclear magnetic resonance confirmed that CO and H_2 were the main products with no other gas products or liquid products detected for all catalysts studied. The CO Faradaic efficiency for Co-N_2 reached up to 95% at -0.68 V, higher than the maximum value for Co-N_3 (63% at -0.53 V), Co-N_4 (below 5% at -0.83 V to -1.03 V) and Co nanoparticles (below 7% across all applied potentials) (Fig. 21B). Experimental and DFT calculations suggested that the high performance of the Co-N_2 catalyst could be ascribed to its low coordination number that facilitated the activation of CO_2 to the $CO_2^{\bullet -}$ intermediate.

5.5. N_2 reduction reaction

NH_3 is one of the most highly produced chemicals that is widely used in agriculture and industry applications.[179] Currently, NH_3 is primarily synthesized by the Haber-Bosch process with heterogeneous Fe-based catalysts at high temperature and pressure, accounting for ~ 1.5% of global energy consumption and generating 300 million metric tons of fossil fuel-derived CO_2 annually.[180] The electrochemical reduction of N_2, ideally under ambient conditions with H_2O as hydrogen source, has been proposed as a sustainable alternative for NH_3 synthesis.[181] However, the development of the electrochemical approach has been impeded by the lack of efficient electrocatalysts with high activity and selectivity over hydrogen generation. Thanks to the recent research efforts, some electrocatalysts for N_2 reduction have been developed, including noble metals, nonprecious metal-based materials, and nanocarbons.[180-182] Recently, Geng et al. reported that Ru single atoms (0.18 wt%) on nitrogen-doped carbon (denoted as Ru SAs/N-C) can work as efficient electrocatalyst toward electrochemical N_2 reduction.[183] The catalyst was synthesized by pyrolyzing Ru-containing derivative of zeolitic imidazolate frameworks (Fig. 22A). XANES and EXAFS studies suggested that the Ru was atomically dispersed in the carbon matrix with coordination to N atoms and the valence state of Ru species was ≈+3. The electrochemical measurements were

performed in three-electrode system with two-compartment cell in 0.05 M H_2SO_4. The partial current for NH_3 production (determined by the indophenol blue method) of Ru SAs/N-C was significantly higher than that of the control sample Ru NPs/N-C at all applied potentials (Fig. 22B). At -0.2 V versus RHE, Ru SAs/N-C achieved a Faradaic efficiency of 29.6% for NH_3 production, which was about 2-fold higher than that of Ru NPs/N-C (Fig. 22C). When normalized by the weight of catalysts, Ru SAs/N-C exhibited the yield rate of 120.9 μg_{NH_3} mg^{-1} h^{-1} at -0.2 V (Fig. 22D). It should be cautioned that without an elaborated calibration and control, the accurate quantification of the NH_3 production could be plagued by possible contamination in laboratory environment, purging gases, electrolyte solvents or the catalysts N_2, electrolytes or the catalysts. To this end, the authors conducted a series of control and confirmatory experiments, including open circuit control measurements, argon control measurements and $^{15}N_2$ reduction experiments to verify that the NH_3 production over Ru SAs/N-C is indeed originated from N_2 electrochemical reduction. Electrochemical stability testes revealed that Ru SAs/N-C experienced less than 7% decay of yield rate for NH_3 reduction during a 12 h potentiostatic test at -0.2 V (Fig. 22E). In another work, Mo single metals (evidenced by EXAFS-FT) supported on N-doped carbons were reported as efficient and stable electrocatalysts toward N_2 reduction with high NH_3 production yield and Faradaic efficiency.[184]

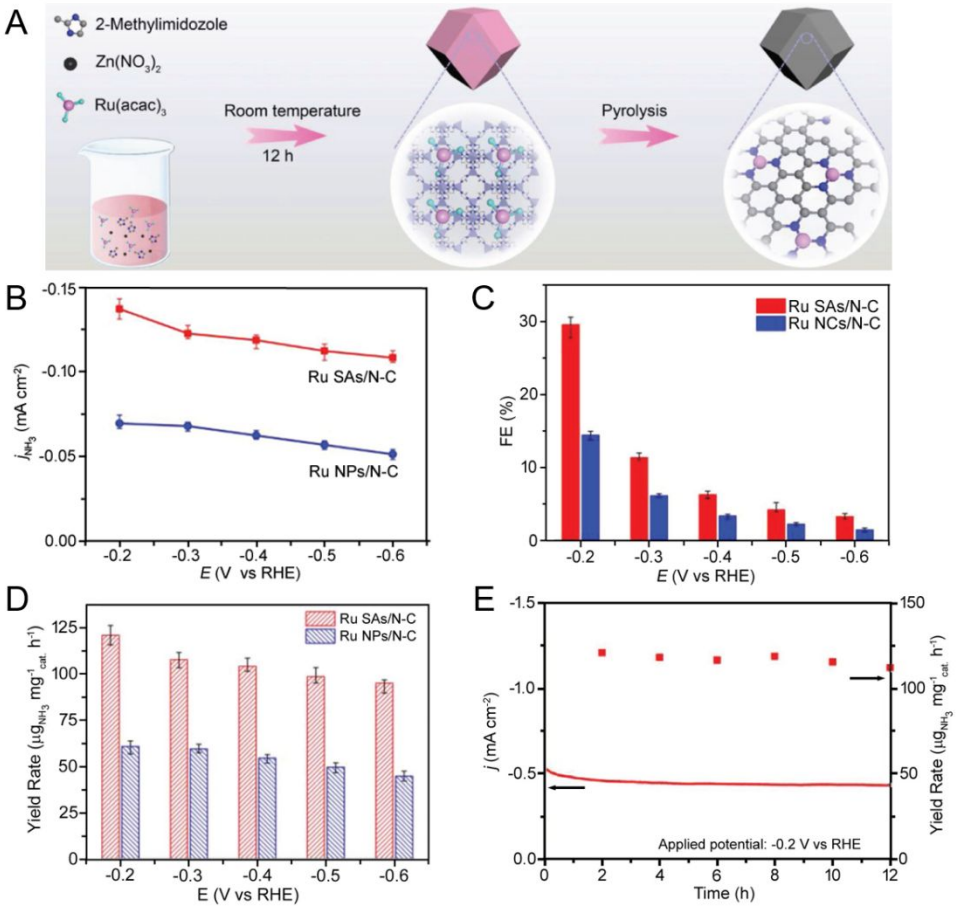

Fig. 22 Synthetic route and NRR electrocatalytic characterizations of Ru SAs/N-C. (A) Scheme of the synthetic procedure for Ru SAs/N-C. (B) Current densities for NH_3 production of Ru SAs/N-C and Ru NPs/N-C. (C) Faradaic efficiency and (D) yield rate of NH_3 production at different applied potentials on Ru SAs/N-C and Ru NPs/N-C. (E) 12 h durability test for Ru SAs/N-C toward N_2 electrochemical reduction at -0.2 V versus RHE. Reproduced with permission from Geng et al.[183] Copyright 2018 Wiley-VCH.

5.6. Other electrochemical reactions

Bao and co-workers reported the use of G-SACs as alternative counter electrode to Pt electrode for dye-sensitized solar cells (DSSCs).[104] A series of single atomic metals (Mn, Fe, Co, Ni and Cu) in the form of MN_4 moieties confined in the basal plane of graphene were synthesized by ball milling of a metal phthalocyanine and graphene nanosheets, and the atomic dispersion of the metals were confirmed by HAADF-STEM and EXAFS-FT. Among the different metals, CoN_4 can work as highly active and stable catalysts facilitating the interconversion of the redox couple I^-/I_3^-. Further, a solar cell device utilizing the CoN_4 as counter electrode was fabricated and displayed a higher power conversion efficiency than the

Pt counterpart. DFT calculations suggested that the resulting superior catalytic properties of CoN_4 could be ascribed to the desired adsorption energy of iodine on the single Co sites.

Sun and co-workers employed the ALD technique to synthesize single atoms and sub-nanometer clusters of Pt on the surfaces of defective graphene nanosheet and studied their catalytic behaviors toward methanol oxidation reaction (MOR), which represents the key reaction of the direct methanol fuel cell technology.[106] The morphology, size, density and loading of Pt on graphene could be well regulated by tuning the number of ALD cycles, which allowed the investigation in the effects of different Pt species on catalytic properties. Catalytic measurements revealed that these catalysts had much higher activity for methanol oxidation and superior tolerance than commercial Pt/C and the excellent catalytic performance was attributed to the low-coordination and partially unoccupied densities of states of Pt atoms 5*d* orbital.

6. Conclusion and outlook

The development of efficient and cost-effective catalysts is of great interest and importance for clean energy applications. Benefited from the unique physicochemical properties of graphene substrate, G-SACs represent a unique class of single atom catalysts compared to those supported on metal oxide-based substrates for catalyzing electrochemical energy conversion processes including hydrogen evolution, oxygen reduction, oxygen evolution, CO_2 reduction, N_2 reduction and methanol oxidation. These G-SACs have been prepared by a variety of strategies including electron/ion irradiation, atomic layer deposition, ball milling, photochemical reduction, solution-phase synthesis, pyrolysis using different types of precursors including molecules, polymers, MOFs and GO. In addition, considerable research efforts have been devoted to establishing the correlation between structure and catalytic properties in G-SACs by applying the concept of ligand-field effects adapted from coordination chemistry since single atoms embedded in graphene can be considered as the mimics of organometallic complexes with the metal center and neighboring coordinators accommodated in the π-conjugated carbon matrix. This aspect has been demonstrated by several experimental and theoretical studies where the regulations in the identity of the metal center and coordinators, coordination configuration, the electronic structure of the carbon substrate and the location of the active site have resulted in the effective tuning of the catalytic behaviors in G-SACs. The foundation for the establishment of the structure-to-activity linkage in G-SACs lies in the identification of the active site structure. Among the various characterization techniques, XAS analyses comprising EXAFS and XANES are

powerful tools for determining the geometric and electronic structure of the active sites, such as the oxidation state of the metal center, bond length, bond disorder, coordination number and geometry. Despite the excitement and achievements brought by the research on G-SACs for electrochemical energy conversion to date, considerable challenges and opportunities remain from both fundamental and applied research perspectives.

From the outset, the achievement of high metal loading in G-SACs with exclusive single atomic dispersion remains a most critical challenge for the field. The formation of strong interaction between the metal center and the neighboring coordinators typically involve the processes of bond breaking and reforming, which require the input of high energy during catalysts preparation (e.g., pyrolysis or ball milling). These activation processes could simultaneously cause the metal atoms to diffuse and agglomerate due to their large surface free energy and therefore the amounts of metals added during preparation need to be sufficiently low to avoid aggregation. Thus far, the metal contents in most studies are typically below 5 wt%, which greatly limits the number of active sites and performance of G-SACs to meet practical applications. Besides the nominal metal loading, another important consideration is that the single metal atoms should be preferentially exposed at the surface so as to actively participate in catalytic reaction. To increase the metal loading of G-SACs, defects engineering of graphene could potentially be explored to introduce additional doping sites for both metal atoms and heteroatoms. Alternatively, modification of existing synthetic strategies and development of novel methods that can minimize the exposure of precursor materials to high-energy environment could minimize aggregation while increasing atomic metal loading.

Second, despite some pioneering attempts, it remains difficult to correlate the exact structure configuration with the catalytic properties, which further precludes the establishment of design principles in optimizing the intrinsic activity of G-SACs. The reasons behind this difficulty are multifold. Firstly, the heterogeneous structure with co-presence of atomic sites and metal aggregates, and the nonuniform distribution of different types of atomic sites severely complicate the identification of active sites as well as the origin of catalytic activity. Secondly, there is a lack of efficient synthetic methods that can systematically modulate the metal center and its coordination environment in a tunable and predictable manner. For most methods developed for synthesizing G-SACs to date, any given method can usually only generate one or a few specified structures and it remains unclear how the adopted structures are correlated with the synthetic conditions. In addition, most studies of G-SACs have focused on atomic MN_x moieties, while other heteroatoms (e.g., B, O, S) are less investigated either as

coordinators to the metal center or as dopants in the carbon matrix. The incorporation of these multiple dopants could provide new avenues to tune the electronic structure and therefore the intrinsic activity of the metal center. Additionally, the comparison in the intrinsic activity among different types of atomic sites prepared by different methods is not straightforward considering that several structural characteristics (e.g., electrical conductivity, porosity, surface area and wettability) beyond the active site structure can influence the catalytic activity of G-SACs and are highly sensitive to the synthetic routes. Therefore, the development of a universal method to synthesize G-SACs with monodispersed and systematically tailorable active sites are highly desirable for unraveling the fundamental correlation between local atomic structures and the catalytic properties.

Lastly, there is little experimental insight on the metal-reactant and metal-support interactions in G-SACs under electrocatalytic conditions, and a limited understanding of the mechanistic details of the reactions on the catalyst surface. As large differences could exist in the geometric and electronic structure of the active metal during electrochemical reaction from that derived under *ex situ* condition, *in situ*/*operando* studies will play important roles in properly unveiling the real active site and the dynamic process for various catalytic processes. The precise understanding of the reaction mechanism is pivotal for the rational design of next generation of high-performing G-SACs for practical technological applications. Despite many challenges ahead, we have witnessed enormous increase of research efforts in the relevant areas in the past few years. The continued efforts in synthetic design and structural/mechanistic studies will surely help accelerate the development of G-SACs with high activity, selectivity and stability for the applications in wide ranges of electrochemical reaction as well as other types of catalytic processes.

Acknowledgements X.D. acknowledges the support by National Science Foundation Grant No. 1800580. Y.H. acknowledges support from Office of Naval Research grant N000141812155. J.D. acknowledges support from the National Natural Science Foundation of China (Grant No. 11605225) and Youth Innovation Promotion Association CAS.

References

[1] V. R. Stamenkovic, D. Strmcnik, P. P. Lopes, N. M. Markovic, *Nat. Mater.*, 2016, **16**, 57-69.

[2] Z. W. Seh, J. Kibsgaard, C. F. Dickens, I. Chorkendorff, J. K. Nørskov, T. F. Jaramillo, *Science*, 2017, **355**, eaad4998.

[3] C. Copéret, M. Chabanas, R. Petroff Saint-Arroman, J.-M. Basset, *Angew. Chem. Int. Ed.*, 2003, **42**, 156-181.

[4] S. Hübner, J. G. de Vries, V. Farina, *Adv. Synth. Catal.*, 2016, **358**, 3-25.

[5] S. Zhao, Y. Wang, J. Dong, C.-T. He, H. Yin, P. An, K. Zhao, X. Zhang, C. Gao, L. Zhang, J. Lv, J. Wang, J. Zhang, A. M. Khattak, N. A. Khan, Z. Wei, J. Zhang, S. Liu, H. Zhao, Z. Tang, *Nat. Energy*, 2016, **1**, 16184.

[6] B. C. Gates, *Chem. Rev.*, 1995, **95**, 511-522.

[7] X.-F. Yang, A. Wang, B. Qiao, J. Li, J. Liu, T. Zhang, *Acc. Chem. Res.*, 2013, **46**, 1740-1748.

[8] J. Liu, *ACS Catal.*, 2017, **7**, 34-59.

[9] A. Wang, J. Li, T. Zhang, *Nat. Rev. Chem.*, 2018, **2**, 65-81.

[10] X. Cui, W. Li, P. Ryabchuk, K. Junge, M. Beller, *Nat. Catal.*, 2018, **1**, 385-397.

[11] R. Qin, P. Liu, G. Fu, N. Zheng, *Small Methods*, 2017, **2**, 1700286.

[12] M. Hu, J. Zhang, W. Zhu, Z. Chen, X. Gao, X. Du, J. Wan, K. Zhou, C. Chen, Y. Li, *Nano Res.*, 2018, **11**, 905-912.

[13] H. Zhang, G. Liu, L. Shi, J. Ye, *Adv. Energy Mater.*, 2017, **8**, 1701343.

[14] C. Zhu, S. Fu, Q. Shi, D. Du, Y. Lin, *Angew. Chem. Int. Ed.*, 2017, **56**, 13944-13960.

[15] M. Dhiman, V. Polshettiwar, *ChemCatChem*, 2017, **10**, 881-906.

[16] B. Bayatsarmadi, Y. Zheng, A. Vasileff, S.-Z. Qiao, *Small*, 2017, **13**, 1700191.

[17] Y. Peng, B. Lu, S. Chen, *Adv. Mater.*, 2018, **30**, 1801995.

[18] B. Long, Y. Tang, J. J. N. R. Li, *Nano Res.*, 2016, **9**, 3868-3880.

[19] J. Liang, Q. Yu, X. Yang, T. Zhang, J. Li, *Nano Res.*, 2018, **11**, 1599-1611.

[20] K. S. Novoselov, V. I. Fal ′ko, L. Colombo, P. R. Gellert, M. G. Schwab, K. Kim, *Nature*, 2012, **490**, 192-200.

[21] H. Wang, H. S. Casalongue, Y. Liang, H. Dai, *J. Am. Chem. Soc.*, 2010, **132**, 7472-7477.

[22] S. Hu, T. Han, C. Lin, W. Xiang, Y. Zhao, P. Gao, F. Du, X. Li, Y. Sun, *Adv. Funct. Mater.*, 2017, **27**, 1700041.

[23] P. Kundu, C. Nethravathi, P. A. Deshpande, M. Rajamathi, G. Madras, N. Ravishankar, *Chem. Mater.*, 2011, **23**, 2772-2780.

[24] M. Liu, R. Zhang, W. Chen, *Chem. Rev.*, 2014, **114**, 5117-5160.

[25] H. Fei, J. Dong, Y. Feng, C. S. Allen, C. Wan, B. Volosskiy, M. Li, Z. Zhao, Y. Wang, H. Sun, P. An, W. Chen, Z. Guo, C. Lee, D. Chen, I. Shakir, M. Liu, T. Hu, Y. Li, A. I. Kirkland, X. Duan, Y. Huang, *Nat. Catal.*, 2018, **1**, 63-72.

[26] J. Luo, D. A. Vermaas, D. Bi, A. Hagfeldt, W. A. Smith, M. Grätzel, *Adv. Energy Mater.*, 2016, **6**, 1600100.

[27] W. I. Choi, B. C. Wood, E. Schwegler, T. Ogitsu, *Adv. Energy Mater.*, 2015, **5**, 1501423.

[28] A. V. Krasheninnikov, P. O. Lehtinen, A. S. Foster, P. Pyykkö, R. M. Nieminen, *Phys. Rev. Lett.*, 2009, **102**, 126807.

[29] H. Wang, Q. Wang, Y. Cheng, K. Li, Y. Yao, Q. Zhang, C. Dong, P. Wang, U. Schwingenschlögl, W. Yang, X. X. Zhang, *Nano Lett.*, 2012, **12**, 141-144.

[30] A. W. Robertson, B. Montanari, K. He, J. Kim, C. S. Allen, Y. A. Wu, J. Olivier, J. Neethling, N. Harrison, A. I. Kirkland, J. H. Warner, *Nano Lett.*, 2013, **13**, 1468-1475.

[31] J. Zhao, Q. Deng, S. M. Avdoshenko, L. Fu, J. Eckert, M. H. Rümmeli, *PNAS*, 2014, **111**, 15641.

[32] J. Duan, S. Chen, M. Jaroniec, S. Z. Qiao, *ACS Catal.*, 2015, **5**, 5207-5234.

[33] D. Deng, X. Chen, L. Yu, X. Wu, Q. Liu, Y. Liu, H. Yang, H. Tian, Y. Hu, P. Du, R. Si, J. Wang, X. Cui, H. Li, J. Xiao, T. Xu, J. Deng, F. Yang, P. N. Duchesne, P. Zhang, J. Zhou, L. Sun, J. Li, X. Pan, X. Bao, *Sci. Adv.*, 2015, **1**, e1500462.

[34] F. Vines, J. R. B. Gomes, F. Illas, *Chem. Soc. Rev.*, 2014, **43**, 4922-4939.

[35] P. Strasser, S. Koh, T. Anniyev, J. Greeley, K. More, C. Yu, Z. Liu, S. Kaya, D. Nordlund, H. Ogasawara, M. F. Toney, A. Nilsson, *Nat. Chem.*, 2010, **2**, 454-460.

[36] G. Chen, C. Xu, X. Huang, J. Ye, L. Gu, G. Li, Z. Tang, B. Wu, H. Yang, Z. Zhao, Z. Zhou, G. Fu, N. Zheng, *Nat. Mater.*, 2016, **15**, 564-569.

[37] V. R. Stamenkovic, B. S. Mun, M. Arenz, K. J. J. Mayrhofer, C. A. Lucas, G. Wang, P. N. Ross, N. M. Markovic, *Nat. Mater.*, 2007, **6**, 241-247.

[38] D. J. Gorin, B. D. Sherry, F. D. Toste, *Chem. Rev.*, 2008, **108**, 3351-3378.

[39] H. Xu, D. Cheng, D. Cao, X. C. Zeng, *Nat. Catal.*, 2018, **1**, 339-348.

[40] V. Tripkovic, M. Vanin, M. Karamad, M. E. Björketun, K. W. Jacobsen, K. S. Thygesen, J. Rossmeisl, *J. Phys. Chem. C*, 2013, **117**, 9187-9195.

[41] S. Back, J. Lim, N.-Y. Kim, Y.-H. Kim, Y. Jung, *Chem. Sci.*, 2017, **8**, 1090-1096.

[42] C. Choi, S. Back, N.-Y. Kim, J. Lim, Y.-H. Kim, Y. Jung, *ACS Catal.*, 2018, **8**, 7517-7525.

[43] A. Zitolo, V. Goellner, V. Armel, M.-T. Sougrati, T. Mineva, L. Stievano, E. Fonda, F. Jaouen, *Nat. Mater.*, 2015, **14**, 937-942.

[44] A. Zitolo, N. Ranjbar-Sahraie, T. Mineva, J. Li, Q. Jia, S. Stamatin, G. F. Harrington, S. M. Lyth, P. Krtil, S. Mukerjee, E. Fonda, F. Jaouen, *Nat. Commun.*, 2017, **8**, 957.

[45] X. Wang, Z. Chen, X. Zhao, T. Yao, W. Chen, R. You, C. Zhao, G. Wu, J. Wang, W. Huang, J. Yang, X. Hong, S. Wei, Y. Wu, Y. Li, *Angew. Chem. Int. Ed.*, 2018, **57**, 1944-1948.

[46] H. B. Yang, S.-F. Hung, S. Liu, K. Yuan, S. Miao, L. Zhang, X. Huang, H.-Y. Wang, W. Cai, R. Chen, J. Gao, X. Yang, W. Chen, Y. Huang, H. M. Chen, C. M. Li, T. Zhang, B. Liu, *Nat. Energy*, 2018, **3**, 140-147.

[47] Y. Guo, P. Yuan, J. Zhang, Y. Hu, I. S. Amiinu, X. Wang, J. Zhou, H. Xia, Z. Song, Q. Xu, S. Mu, *ACS Nano*, 2018, **12**, 1894-1901.

[48] Y. Hou, M. Qiu, M. G. Kim, P. Liu, G. Nam, T. Zhang, X. Zhuang, B. Yang, J. Cho, M. Chen, C. Yuan, L. Lei, X. Feng, *Nat. Commun.*, 2019, **10**, 1392.

[49] Y. Han, Y. Wang, R. Xu, W. Chen, L. Zheng, A. Han, Y. Zhu, J. Zhang, H. Zhang, J. Luo, C. Chen, Q. Peng, D. Wang, Y. Li, *Energy Environ. Sci.*, 2018, **11**, 2348-2352.

[50] H. C. Kwon, M. Kim, J. P. Grote, S. J. Cho, M. W. Chung, H. Kim, D. H. Won, A. R. Zeradjanin, K. J. J. Mayrhofer, M. Choi, H. Kim, C. H. Choi, *J. Am. Chem. Soc.*, 2018, **140**, 16198-16205.

[51] H. T. Chung, D. A. Cullen, D. Higgins, B. T. Sneed, E. F. Holby, K. L. More, P. Zelenay, *Science*, 2017, **357**, 479.

[52] N. Ramaswamy, U. Tylus, Q. Jia, S. Mukerjee, *J. Am. Chem. Soc.*, 2013, **135**, 15443-15449.

[53] X. Fu, N. Li, B. Ren, G. Jiang, Y. Liu, F. M. Hassan, D. Su, J. Zhu, L. Yang, Z. Bai, Z. P. Cano, A. Yu, Z. Chen, *Adv. Energy Mater.*, 2019, **9**, 1803737.

[54] Y. Wang, D. Adekoya, J. Sun, T. Tang, H. Qiu, L. Xu, S. Zhang, Y. Hou, *Adv. Funct. Mater.*, 2018, **29**, 1807485.

[55] R. Jiang, L. Li, T. Sheng, G. Hu, Y. Chen, L. Wang, *J. Am. Chem. Soc.*, 2018, **140**, 11594-11598.

[56] K. Liu, H. Zhong, F. Meng, X. Zhang, J. Yan, Q. Jiang, *Mater. Chem. Front.*, 2017, **1**, 2155-2173.

[57] P. Chen, T. Zhou, L. Xing, K. Xu, Y. Tong, H. Xie, L. Zhang, W. Yan, W. Chu, C. Wu, Y. Xie, *Angew. Chem. Int. Ed.*, 2017, **56**, 610-614.

[58] D. Liu, C. Wu, S. Chen, S. Ding, Y. Xie, C. Wang, T. Wang, Y. A. Haleem, Z. ur Rehman, Y. Sang, Q. Liu, X. Zheng, Y. Wang, B. Ge, H. Xu, L. Song, *Nano Res.*, 2018, **11**, 2217-2228.

[59] G. Zhang, Y. Jia, C. Zhang, X. Xiong, K. Sun, R. Chen, W. Chen, Y. Kuang, L. Zheng, H. Tang, W. Liu, J. Liu, X. Sun, W.-F. Lin, H. Dai, *Energy Environ. Sci.*, 2019, **12**, 1317-1325.

[60] T. Sun, S. Zhao, W. Chen, D. Zhai, J. Dong, Y. Wang, S. Zhang, A. Han, L. Gu, R. Yu, X. Wen, H. Ren, L. Xu, C. Chen, Q. Peng, D. Wang, Y. Li, *PNAS*, 2018, **115**, 12692.

[61] X.-M. Hu, H. H. Hval, E. T. Bjerglund, K. J. Dalgaard, M. R. Madsen, M.-M. Pohl, E. Welter, P. Lamagni, K. B. Buhl, M. Bremholm, M. Beller, S. U. Pedersen, T. Skrydstrup, K. Daasbjerg, *ACS Catal.*, 2018, **8**, 6255-6264.

[62] L. Zhao, Y. Zhang, L.-B. Huang, X.-Z. Liu, Q.-H. Zhang, C. He, Z.-Y. Wu, L.-J. Zhang, J. Wu, W. Yang, L. Gu, J.-S. Hu, L.-J. Wan, *Nat. Commun.*, 2019, **10**, 1278.

[63] K. Yuan, S. Sfaelou, M. Qiu, D. Lützenkirchen-Hecht, X. Zhuang, Y. Chen, C. Yuan, X. Feng, U. Scherf, *ACS Energy Lett.*, 2018, **3**, 252-260.

[64] Y. Chen, S. Ji, S. Zhao, W. Chen, J. Dong, W.-C. Cheong, R. Shen, X. Wen, L. Zheng, A. I. Rykov, S. Cai, H. Tang, Z. Zhuang, C. Chen, Q. Peng, D. Wang, Y. Li, *Nat. Commun.*, 2018, **9**, 5422.

[65] H. Shen, E. Gracia-Espino, J. Ma, K. Zang, J. Luo, L. Wang, S. Gao, X. Mamat, G. Hu, T. Wagberg, S. Guo, *Angew. Chem. Int. Ed.*, 2017, **56**, 13800-13804.

[66] C. Zhang, J. Sha, H. Fei, M. Liu, S. Yazdi, J. Zhang, Q. Zhong, X. Zou, N. Zhao, H. Yu, Z. Jiang, E. Ringe, B. I. Yakobson, J. Dong, D. Chen, J. M. Tour, *ACS Nano*, 2017, **11**, 6930-6941.

[67] D. C. Marcano, D. V. Kosynkin, J. M. Berlin, A. Sinitskii, Z. Sun, A. Slesarev, L. B. Alemany, W. Lu, J. M. Tour, *ACS Nano*, 2010, **4**, 4806-4814.

[68] K. Chen, S. Song, F. Liu, D. Xue, *Chem. Soc. Rev.*, 2015, **44**, 6230-6257.

[69] L. Dai, *Acc. Chem. Res.*, 2013, **46**, 31-42.

[70] I. K. Moon, J. Lee, R. S. Ruoff, H. Lee, *Nat. Commun.*, 2010, **1**, 73.

[71] A. Bagri, C. Mattevi, M. Acik, Y. J. Chabal, M. Chhowalla, V. B. Shenoy, *Nat. Chem.*, 2010, **2**, 581-587.

[72] H. Fei, J. Dong, M. J. Arellano-Jiménez, G. Ye, N. Dong Kim, E. L. G. Samuel, Z. Peng, Z. Zhu, F. Qin, J. Bao, M. J. Yacaman, P. M. Ajayan, D. Chen, J. M. Tour, *Nat. Commun.*, 2015, **6**, 8668.

[73] K. Jiang, S. Siahrostami, T. Zheng, Y. Hu, S. Hwang, E. Stavitski, Y. Peng, J. J. Dynes, M. Gangishetty, D. Su, K. Attenkofer, H. Wang, *Energy Environ. Sci.*, 2018, **11**, 893-903.

[74] J. Guan, Z. Duan, F. Zhang, S. D. Kelly, R. Si, M. Dupuis, Q. Huang, J. Q. Chen, C. Tang, C. Li, *Nat. Catal.*, 2018, **1**, 870-877.

[75] X. Wen, Z. Duan, L. Bai, J. Guan, *J. Power Sources*, 2019, **431**, 265-273.

[76] H. Fei, J. Dong, C. Wan, Z. Zhao, X. Xu, Z. Lin, Y. Wang, H. Liu, K. Zang, J. Luo, S. Zhao, W. Hu, W. Yan, I. Shakir, Y. Huang, X. Duan, *Adv. Mater.*, 2018, **30**, 1802146.

[77] B. Y. Guan, X. Y. Yu, H. B. Wu, X. W. Lou, *Adv. Mater.*, 2017, **29**, 1703614.

[78] S. Dang, Q.-L. Zhu, Q. Xu, *Nat. Rev. Mater.*, 2017, **3**, 17075.

[79] J. Liu, D. Zhu, C. Guo, A. Vasileff, S.-Z. Qiao, *Adv. Energy Mater.*, 2017, **7**, 1700518.

[80] M. Xiao, J. Zhu, G. Li, N. Li, S. Li, Z. P. Cano, L. Ma, P. X. Cui, P. Xu, G. Jiang, H. Jin, S. Wang, T. Wu, J. Lu, A. Yu, D. Su, Z. Chen, *Angew. Chem.*, 2019, **131**, 9742.

[81] J. Han, X. Meng, L. Lu, J. Bian, Z. Li, C. Sun, *Adv. Funct. Mater.*, 2019, DOI: 10.1002/adfm.201808872.

[82] J. Wu, H. Zhou, Q. Li, M. Chen, J. Wan, N. Zhang, L. Xiong, S. Li, B. Y. Xia, G. Feng, M. Liu, L. Huang, *Adv. Energy Mater.*, 2019, **9**, 1900149.

[83] T. Sun, L. Xu, D. Wang, Y. Li, *Nano Res.*, 2019, DOI: 10.1007/s12274-019-2345-4.

[84] Y. Qu, Z. Li, W. Chen, Y. Lin, T. Yuan, Z. Yang, C. Zhao, J. Wang, C. Zhao, X. Wang, F. Zhou, Z. Zhuang, Y. Wu, Y. Li, *Nat. Catal.*, 2018, **1**, 781-786.

[85] X. Wan, X. Liu, Y. Li, R. Yu, L. Zheng, W. Yan, H. Wang, M. Xu, J. Shui, *Nat. Catal.*, 2019, **2**, 259-268.

[86] S. Wei, A. Li, J.-C. Liu, Z. Li, W. Chen, Y. Gong, Q. Zhang, W.-C. Cheong, Y. Wang, L. Zheng, H. Xiao, C. Chen, D. Wang, Q. Peng, L. Gu, X. Han, J. Li, Y. Li, *Nat. Nano.*, 2018, **13**, 856-861.

[87] Y. Chen, S. Ji, Y. Wang, J. Dong, W. Chen, Z. Li, R. Shen, L. Zheng, Z. Zhuang, D. Wang, Y. Li, *Angew. Chem.*, 2017, **129**, 7041-7045.

[88] M. Xiao, J. Zhu, L. Ma, Z. Jin, J. Ge, X. Deng, Y. Hou, Q. He, J. Li, Q. Jia, S. Mukerjee, R. Yang, Z. Jiang, D. Su, C. Liu, W. Xing, *ACS Catal.*, 2018, **8**, 2824-2832.

[89] P. Yin, T. Yao, Y. Wu, L. Zheng, Y. Lin, W. Liu, H. Ju, J. Zhu, X. Hong, Z. Deng, G. Zhou, S. Wei, Y. Li, *Angew. Chem. Int. Ed.*, 2016, **55**, 10800-10805.

[90] L. Jiao, H.-L. Jiang, *Chem*, 2019, **5**, 786-804.

[91] J. Li, M. Chen, D. A. Cullen, S. Hwang, M. Wang, B. Li, K. Liu, S. Karakalos, M. Lucero, H. Zhang, C. Lei, H. Xu, G. E. Sterbinsky, Z. Feng, D. Su, K. L. More, G. Wang, Z. Wang, G. Wu, *Nat. Catal.*, 2018, **1**, 935-945.

[92] X. Wang, W. Chen, L. Zhang, T. Yao, W. Liu, Y. Lin, H. Ju, J. Dong, L. Zheng, W. Yan, X. Zheng, Z. Li, X. Wang, J. Yang, D. He, Y. Wang, Z. Deng, Y. Wu, Y. Li, *J. Am. Chem. Soc.*, 2017, **139**, 9419-9422.

[93] Y. Deng, B. Chi, J. Li, G. Wang, L. Zheng, X. Shi, Z. Cui, L. Du, S. Liao, K. Zang, J. Luo, Y. Hu, X. Sun, *Adv. Energy Mater.*, 2019, **9**, 1802856.

[94] Y. Qu, B. Chen, Z. Li, X. Duan, L. Wang, Y. Lin, T. Yuan, F. Zhou, Y. Hu, Z. Yang, C. Zhao, J. Wang, C. Zhao, Y. Hu, G. Wu, Q. Zhang, Q. Xu, B. Liu, P. Gao, R. You, W. Huang, L. Zheng, L. Gu, Y. Wu, Y. Li, *J. Am. Chem. Soc.*, 2019, **141**, 4505-4509.

[95] J. Yang, Z. Qiu, C. Zhao, W. Wei, W. Chen, Z. Li, Y. Qu, J. Dong, J. Luo, Z. Li, Y. Wu, *Angew. Chem. Int. Ed.*, 2018, **57**, 14095-14100.

[96] H. Yan, H. Cheng, H. Yi, Y. Lin, T. Yao, C. Wang, J. Li, S. Wei, J. Lu, *J. Am. Chem. Soc.*, 2015, **137**, 10484-10487.

[97] H. Wei, H. Wu, K. Huang, B. Ge, J. Ma, J. Lang, D. Zu, M. Lei, Y. Yao, W. Guo, H. Wu, *Chem. Sci.*, 2019, **10**, 2830-2836.

[98] K. Huang, L. Zhang, T. Xu, H. Wei, R. Zhang, X. Zhang, B. Ge, M. Lei, J.-Y. Ma, L.-M. Liu, H. Wu, *Nat. Commun.*, 2019, **10**, 606.

[99] W. Bi, X. Li, R. You, M. Chen, R. Yuan, W. Huang, X. Wu, W. Chu, C. Wu, Y. Xie, *Adv. Mater.*, 2018, **30**, 1706617.

[100] E. Kano, A. Hashimoto, T. Kaneko, N. Tajima, T. Ohno, M. Takeguchi, *Nanoscale*, 2016, **8**, 529-535.

[101] Z. He, K. He, A. W. Robertson, A. I. Kirkland, D. Kim, J. Ihm, E. Yoon, G.-D. Lee, J. H. Warner, *Nano Lett.*, 2014, **14**, 3766-3772.

[102] S. L. James, C. J. Adams, C. Bolm, D. Braga, P. Collier, T. Friscic, F. Grepioni, K. D. M. Harris, G. Hyett, W. Jones, A. Krebs, J. Mack, L. Maini, A. G. Orpen, I. P. Parkin, W. C. Shearouse, J. W. Steed, D. C. Waddell, *Chem. Soc. Rev.*, 2012, **41**, 413-447.

[103] M. Yi, Z. Shen, *J. Mater. Chem. A*, 2015, **3**, 11700-11715.

[104] X. Cui, J. Xiao, Y. Wu, P. Du, R. Si, H. Yang, H. Tian, J. Li, W.-H. Zhang, D. Deng, X. Bao, *Angew. Chem. Int. Ed.*, 2016, **55**, 6708-6712.

[105] J. Lu, J. W. Elam, P. C. Stair, *Acc. Chem. Res.*, 2013, **46**, 1806-1815.

[106] S. Sun, G. Zhang, N. Gauquelin, N. Chen, J. Zhou, S. Yang, W. Chen, X. Meng, D. Geng, M. N. Banis, R. Li, S. Ye, S. Knights, G. A. Botton, T.-K. Sham, X. Sun, *Sci. Rep.*, 2013, **3**, 1775.

[107] S. Stambula, N. Gauquelin, M. Bugnet, S. Gorantla, S. Turner, S. Sun, J. Liu, G. Zhang, X. Sun, G. A. Botton, *J. Phys. Chem. C*, 2014, **118**, 3890-3900.

[108] N. Cheng, S. Stambula, D. Wang, M. N. Banis, J. Liu, A. Riese, B. Xiao, R. Li, T.-K. Sham, L.-M. Liu, G. A. Botton, X. Sun, *Nat. Commun.*, 2016, **7**, 13638.

[109] S. Linic, U. Aslam, C. Boerigter, M. Morabito, *Nat. Mater.*, 2015, **14**, 567.

[110] H. Wei, K. Huang, D. Wang, R. Zhang, B. Ge, J. Ma, B. Wen, S. Zhang, Q. Li, M. Lei, C. Zhang, J. Irawan, L.-M. Liu, H. Wu, *Nat. Commun.*, 2017, **8**, 1490.

[111] T. Li, J. Liu, Y. Song, F. Wang, *ACS Catal.*, 2018, **8**, 8450-8458.

[112] Z. Zhang, Y. Chen, L. Zhou, C. Chen, Z. Han, B. Zhang, Q. Wu, L. Yang, L. Du, Y. Bu, P. Wang, X. Wang, H. Yang, Z. Hu, *Nat. Commun.*, 2019, **10**, 1657.

[113] Q. Lai, Y. Zhao, J. Zhu, Y. Liang, J. He, J. Chen, *ChemElectroChem*, 2018, **5**, 1822-1826.

[114] A. Bakandritsos, R. G. Kadam, P. Kumar, G. Zoppellaro, M. Medved', J. Tuček, T. Montini, O. Tomanec, P. Andrýsková, B. Drahoš, R. S. Varma, M. Otyepka, M. B. Gawande, P. Fornasiero, R. Zbořil, *Adv. Mater.*, 2019, **31**, 1900323.

[115] G. Malta, S. A. Kondrat, S. J. Freakley, C. J. Davies, L. Lu, S. Dawson, A. Thetford, E. K. Gibson, D. J. Morgan, W. Jones, P. P. Wells, P. Johnston, C. R. A. Catlow, C. J. Kiely, G. J. Hutchings, *Science*, 2017, **355**, 1399.

[116] J. J. Rehr, R. C. Albers, *Rev. Mod. Phys.*, 2000, **72**, 621-654.

[117] S. Bordiga, E. Groppo, G. Agostini, J. A. van Bokhoven, C. Lamberti, *Chem. Rev.*, 2013, **113**, 1736-1850.

[118] D. C. Koningsberger, R. Prins, *X-ray absorption: principles, applications, techniques of EXAFS, SEXAFS, and XANES*, John Wiley and Sons, New York, NY, 1988.

[119] H. Funke, A. C. Scheinost, M. Chukalina, *Phy. Rev. B*, 2005, **71**, 094110.

[120] Y. Chen, S. Ji, W. Sun, W. Chen, J. Dong, J. Wen, J. Zhang, Z. Li, L. Zheng, C. Chen, Q. Peng, D. Wang, Y. Li, *J. Am. Chem. Soc.*, 2018, **140**, 7407-7410.

[121] J. Yang, B. Chen, X. Liu, W. Liu, Z. Li, J. Dong, W. Chen, W. Yan, T. Yao, X. Duan, Y. Wu, Y. Li, *Angew. Chem. Int. Ed.*, 2018, **57**, 9495-9500.

[122] W. Liu, L. Zhang, W. Yan, X. Liu, X. Yang, S. Miao, W. Wang, A. Wang, T. Zhang, *Chem. Sci.*, 2016, **7**, 5758-5764.

[123] M. Benfatto, S. Della Longa, C. R. Natoli, *J. Synchrotron Radiat.*, 2003, **10**, 51-57.

[124] K. Hayakawa, K. Hatada, S. Della Longa, P. D'Angelo, M. Benfatto, *AIP Conf. Proc.*, 2007, **882**, 111-113.

[125] X. Li, X. Yang, J. Zhang, Y. Huang, B. Liu, *ACS Catal.*, 2019, **9**, 2521-2531.

[126] L. Cao, Q. Luo, W. Liu, Y. Lin, X. Liu, Y. Cao, W. Zhang, Y. Wu, J. Yang, T. Yao, S. Wei, *Nat. Catal.*, 2019, **2**, 134-141.

[127] B. Lassalle-Kaiser, S. Gul, J. Kern, V. K. Yachandra, J. Yano, *J. Electron Spectrosc. Relat. Phenom.*, 2017, **221**, 18-27.

[128] J. Gu, C.-S. Hsu, L. Bai, H. M. Chen, X. Hu, *Science*, 2019, **364**, 1091.

[129] G. B. B. Varadwaj, V. O. Nyamori, *Nano Res.*, 2016, **9**, 3598-3621.

[130] C. H. Choi, M. Kim, H. C. Kwon, S. J. Cho, S. Yun, H.-T. Kim, K. J. J. Mayrhofer, H. Kim, M. Choi, *Nat. Commun.*, 2016, **7**, 10922.

[131] T. Sun, B. Tian, J. Lu, C. Su, *J. Mater. Chem. A*, 2017, **5**, 18933-18950.

[132] A. Serov, K. Artyushkova, P. Atanassov, *Adv. Energy Mater.*, 2014, **4**, 1301735.

[133] G. Wu, *Front. Energy*, 2017, **11**, 286-298.

[134] L. Yang, D. Cheng, H. Xu, X. Zeng, X. Wan, J. Shui, Z. Xiang, D. Cao, *PNAS*, 2018, **115**, 6626-6631.

[135] Y. He, S. Hwang, D. A. Cullen, M. A. Uddin, L. Langhorst, B. Li, S. Karakalos, A. J. Kropf, E. C. Wegener, J. Sokolowski, M. Chen, D. Myers, D. Su, K. L. More, G. Wang, S. Litster, G. Wu, *Energy Environ. Sci.*, 2018, **12**, 250-260.

[136] J. Liu, M. Jiao, B. Mei, Y. Tong, Y. Li, M. Ruan, P. Song, G. Sun, L. Jiang, Y. Wang, Z. Jiang, L. Gu, Z. Zhou, W. Xu, *Angew. Chem. Int. Ed.*, 2018, **58**, 1163-1167.

[137] F. Li, G.-F. Han, H.-J. Noh, S.-J. Kim, Y. Lu, H. Y. Jeong, Z. Fu, J.-B. Baek, *Energy Environ. Sci.*, 2018, **11**, 2263-2269.

[138] J. Li, S. Chen, N. Yang, M. Deng, S. Ibraheem, J. Deng, J. Li, L. Li, Z. Wei, *Angew. Chem. Int. Ed.*, 2019, **58**, 7035-7039.

[139] J. D. Holladay, J. Hu, D. L. King, Y. Wang, *Catal. Today*, 2009, **139**, 244-260.

[140] J. K. Nørskov, T. Bligaard, A. Logadottir, J. R. Kitchin, J. G. Chen, S. Pandelov, U. Stimming, *J. Electrochem. Soc.*, 2005, **152**, J23-J26.

[141] D. Liu, X. Li, S. Chen, H. Yan, C. Wang, C. Wu, Y. A. Haleem, S. Duan, J. Lu, B. Ge, P. M. Ajayan, Y. Luo, J. Jiang, L. Song, *Nat. Energy*, 2019, **4**, 512-518.

[142] H. Zhang, P. An, W. Zhou, B. Y. Guan, P. Zhang, J. Dong, X. W. Lou, *Sci. Adv.*, 2018, **4**, eaao6657.

[143] H. J. Qiu, Y. Ito, W. Cong, Y. Tan, P. Liu, A. Hirata, T. Fujita, Z. Tang, M. Chen, *Angew. Chem. Int. Ed.*, 2015, **54**, 14031-14035.

[144] L. Fan, P. F. Liu, X. Yan, L. Gu, Z. Z. Yang, H. G. Yang, S. Qiu, X. Yao, *Nat. Commun.*, 2016, **7**, 10667.

[145] L. Zhang, Y. Jia, G. Gao, X. Yan, N. Chen, J. Chen, M. T. Soo, B. Wood, D. Yang, A. Du, X. Yao, *Chem*, 2018, **4**, 285-297.

[146] Z.-L. Wang, X.-F. Hao, Z. Jiang, X.-P. Sun, D. Xu, J. Wang, H.-X. Zhong, F.-L. Meng, X.-B. Zhang, *J. Am. Chem. Soc.*, 2015, **137**, 15070-15073.

[147] H.-W. Liang, S. Brüller, R. Dong, J. Zhang, X. Feng, K. Müllen, *Nat. Commun.*, 2015, **6**, 7992.

[148] M. D. Hossain, Z. Liu, M. Zhuang, X. Yan, G.-L. Xu, C. A. Gadre, A. Tyagi, I. H. Abidi, C.-J. Sun, H. Wong, A. Guda, Y. Hao, X. Pan, K. Amine, Z. Luo, *Adv. Energy Mater.*, 2019, **9**, 1803689.

[149] W. Chen, J. Pei, C.-T. He, J. Wan, H. Ren, Y. Zhu, Y. Wang, J. Dong, S. Tian, W.-C. Cheong, S. Lu, L. Zheng, X. Zheng, W. Yan, Z. Zhuang, C. Chen, Q. Peng, D. Wang, Y. Li, *Angew. Chem.*, 2017, **129**, 16302-16306.

[150] C. Wenxing, P. Jiajing, H. Chun-Ting, W. Jiawei, R. Hanlin, W. Yu, D. Juncai, W. Konglin, C. Weng-Chon, M. Junjie, Z. Xusheng, Y. Wensheng, Z. Zhongbin, C. Chen, P. Qing, W. Dingsheng, L. Yadong, *Adv. Mater.*, 2018, **30**, 1800396.

[151] Y. Pan, S. Liu, K. Sun, X. Chen, B. Wang, K. Wu, X. Cao, W.-C. Cheong, R. Shen, A. Han, Z. Chen, L. Zheng, J. Luo, Y. Lin, Y. Liu, D. Wang, Q. Peng, Q. Zhang, C. Chen, Y. Li, *Angew. Chem.*, 2018, **57**, 8614-8618.

[152] P. Du, R. Eisenberg, *Energy Environ. Sci.*, 2012, **5**, 6012-6021.

[153] B. Kumar, J. P. Brian, V. Atla, S. Kumari, K. A. Bertram, R. T. White, J. M. Spurgeon, *Catal. Today*, 2016, **270**, 19-30.

[154] L. Zhang, Z.-J. Zhao, J. Gong, *Angew. Chem. Int. Ed.*, 2017, **56**, 11326-11353.

[155] X. Su, X.-F. Yang, Y. Huang, B. Liu, T. Zhang, *Acc. Chem. Res.*, 2019, **52**, 656-664.

[156] A. S. Varela, W. Ju, A. Bagger, P. Franco, J. Rossmeisl, P. Strasser, *ACS Catal.*, 2019, **9**, 7270-7284.

[157] P. Su, K. Iwase, S. Nakanishi, K. Hashimoto, K. Kamiya, *Small*, 2016, **12**, 6083-6089.

[158] C. Zhao, X. Dai, T. Yao, W. Chen, X. Wang, J. Wang, J. Yang, S. Wei, Y. Wu, Y. Li, *J. Am. Chem. Soc.*, 2017, **139**, 8078-8081.

[159] X. Li, W. Bi, M. Chen, Y. Sun, H. Ju, W. Yan, J. Zhu, X. Wu, W. Chu, C. Wu, Y. Xie, *J. Am. Chem. Soc.*, 2017, **139**, 14889-14892.

[160] K. Jiang, S. Siahrostami, A. J. Akey, Y. Li, Z. Lu, J. Lattimer, Y. Hu, C. Stokes, M. Gangishetty, G. Chen, Y. Zhou, W. Hill, W.-B. Cai, D. Bell, K. Chan, J. K. Nørskov, Y. Cui, H. Wang, *Chem*, 2017, **3**, 950-960.

[161] C. Yan, H. Li, Y. Ye, H. Wu, F. Cai, R. Si, J. Xiao, S. Miao, S. Xie, F. Yang, Y. Li, G. Wang, X. Bao, *Energy Environ. Sci.*, 2018, **11**, 1204-1210.

[162] A. S. Varela, N. Ranjbar Sahraie, J. Steinberg, W. Ju, H.-S. Oh, P. Strasser, *Angew. Chem. Int. Ed.*, 2015, **54**, 10758-10762.

[163] F. Pan, H. Zhang, K. Liu, D. Cullen, K. More, M. Wang, Z. Feng, G. Wang, G. Wu, Y. Li, *ACS Catal.*, 2018, **8**, 3116-3122.

[164] F. Yang, P. Song, X. Liu, B. Mei, W. Xing, Z. Jiang, L. Gu, W. Xu, *Angew. Chem. Int. Ed.*, 2018, **57**, 12303-12307.

[165] X. Zu, X. Li, W. Liu, Y. Sun, J. Xu, T. Yao, W. Yan, S. Gao, C. Wang, S. Wei, Y. Xie, *Adv. Mater.*, 2019, **31**, 1808135.

[166] C. Zhao, Y. Wang, Z. Li, W. Chen, Q. Xu, D. He, D. Xi, Q. Zhang, T. Yuan, Y. Qu, J. Yang, F. Zhou, Z. Yang, X. Wang, J. Wang, J. Luo, Y. Li, H. Duan, Y. Wu, Y. Li, *Joule*, 2019, **3**, 584-594.

[167] P. Lu, Y. Yang, J. Yao, M. Wang, S. Dipazir, M. Yuan, J. Zhang, X. Wang, Z. Xie, G. Zhang, *Appl. Catal., B*, 2019, **241**, 113-119.

[168] B. Zhang, J. Zhang, J. Shi, D. Tan, L. Liu, F. Zhang, C. Lu, Z. Su, X. Tan, X. Cheng, B. Han, L. Zheng, J. Zhang, *Nat. Commun.*, 2019, **10**, 2980.

[169] Y. Cheng, S. Yang, S. P. Jiang, S. Wang, *Small Methods*, 2019, DOI: 10.1002/smtd.201800440.

[170] Y. Cheng, S. Zhao, H. Li, S. He, J.-P. Veder, B. Johannessen, J. Xiao, S. Lu, J. Pan, M. F. Chisholm, S.-Z. Yang, C. Liu, J. G. Chen, S. P. Jiang, *Appl. Catal., B*, 2019, **243**, 294-303.

[171] T. Zheng, K. Jiang, N. Ta, Y. Hu, J. Zeng, J. Liu, H. Wang, *Joule*, 2019, **3**, 265-278.

[172] Z. Chen, K. Mou, S. Yao, L. Liu, *ChemSusChem*, 2018, **11**, 2944-2952.

[173] C. Zhang, S. Yang, J. Wu, M. Liu, S. Yazdi, M. Ren, J. Sha, J. Zhong, K. Nie, A. S. Jalilov, Z. Li, H. Li, B. I. Yakobson, Q. Wu, E. Ringe, H. Xu, P. M. Ajayan, J. M. Tour, *Adv. Energy Mater.*, 2018, **8**, 1703487.

[174] T. N. Huan, N. Ranjbar, G. Rousse, M. Sougrati, A. Zitolo, V. Mougel, F. Jaouen, M. Fontecave, *ACS Catal.*, 2017, **7**, 1520-1525.

[175] T. Möller, W. Ju, A. Bagger, X. Wang, F. Luo, T. N. Thanh, A. Varela, J. Rossmeisl, P. Strasser, *Energy Environ. Sci.*, 2019, **12**, 640-647.

[176] W. Ju, A. Bagger, G.-P. Hao, A. S. Varela, I. Sinev, V. Bon, B. Roldan Cuenya, S. Kaskel, J. Rossmeisl, P. Strasser, *Nat. Commun.*, 2017, **8**, 944.

[177] Z. Geng, Y. Cao, W. Chen, X. Kong, Y. Liu, T. Yao, Y. Lin, *Appl. Catal., B*, 2019, **240**, 234-240.

[178] Y. Pan, R. Lin, Y. Chen, S. Liu, W. Zhu, X. Cao, W. Chen, K. Wu, W.-C. Cheong, Y. Wang, L. Zheng, J. Luo, Y. Lin, Y. Liu, C. Liu, J. Li, Q. Lu, X. Chen, D. Wang, Q. Peng, C. Chen, Y. Li, *J. Am. Chem. Soc.*, 2018, **140**, 4218-4221.

[179] S. L. Foster, S. I. P. Bakovic, R. D. Duda, S. Maheshwari, R. D. Milton, S. D. Minteer, M. J. Janik, J. N. Renner, L. F. Greenlee, *Nat. Catal.*, 2018, **1**, 490-500.

[180] C. Xiaoyang, T. Cheng, Z. Qiang, *Adv. Energy Mater.*, 2018, **8**, 1800369.

[181] W. Qiu, X.-Y. Xie, J. Qiu, W.-H. Fang, R. Liang, X. Ren, X. Ji, G. Cui, A. M. Asiri, G. Cui, B. Tang, X. Sun, *Nat. Commun.*, 2018, **9**, 3485.

[182] C. Guo, J. Ran, A. Vasileff, S.-Z. Qiao, *Energy Environ. Sci.*, 2018, **11**, 45-56.

[183] Z. Geng, Y. Liu, X. Kong, P. Li, K. Li, Z. Liu, J. Du, M. Shu, R. Si, J. Zeng, *Adv. Mater.*, 2018, **30**, 1803498.

[184] L. Han, X. Liu, J. Chen, R. Lin, H. Liu, F. Lü, S. Bak, Z. Liang, S. Zhao, E. Stavitski, J. Luo, R. R. Adzic, H. L. Xin, *Angew. Chem. Int. Ed.*, 2019, **58**, 2321-2325.

Table 1 Single atom catalysts supported on graphene layers or graphitized carbon for electrocatalytic water splitting

Catalyst	Synthetic method	Metal content [wt%]	Catalyst loading [mg cm^{-2}]	Electrolyte	η_{10} [mV]	Tafel slope [mV $decade^{-1}$]	TOF [s^{-1}] at specific η	Ref.
Hydrogen evolution reaction								
ALDPt/NGNs	ALD	2.1 by ICP	0.05	0.5 M H_2SO_4	~40	29	N/A	108
Pt_1/OLC	ALD	0.27 by ICP	0.51	0.5 M H_2SO_4	38	36	40.78 at 100 mV	141
Pt_1/graphene	ALD	0.33 by ICP	0.51	0.5 M H_2SO_4	~60	42	16.67 at 100 mV	141
Pt_1/MC	Photochemical reduction	2.6 by ICP	0.38	0.5 M H_2SO_4	25	26	N/A	110
Pt_1/NPC	Photochemical reduction	3.8 by ICP	0.1	0.5 M H_2SO_4	29	28	2.93 at 25 mV	111
Pt_1/NMC	Photochemical reduction	2.54 by ICP	0.39	0.5 M H_2SO_4	29	26	N/A	97
Pt SAs/DG	Thermal emitting	2.10 by ICP	1.0	0.5 M H_2SO_4	23	25	N/A	94
Pt_1/hNCNC	Impregnation-adsorption	2.92 by UV-vis	0.1	0.5 M H_2SO_4	15	24	7.67 at 20 mV	112
Pt@PCM	Pyrolysis	0.53 by ICP	N/A	0.5 M H_2SO_4	105	64	43.6 at 500 mV	142
Co-SAS/HOPNC	Pyrolysis	0.49 by ICP	0.6	0.5 M H_2SO_4	137	52	0.41 at 100 mV	60
Co-NG	Pyrolysis	2.54 by ICP	0.28	0.5 M H_2SO_4	147	82	0.10 at 100 mV	72
Co-NG-MW	Microwave-assisted pyrolysis	1.1 by ICP	0.1	0.5 M H_2SO_4	175	80	0.385 at 100 mV	76
Co_1/PCN	Pyrolysis	0.3 by ICP	0.5	1 M KOH	89	52	5.98 at 100 mV	126
PANICo750A	Pyrolysis	1.05 by ICP	N/A	0.5 M H_2SO_4	138	55	N/A	146
CoN_x/C	Pyrolysis	0.14 by ICP	2.0	0.5 M H_2SO_4	133	57	0.39 at 100 mV	147
Co-SAC	Pyrolysis	1.39 by XPS	0.2	0.5 M H_2SO_4	230	99	N/A	148
Ni-doped graphene	CVD	N/A	N/A	0.5 M H_2SO_4	~180	45	0.8 at 300 mV	143
A-Ni-C	Pyrolysis	1.5 by ICP	0.28	0.5 M H_2SO_4	34	41	N/A	144
A-Ni@DG	Pyrolysis	1.24 by ICP	0.26	0.5 M H_2SO_4	70	31	5.7 at 100 mV	145
W-SA	Pyrolysis	1.21 by ICP	0.2	0.1 M KOH	85	53	6.35 at 120 mV	150
$Mo_1N_1C_2$	Pyrolysis	1.32 by ICP	0.41	0.1 M KOH	132	90	0.465 at 100 mV	149
Oxygen evolution reaction								
Ni-NHGF	Pyrolysis	0.25 by ICP	0.27	1 M KOH	331	63	0.72 at 300 mV	25
S|NiN_x-PC/EG	Pyrolysis	0.2 by ICP	0.15	1 M KOH	280	45	10.9 at 300 mV	48
A-Ni@DG	Pyrolysis	1.24 by ICP	0.26	1 M KOH	270	47	13.4 at 300 mV	145
S,N-Fe/N/C-CNT	Pyrolysis	3.3 by XPS	0.6	0.1 M KOH	370	82	N/A	57
Fe-N_4 SAs/NPC	Pyrolysis	1.96 by ICP	0.51	1 M KOH	430	95	N/A	151
Mn-NG	Pyrolysis	0.026 by ICP	N/A	1 M KOH	337	55	N/A	74

Table 2 Single atom catalysts supported on graphene layers or graphitized carbon for electrocatalytic CO_2 reduction

Catalyst	Synthetic method	Metal content [wt%]	Catalyst loading [mg cm^{-2}]	Electrolyte	Potential	Current density [mA cm^{-2}]	Main product (Faradaic efficiency)	Ref.
A-Ni-NSG	Pyrolysis	2.8 by ICP	0.4	0.5 M $KHCO_3$	-0.72 V vs RHE	23.5	CO (94%)	46
Ni-N-C	Pyrolysis	0.24 by ICP	0.5	0.5 M $KHCO_3$	-0.77 V vs RHE	~7.5	CO (92%)	61
Ni-NG	Pyrolysis	2 by XPS	1	0.5 M $KHCO_3$	-0.74 V vs RHE	11	CO (95%)	73
Ni^{2+}@NG	Ion-adsorption	0.8 by ICP	0.3	0.5 M $KHCO_3$	-0.68 V vs RHE	10.2	CO (92%)	99
Ni-N-Gr	Pyrolysis	2.2 by ICP	0.3	0.1 M $KHCO_3$	-0.8 V vs RHE	~1.5	CO (90%)	157
Ni SAs/N-C	Pyrolysis	1.53 by ICP	0.1	0.5 M $KHCO_3$	-1.0 V vs RHE	10.5	CO (70.3%)	158
Ni-N_4-C	Pyrolysis	1.41 by ICP	0.2	0.5 M $KHCO_3$	-0.81 V vs RHE	28.6	CO (99%)	159
NiN-GS	Pyrolysis	~5 by XPS	1	0.5 M $KHCO_3$	-0.76 V vs RHE	21.3	CO (96%)	160
C-Zn_1Ni_4 ZIF-8	Pyrolysis	5.44 by ICP	2	0.5 M $KHCO_3$	-1.03 V vs RHE	71.5	CO (93.5%)	161
H-CP	Solid-state diffusion	N/A	3.5	0.5 M $KHCO_3$	-1.2 V vs RHE	60.11	CO (90.8%)	166
Ni SAs/NCNTs	Pyrolysis	6.63 by ICP	0.8	0.5 M $KHCO_3$	-1 V vs RHE	57.1	CO (95%)	167
Ni-N-MEGO	Pyrolysis	6.7 by ICP	0.5	0.5 M $KHCO_3$	-0.7 V vs RHE	29.1	CO (92%)	170
Ni-NCB	Pyrolysis	0.27 by ICP	0.2	0.5 M $KHCO_3$	-0.68 V vs RHE	6.8	CO (99%)	171
Ni-N-C	Pyrolysis	1.8 by XPS	0.75	0.1 M $KHCO_3$	-0.84 V vs RHE	15	CO (81%)	175
Ni-N-C	Pyrolysis	1.73 by XPS	0.76	0.1 M $KHCO_3$	-0.75 V vs RHE	11.2	CO (80%)	176
Co-N_2	Pyrolysis	0.25 by ICP	0.8	0.5 M $KHCO_3$	-0.63 V vs RHE	18.4	CO (94%)	45
Co_1-N_4	Pyrolysis	0.6 by ICP	N/A	0.1 M $KHCO_3$	-0.8 V vs RHE	~15	CO (82%)	177
Co-N_5/HNPCSs	Pyrolysis	3.54 by ICP	N/A	0.2 M $NaHCO_3$	-0.79 V vs RHE	10.2	CO (99.3%)	178
Fe^{3+}-N-C	Pyrolysis	2.8 by ICP	0.6	0.5 M $KHCO_3$	-0.47 V vs RHE	~21	CO (~95%)	128
Fe-N-C	Pyrolysis	0.5 by XPS	0.6	0.1 M $KHCO_3$	-0.68 V vs RHE	2.8	CO (93%)	163
Fe/NG-750	Pyrolysis	1.25 by ICP	0.32	0.1 M $KHCO_3$	-0.6 V vs RHE	~3	CO (80%)	173
$Fe_{0.5}$d	Pyrolysis	1.5 by XAS	1	0.1 M $KHCO_3$	-0.6 V vs RHE	4.5	CO (91%)	174
ZnN_x/C	Pyrolysis	0.1 by ICP	1	0.5 M $KHCO_3$	-0.43 V vs RHE	4.8	CO (95%)	164
Zn-N-G-800	Pyrolysis	~1.6 by ICP	2	0.5 M $KHCO_3$	-0.5 V vs RHE	4.1	CO (91%)	172
(Cl,N)-Mn/G	Pyrolysis	0.05 by ICP	0.5	0.5 M $KHCO_3$	-0.6 V vs RHE	13.4	CO (97%)	168
$Sn_1^{\delta+}$-NG	Pyrolysis	0.82 by ICP	0.24	0.25 M $KHCO_3$	-1.6 V vs SCE	11.7	Formate (75.1%)	165

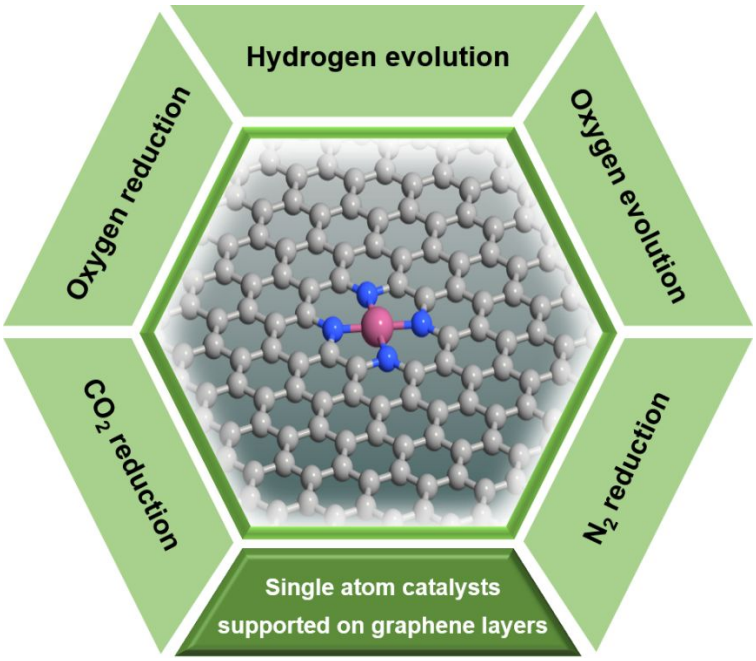

The synthetic strategies, structural identification and electrocatalytic applications of single atom catalysts supported on graphene or graphene-like carbons are reviewed.